The Astrophysical Journal, 869:130 (31pp), 2018 December 20 https://doi.org/10.3847/1538-4357/aaf054

Binary Neutron Star Mergers: Mass Ejection, Electromagnetic Counterparts, and Nucleosynthesis

David Radice[1,2], Albino Perego[3,4], Kenta Hotokezaka[2], Steven A. Fromm[5], Sebastiano Bernuzzi[3,6], and Luke F. Roberts[5]
[1] Institute for Advanced Study, 1 Einstein Drive, Princeton, NJ 08540, USA
[2] Department of Astrophysical Sciences, Princeton University, 4 Ivy Lane, Princeton, NJ 08544, USA
[3] Istituto Nazionale di Fisica Nucleare, Sezione Milano Bicocca, gruppo collegato di Parma, I-43124 Parma, Italy
[4] Dipartimento di Fisica, Università degli Studi di Milano Bicocca, Piazza della Scienza 3, I-20126 Milano, Italy
[5] NSCL/FRIB and Department of Physics & Astronomy, Michigan State University, 640 S. Shaw Lane, East Lansing, MI 48824, USA
[6] Theoretisch-Physikalisches Institut, Friedrich-Schiller-Universität Jena, D-07743, Jena, Germany
Received 2018 October 7; revised 2018 November 12; accepted 2018 November 12; published 2018 December 19

Abstract

We present a systematic numerical relativity study of the mass ejection and the associated electromagnetic transients and nucleosynthesis from binary neutron star (NS) mergers. We find that a few $10^{-3}\,M_{\odot}$ of material is ejected dynamically during the mergers. The amount and the properties of these outflows depend on binary parameters and on the NS equation of state (EOS). A small fraction of these ejecta, typically $\sim 10^{-6}\,M_{\odot}$, is accelerated by shocks formed shortly after merger to velocities larger than $0.6c$ and produces bright radio flares on timescales of weeks, months, or years after merger. Their observation could constrain the strength with which the NSs bounce after merger and, consequently, the EOS of matter at extreme densities. The dynamical ejecta robustly produce second and third *r*-process peak nuclei with relative isotopic abundances close to solar. The production of light *r*-process elements is instead sensitive to the binary mass ratio and the neutrino radiation treatment. Accretion disks of up to $\sim 0.2\,M_{\odot}$ are formed after merger, depending on the lifetime of the remnant. In most cases, neutrino- and viscously driven winds from these disks dominate the overall outflow. Finally, we generate synthetic kilonova light curves and find that kilonovae depend on the merger outcome and could be used to constrain the NS EOS.

Key words: nuclear reactions, nucleosynthesis, abundances – stars: neutron

1. Introduction

Merging neutron stars (NSs) are loud gravitational wave (GW) sources and power bright electromagnetic (EM) transients, as recently demonstrated by GW170817 (Abbott et al. 2017c, 2017d, 2017e, 2018b; Arcavi et al. 2017; Coulter et al. 2017; Drout et al. 2017; Evans et al. 2017; Hallinan et al. 2017; Kasliwal et al. 2017; Mooley et al. 2018a; Nicholl et al. 2017; Smartt et al. 2017; Soares-Santos et al. 2017; Tanvir et al. 2017; Troja et al. 2017; Lyman et al. 2018; Ruan et al. 2018). AT2017gfo, the EM counterpart to GW170817, has a UV/optical/IR component with blackbody-like spectrum that has been interpreted as the result of the radioactive decay of about $0.05\,M_{\odot}$ of material ejected during and shortly after the merger (Chornock et al. 2017; Cowperthwaite et al. 2017; Drout et al. 2017; Nicholl et al. 2017; Perego et al. 2017a; Tanaka et al. 2017; Tanvir et al. 2017; Utsumi et al. 2017; Villar et al. 2017; Waxman et al. 2018; Kawaguchi et al. 2018; Metzger et al. 2018). Nonthermal emission from the radio to the γ-ray bands was also observed. The origins of this EM component are less clear, but recent observations point to the presence of synchrotron radiation generated by a relativistic jetted outflow interacting with the interstellar medium (ISM; Abbott et al. 2017c; Kasliwal et al. 2017; Kim et al. 2017; Margutti et al. 2017, 2018; Mooley et al. 2018a, 2018b; Alexander et al. 2018; Barkov et al. 2018; Ghirlanda et al. 2018; Hotokezaka et al. 2018b; Lazzati et al. 2018; Nakar & Piran 2018; Resmi et al. 2018).

These groundbreaking observations are being used to constrain general relativity (GR; Lombriser & Taylor 2016; McManus et al. 2016; Abbott et al. 2017c; Baker et al. 2017; Pardo et al. 2018; Visinelli et al. 2018), cosmological parameters (Abbott et al. 2017a; Hotokezaka et al. 2018c), the equation of state (EOS) of NSs (Bauswein et al. 2017; Margalit & Metzger 2017; Shibata et al. 2017a; Abbott et al. 2018a; Annala et al. 2018; De et al. 2018; Drago et al. 2018; Fattoyev et al. 2018; Hinderer et al. 2018; Malik et al. 2018; Most et al. 2018b; Nandi et al. 2018; Paschalidis et al. 2018; Radice et al. 2018c; Rezzolla et al. 2018; Ruiz et al. 2018; Tews et al. 2018; Tsang et al. 2018; Wei et al. 2018), and the origin of short γ-ray bursts (SGRBs; Abbott et al. 2017c; Mooley et al. 2018a; Beniamini et al. 2019; Finstad et al. 2018; Lazzati et al. 2018), among others.

NS mergers also generate neutron-rich outflows that are thought to be a likely site for the production of *r*-process nuclei (Lattimer & Schramm 1974; Symbalisty & Schramm 1982; Eichler et al. 1989; Meyer 1989; Freiburghaus et al. 1999; Goriely et al. 2011; Korobkin et al. 2012; Wanajo et al. 2014; Just et al. 2015; Thielemann et al. 2017). This is supported by the UV/optical/IR follow-up observations to GW170817 (e.g., Kasen et al. 2017; Hotokezaka et al. 2018a; Rosswog et al. 2018). The observed signals are thought to have been produced by the decay of radioactive isotopes produced during the *r*-process. However, uncertainty persists on the exact rates and nucleosynthetic yields from mergers. These need to be addressed by future observations and theoretical studies.

Numerical simulations are the cornerstone to the modeling of multi-messenger signatures and nucleosynthetic yields from NS mergers. Binary NS mergers are essentially multi-physics problems, involving strong-field gravity, strongly interacting matter, relativistic (magneto-)hydrodynamics, and neutrino transport. Due to the complexity of the problem, most previous binary NS merger simulations either employed an approximate treatment for the gravitational field of the NSs (Ruffert et al. 1996; Rosswog et al. 1999, 2003, 2013;

Rosswog & Davies 2003; Rosswog & Liebendoerfer 2003; Oechslin et al. 2007; Korobkin et al. 2012; Bauswein et al. 2013), or included GR effects, but compromised on the treatment of NS matter (Shibata & Uryu 2000; Shibata et al. 2003, 2005; Baiotti et al. 2008; Kiuchi et al. 2010; Rezzolla et al. 2010, 2011; Hotokezaka et al. 2011, 2013a, 2013b; Palenzuela et al. 2013; Ruiz et al. 2016; Dietrich et al. 2017a, 2017b). In the last few years, however, full-GR simulations with a microphysical treatment of NS matter and with different levels of approximation for neutrino-radiation effects have also become available (Sekiguchi et al. 2011, 2015, 2016; Palenzuela et al. 2015; Foucart et al. 2016b; Lehner et al. 2016; Radice et al. 2016b; Bovard et al. 2017).

Merger simulations have clarified the mechanisms driving the mass ejection and highlighted the importance of neutrino effects. Complementary studies on the long-term evolution of merger remnants also revealed the importance of the magnetically, neutrino-, and viscously driven secular outflows (Metzger et al. 2008, 2009, 2018; Dessart et al. 2009; Lee et al. 2009; Fernández & Metzger 2013; Metzger & Fernández 2014; Perego et al. 2014; Siegel et al. 2014; Just et al. 2015; Martin et al. 2015; Wu et al. 2016; Fujibayashi et al. 2017, 2018; Lippuner et al. 2017; Siegel & Metzger 2017, 2018; Fernández et al. 2019). These might in some cases dominate the nucleosynthetic yields and produce the bulk of the thermal radiation from NS mergers. However, quantitative questions remain concerning the dependence of the multi-messenger emissions and of the *r*-process production on the binary parameters and the EOS. Indeed, most previous studies considered only several binary configurations, with the exception of Hotokezaka et al. (2013a) and Dietrich et al. (2017a, 2017b), who used an ideal-gas prescription to approximate thermal effects in the NS matter, and Bauswein et al. (2013) who used temperature dependent microphysical EOSs, but adopted an approximate treatment of gravity and neglected weak reactions.

In this work, we present a systematic study of the mass ejection, nucleosynthetic yields, and EM counterparts of NS mergers based on 59 high-resolution numerical relativity simulations. We employ four microphysical temperature-dependent nuclear EOSs and include the impact of neutrino losses. We consider total binary masses between $2.4\,M_\odot$ and $3.4\,M_\odot$ and mass ratios between 0.85 and 1. Our data sets also includes 13 simulations with an effective treatment of neutrino reabsorption and six simulations with viscosity. We quantify the dependence of dynamical ejecta mass and intrinsic properties on the binary parameters and NS EOS. We compute nucleosynthetic yields for the dynamical ejecta and show that second and third *r*-process peaks are robustly produced with relative isotopic abundances close to solar, while the production of light *r*-process elements is sensitive to the binary mass ratio and the treatment of neutrino radiation. We estimate kilonova light curves and show that their properties depend on the lifetime of the merger remnant. We also compute the expected radio signal from the interaction between the ejecta and the ISM. This signal could be used to probe the strength of the shocks generated after merger and, thus, indirectly the EOS of matter at extreme densities and temperatures. Our simulations also reveal a new outflow mechanism operating in unequal mass binaries and enabled by viscosity. These "viscous-dynamical" ejecta are launched due to the thermalization of mass exchange streams between the secondary and the primary NS shortly before merger and is discussed in more detail in a companion paper (Radice et al. 2018b).

The rest of this paper is organized as follows. Section 2 summarizes the numerical methods and the initial data employed for the simulations. Section 3 discusses dynamical and secular mass ejection. Section 4 reports on our *r*-process nucleosynthesis calculations and yields. Section 5 is dedicated to the discussion of the EM counterparts from binary NS mergers, focusing on the kilonova signal and on the radio remnant powered by the interaction of the ejecta with the ISM. Section 6 is dedicated to a discussion and conclusions. Finally, Appendices A and B present a discussion of finite-resolution effects and implementation details of the viscosity treatment employed by the simulations.

2. Methods

2.1. Initial Data

We construct initial data in quasi-circular orbit using the `Lorene` pseudo-spectral code (Gourgoulhon et al. 1999). The initial separation between the NSs is set to 40 km, corresponding to ∼2–3 orbits before merger. The EOSs used for the initial data are constructed from the minimum temperature slice of the EOS table used for the evolution, assuming neutrino-less beta-equilibrium. To create the initial data tables we also subtract from the pressure the contribution of photon radiation, which dominates at the lowest densities due to the assumption of constant temperature. When reading the initial data in the evolution code we set the electron fraction according to the beta-equilibrium condition, and we reset the specific internal energy according to the minimum temperature slice in the EOS table used for the evolution. Small errors in the initial data and in the mapping from the zero- to the finite-temperature EOSs induce small oscillations in the NSs prior to merger. We quantify these in terms of the relative change of the central density of the stars, which we find typically to be $\lesssim$2%–3%.

2.2. General-relativistic Hydrodynamics

We evolve the initial data using the `WhiskyTHC` code (Radice & Rezzolla 2012; Radice et al. 2014a, 2014b, 2015). `WhiskyTHC` separately evolves the proton and neutron number densities

$$\nabla_\mu (n_{p,n} u^\mu) = R_{p,n}, \tag{1}$$

where $n_p = Y_e n$ is the proton number density, n_n is the neutron number density, $n = n_p + n_n$ is the baryon number density, u^μ is the fluid four-velocity, and Y_e is the electron fraction of the material. $R_p = -R_n$ is the net lepton number deposition rate due to the absorption and emission of neutrinos and anti-neutrinos (see Section 2.3).

We model NS matter as a perfect fluid with stress-energy tensor

$$T_{\mu\nu} = (e + p) u_\mu u_\nu + p g_{\mu\nu}, \tag{2}$$

where e is the energy density and p the pressure. We solve the Euler equations for the balance of energy and momentum

$$\nabla_\nu T^{\mu\nu} = Q u^\mu, \tag{3}$$

where Q is the net energy deposition rate due to the absorption and emission of neutrinos (see Section 2.3).

WhiskyTHC discretizes Equations (1) and (3) using high-resolution shock-capturing schemes. For the simulations presented in this work we use a central Kurganov–Tadmor-type scheme (Kurganov & Tadmor 2000) employing the HLLE flux formula (Einfeldt 1988) and non-oscillatory reconstruction of the primitive variables with the MP5 scheme of Suresh (1997). For numerical reasons we embed the NSs in a low-density medium, with $\rho_0 = m_b n \simeq 6 \times 10^4\ \mathrm{g\ cm^{-3}}$, where m_b is the atomic mass unit. We use the best available numerical schemes for the treatment of low-density regions and for the advection of the fluid composition. We employ the positivity-preserving limiter from Radice et al. (2014b) to ensure rest-mass conservation even in the presence of the artificial density floor, and we use the consistent multi-fluid advection method of Plewa & Müller (1999) to ensure separate local conservation of the proton and neutron number densities. Furthermore, we extract the outflows properties when the density is still several orders of magnitude higher than that of the artificial atmosphere.

The spacetime is evolved using the Z4c formulation of Einstein's equations (Bernuzzi & Hilditch 2010; Hilditch et al. 2013) as implemented in the CTGamma code (Pollney et al. 2011; Reisswig et al. 2013b), which is part of the Einstein Toolkit (Löffler et al. 2012). CTGamma implements fourth-order finite-differencing of the equations and we use fifth-order Kreiss–Oliger dissipation to ensure the nonlinear stability of the evolution (Kreiss & Oliger 1973). The coupling between the hydrodynamics and the spacetime evolution is handled using the method of lines. We adopt the optimal strongly stability-preserving third-order Runge–Kutta scheme (Gottlieb et al. 2008) as the time integrator. The timestep is set according to the speed-of-light Courant–Friedrichs–Lewy (CFL) condition with CFL factor 0.15. We remark that numerical stability only requires the CFL to be less than 0.25. However, the smaller value of 0.15 is necessary to guarantee the positivity of the density when using the positivity-preserving limiter implemented in WhiskyTHC.

Our simulation domain covers a cube of 3024 km diameter whose center is at the center of mass of the binary. Our code uses Berger–Oliger conservative adaptive mesh refinement (AMR; Berger & Oliger 1984) with sub-cycling in time and refluxing (Berger & Colella 1989; Reisswig et al. 2013a) as provided by the Carpet module of the Einstein Toolkit (Schnetter et al. 2004). We set up an AMR grid structure with seven refinement levels. The finest refinement level covers both NSs during the inspiral and the remnant after the merger and has a typical resolution of $h \simeq 185$ m. For selected binaries, we also perform simulations with finest grid resolution of 123 and 246 m. See Table 2 for a summary of our models.

2.3. Neutrino Leakage Scheme

We treat compositional and energy changes in the material due to weak reactions using a leakage scheme (Galeazzi et al. 2013; Radice et al. 2016b; see also van Riper & Lattimer 1981; Ruffert et al. 1996; Rosswog & Liebendoerfer 2003; O'Connor & Ott 2010; Sekiguchi 2010; Neilsen et al. 2014; Perego et al. 2016; Ardevol-Pulpillo et al. 2018 for other implementations). Our scheme tracks reactions involving electron ν_e and anti-electron type $\bar{\nu}_e$ neutrinos separately. Heavy-lepton neutrinos are lumped together in a single effective specie labeled ν_x. We account for the reactions listed in Table 1. We use the formulas from the references listed in the tables to compute the neutrino production rates R_ν, $\nu \in \{\nu_e, \bar{\nu}_e, \nu_x\}$, the associated energy release Q_ν, and neutrino absorption $\kappa_{\nu,a}$ and scattering $\kappa_{\nu,s}$ opacities. In doing so, we assume that the neutrinos follow Fermi–Dirac distributions with chemical potentials obtained assuming beta-equilibrium with thermalized neutrinos as in Rosswog & Liebendoerfer (2003). Following Ruffert et al. (1996), we also distinguish between the number-density-weighted opacities $\kappa^0_{\nu,a}$ and $\kappa^0_{\nu,s}$ which determine the rate at which neutrinos diffuse out of the material, and the energy-density-weighted opacities $\kappa^1_{\nu,a}$ and $\kappa^1_{\nu,s}$ which determine the rate at which energy diffuses out of the material due to the loss of neutrinos.

Table 1
Weak Reaction Rates and References for Their Implementation

Reaction	Reference
$\nu_e + n \leftrightarrow p + e^-$	Bruenn (1985)
$\bar{\nu}_e + p \leftrightarrow n + e^+$	Bruenn (1985)
$e^+ + e^- \to \nu + \bar{\nu}$	Ruffert et al. (1996)
$\gamma + \gamma \to \nu + \bar{\nu}$	Ruffert et al. (1996)
$N + N \to \nu + \bar{\nu} + N + N$	Burrows et al. (2006)
$\nu + N \to \nu + N$	Ruffert et al. (1996)
$\nu + A \to \nu + A$	Shapiro & Teukolsky (1983)

Note. We use the following notation: $\nu \in \{\nu_e, \bar{\nu}_e, \nu_x\}$ denotes a neutrino, ν_x denote any heavy-lepton neutrino, $N \in \{n, p\}$ denotes a nucleon, and A denotes a nucleus.

The total neutrino opacities $\kappa^\alpha_{\nu,a} + \kappa^\alpha_{\nu,s}$, with $\alpha \in \{0,1\}$, are used to compute an estimate to the optical depth τ^α_ν following the scheme of Neilsen et al. (2014), which is well-suited to the complex geometries present in NS mergers. We use the optical depth to define effective emission rates as (Ruffert et al. 1996)

$$R^{\mathrm{eff}}_\nu = \frac{R_\nu}{1 + t^0_{\mathrm{diff}}\,(t^0_{\mathrm{loss}})^{-1}}, \tag{4}$$

where we have introduced the effective diffusion time t_{diff}

$$t^0_{\mathrm{diff}} = \mathcal{D}\frac{(\tau^0_\nu)^2}{\kappa^0_{\nu,a} + \kappa^0_{\nu,s}}, \tag{5}$$

the neutrino emission timescale

$$t^0_{\mathrm{loss}} = \frac{R_\nu}{n_\nu}, \tag{6}$$

and n_ν is the neutrino number density computed assuming beta-equilibrium with neutrinos. The constant $\mathcal{D}$ is a tuning parameter that we set to 6. The effective energy emission rates Q^{eff}_ν are computed along the same lines, but using τ^1_ν, $\kappa^1_{\nu,a}$, and $\kappa^1_{\nu,s}$ instead of τ^0_ν, $\kappa^0_{\nu,a}$, and $\kappa^0_{\nu,s}$, respectively.

Neutrinos are split into a trapped component n^{trap}_ν and a free-streaming component n^{fs}_ν. Free-streaming neutrinos are emitted according to the effective rate R^{eff}_ν of Equation (4) and with average energy $Q^{\mathrm{eff}}_\nu / R^{\mathrm{eff}}_\nu$ and then evolved according to the M0 scheme we introduced in Radice et al. (2016b) and which is briefly summarized below. In our implementation the pressure due to the trapped neutrino component is neglected, since it is found to be unimportant in the conditions relevant for NS mergers (Galeazzi et al. 2013).

The M0 scheme evolves the number density of the free-streaming neutrinos assuming that they move along radial null rays with four-vector k^α normalized so that $k^\alpha u_\alpha = -1$. Under these assumptions it is possible to show that that the free-streaming fluid rest frame neutrino number density $n_\nu^{\rm fs}$ satisfies (Radice et al. 2016b)

$$\nabla_\alpha [n_\nu^{\rm fs} k^\alpha] = R_\nu^{\rm eff} - \kappa_{\nu,a}^{\rm eff} n_\nu^{\rm fs}, \tag{7}$$

where $R_\nu^{\rm eff}$ is the effective luminosity from Equation (4) and the effective absorption rates are defined as

$$\kappa_{\nu,a}^{\rm eff} = e^{-\tau_\nu^0} \left(\frac{E_\nu^{\rm fs}}{E_\nu^\beta} \right)^2 \kappa_{\nu,a}^0. \tag{8}$$

We have also introduced the average energy of free-streaming neutrinos $E_\nu^{\rm fs}$ and the average neutrino energy in beta-equilibrium E_ν^β, both defined in the fluid rest frame. Note that in the simulations we reported in Radice et al. (2016b) the term in parenthesis on the right-hand side of Equation (8) was neglected. We report a comparison of results obtained with and without the inclusion of this term in Section 4.1.

Our scheme estimates the free-streaming neutrino energy under the additional assumption, only approximately satisfied in our simulations, of stationarity of the metric. Accordingly, ∂_t is assumed to be a Killing vector so that $p_\nu^\alpha (\partial_t)_\alpha$, p_ν^α being the neutrino four-momentum, is a conserved quantity. Under this assumption it is possible to show that the average free-streaming neutrino energy satisfies (Radice et al. 2016b)

$$k^t \partial_t (E_\nu^{\rm fs} \chi) + k^r \partial_r (E_\nu^{\rm fs} \chi) = \frac{\chi}{n_\nu^{\rm fs}} (Q_\nu^{\rm eff} - E_\nu^{\rm fs} R_\nu^{\rm eff}), \tag{9}$$

where $\chi = -k^\alpha\, (\partial_t)_\alpha$.

In the simulations in which it is employed, the M0 scheme is switched on shortly before the two NSs collide, when neutrino–matter interactions start to become dynamically important. We solve Equations (7) and (9) on a uniform spherical grid extending to $512\, G/c^2\, M_\odot \simeq 756$ km and having $n_r \times n_\theta \times n_\phi = 3096 \times 32 \times 64$ grid points.

The coupling between neutrinos and matter is treated using an operator split approach, discussed in detail in Radice et al. (2016b). The source terms for Equations (1) and (3) are, respectively,

$$R_p = (\kappa_{\nu_e,a}^{\rm eff} n_{\nu_e}^{\rm fs} - \kappa_{\bar\nu_e,a}^{\rm eff} n_{\bar\nu_e}^{\rm fs}) - (R_{\nu_e}^{\rm eff} - R_{\bar\nu_e}^{\rm eff}), \tag{10}$$

and

$$\begin{aligned} Q = {} & (\kappa_{\nu_e,a}^{\rm eff} n_{\nu_e}^{\rm fs} E_{\nu_e} + \kappa_{\bar\nu_e,a}^{\rm eff} n_{\bar\nu_e}^{\rm fs} E_{\bar\nu_e}) \\ & - (Q_{\nu_e}^{\rm eff} + Q_{\bar\nu_e}^{\rm eff} + Q_{\nu_x}^{\rm eff}). \end{aligned} \tag{11}$$

The M0 scheme is more approximate than the frequency-integrated M1 scheme adopted by, e.g., Sekiguchi et al. (2015) and Foucart et al. (2015). However it has the advantage of computational efficiency, it includes gravitational and Doppler effects, albeit in an approximate way, and does not suffer from unphysical radiation shocks in the important region above the merger remnant that plagues M1 schemes (Foucart et al. 2018a).

2.4. Viscosity

Our simulations do not include magnetic fields, so we cannot model the possible emergence of magnetically driven outflows and jets after the merger (Rezzolla et al. 2011; Bucciantini et al. 2012; Siegel et al. 2014; Ruiz et al. 2016; Metzger et al. 2018). Moreover, we cannot self-consistently treat the transport of angular momentum in the merger remnant, which is primarily due to magnetic stresses (Duez et al. 2006; Kiuchi et al. 2014, 2018; Guilet et al. 2017). We leave the treatment of jets and relativistic winds, which necessarily requires high-resolution GR magnetohydrodynamic (GRMHD) simulations, to future work. On the other hand, we study the range of possible effects due to the angular momentum transport by means of an effective viscosity which we include in a subset of our simulations. The use of this approach has not yet been fully validated for NS merger simulations. However, it has been found to reproduce some of the main features of the MHD dynamics in the context of post-merger accretion disks (Fernández et al. 2019).

More specifically, we use the GR large eddy simulations method (GRLES; Radice 2017) to explore the impact of subgrid-scale turbulent angular momentum transport. Accordingly, we decompose the stress energy tensor of the fluid $T^{\mu\nu}$ as

$$T_{\mu\nu} = E n_\mu n_\nu + S_\mu n_\nu + S_\nu n_\mu + S_{\mu\nu}, \tag{12}$$

where

$$E = T_{\mu\nu} n^\mu n^\nu = \rho h W^2 - p, \tag{13}$$

$$S_\mu = -\gamma_{\mu\alpha} n_\beta T^{\alpha\beta} = \rho h W^2 v_\mu, \tag{14}$$

$$S_{\mu\nu} = \gamma_{\mu\alpha}\gamma_{\mu\beta} T^{\alpha\beta} = S_\mu v_\nu + p\gamma_{\mu\nu} + \tau_{\mu\nu}, \tag{15}$$

and n^μ is the normal to the space-like slice hyper-surface, while $\gamma_{\mu\nu}$, v^μ, and W are, respectively, the spatial metric, the three-velocity, and the Lorentz factor. $\tau_{\mu\nu}$ is a purely spatial tensor representing the effect of subgrid scale turbulence. As in Radice (2017), we use the following ansatz for τ_{ij}:

$$\tau_{ij} = -2\nu_T (\rho + p) W^2 \left[\frac{1}{2}(D_i v_j + D_j v_i) - \frac{1}{3} D_k v^k \gamma_{ij} \right], \tag{16}$$

where $\nu_T = \ell_{\rm mix} c_s$ is the turbulent viscosity, c_s is the sound speed, D_i denotes the covariant derivative compatible with the spatial metric, and $\ell_{\rm mix}$ is a free parameter we vary to study the sensitivity of our results to turbulence. In the context of accretion disk theory, turbulent viscosity is typically parameterized in terms of a dimensionless constant α linked to $\ell_{\rm mix}$ through the relation $\ell_{\rm mix} = \alpha\, c_s\, \Omega^{-1}$, where Ω is the angular velocity of the fluid (Shakura & Sunyaev 1973). Recently, Kiuchi et al. (2018) performed very high-resolution GRMHD simulations of an NS merger with sufficiently high seed magnetic fields (10^{15} G) to be able to resolve the magnetorotational instability in the merger remnant and reported averaged α values for different rest-mass density shells. Combining their estimate of α with values of c_s and Ω from our simulations we find values of $\ell_{\rm mix} = 0$–30 m. Here, we conservatively vary $\ell_{\rm mix}$ between 0 (default; no subgrid model) and 50 m (very efficient angular momentum transport).

`WhiskyTHC` consistently includes the contributions of $\tau_{\mu\nu}$ to the fluid stress energy tensor in the calculation of the right-hand side of the metric and fluid equations. Flux terms resulting from the inclusion of $\tau_{\mu\nu}$ need to be treated with care, because a naive application of Godunov-type methods would result in a scheme suffering from an odd–even decoupling instability (e.g., Lowrie & Morel 2001). `WhiskyTHC` uses a proper combination of left- and right-biased finite-differencing operators to discretize terms arising from the derivatives of

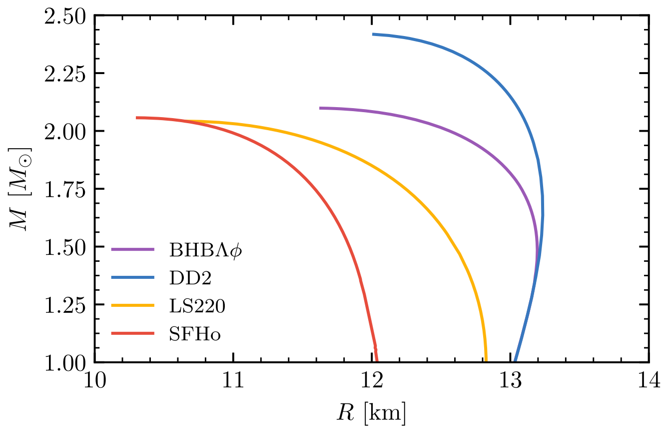

Figure 1. NS masses and radii predicted by the EOSs considered in this study. The BHB$\Lambda\phi$ and DD2 EOSs predict the same radii for NSs less massive than $\sim$1.5 $M_\odot$. BHB$\Lambda\phi$ predicts smaller radii for more massive NSs and a smaller maximum mass. The LS220 and SFHo EOSs have similar maximum masses and similar compactness close to the maximum mass. However, LS220 predicts radii almost 1 km larger than SFHo for a canonical 1.4 $M_\odot$ NS.

$\tau_{\mu\nu}$ in a flux-conservative fashion. The details are given in Appendix B.

2.5. Models

For our survey we consider four different nuclear EOSs: the DD2 EOS (Hempel & Schaffner-Bielich 2010; Typel et al. 2010), the BHB$\Lambda\phi$ EOS (Banik et al. 2014), the LS220 EOS (Lattimer & Swesty 1991), and the SFHo EOS (Steiner et al. 2013). These EOSs predict NS maximum masses and radii within the range allowed by current astrophysical constraints, including the recent LIGO/Virgo constraint on tidal deformability (Abbott et al. 2017d, 2018a, 2018b; De et al. 2018). The LS220 EOS is based on a liquid droplet Skyrme model while the other three EOSs are based on nuclear statistical equilibrium with a finite-volume correction coupled to a relativistic mean field theory for treating high-density nuclear matter. DD2 and SFHo use different parameterizations and values for modeling the mean-field nuclear interactions. The BHB$\Lambda\phi$ EOS uses the same nucleon interactions as the DD2 EOS, but also includes interacting Λ hyperons that can be produced at high density and soften the EOS.

Although these EOSs differ in many aspects, including their finite-temperature properties and their dependence on the neutron richness of the system, we can generally characterize them by the Tolman–Oppenheimer–Volkoff (TOV) solutions they predict, which we show in Figure 1. SFHo, LS220, DD2, and BHB$\Lambda\phi$ support 2.06, 2.06, 2.42, and 2.11 $M_\odot$ cold, non-rotating maximum NS masses and have $R_{1.4}$ of 11.9, 12.7, 13.2, and 13.2 km, respectively. Since NS radii correlate with the pressure at roughly twice saturation density (Lattimer 2012), we refer to EOSs having smaller $R_{1.4}$ as being "softer" and to EOSs having larger $R_{1.4}$ as being "stiffer." Although all four models have saturation density symmetry energies within experimental bounds, LS220 has a significantly steeper density dependence of its symmetry energy than the other models. In all models, the finite-temperature behavior of the EOS is mainly determined by the nucleon effective mass, with smaller effective masses leading to higher temperatures for constant entropy. LS220 assumes that the nucleon mass is the bare nucleon mass at all densities, while SFHo has $m_N^*/m_N = 0.76$ at saturation density, and both DD2 and BHB $\Lambda\phi$ have $m_N^*/m_N = 0.56$, where m_N^* is the effective nucleon mass and m_N is the bare nucleon mass.

We considered 35 distinct binaries with total masses $M \in [2.4, 3.4]\, M_\odot$ and mass ratios in the range $q \in [0.85, 1]$. All binaries have been simulated using the leakage scheme discussed above; selected binaries have also been simulated with the M0 scheme, at different resolutions, and/or with viscosity, for a total of 59 simulations. A summary of all simulations and key results is given in Table 2. Each run is labeled after the employed EOS, the masses of the two NSs at infinite separation, the simulated physics, the value of the mixing length $\ell_{\rm mix}$ in meters, if larger than zero and, in the case of binaries run at multiple resolutions, the resolution (`LR`: low resolution, `HR`: high resolution). For example, `LS220_M140120_M0_L25` is a binary with NSs masses 1.4 $M_\odot$ and 1.2 $M_\odot$ that was simulated with the LS220 EOS, employing the M0 scheme, with $\ell_{\rm mix} = 25$ m, and run at our standard resolution $h = 185$ m. We will make all of our GW waveforms publicly available as part of the `CoRe` catalog (Dietrich et al. 2018).

We simulate all binaries for at least 20 ms after the merger, or until few milliseconds after black hole (BH) formation if this occurs earlier. With the exceptions of the runs including viscosity, which we discuss in more detail in a companion paper (Radice et al. 2018b), the outflow rate, precisely defined in Section 3, has dropped to zero at the end of our simulations. Our models include binaries spanning all possible outcomes predicted for NS binary mergers (e.g., Shibata 2016). Some of our binaries produce BHs promptly at the time of the merger; others produce hypermassive neutron stars (HMNSs) that collapse on timescales of several milliseconds (Baumgarte et al. 2000; Shibata & Taniguchi 2006; Baiotti et al. 2008; Sekiguchi et al. 2011; Bernuzzi et al. 2016), or long-lived massive NS remnants, expected to be stable on secular timescales or, in some cases, indefinitely (Giacomazzo & Perna 2013; Foucart et al. 2016a; Radice et al. 2018a). Table 2 reports the time to BH formation in milliseconds from the merger $t_{\rm BH}$, or a lower limit if the central object does not collapse within the simulation time.

3. Mass Ejection

Tidal interactions and shocks exerted on the NSs close to the time of merger trigger the ejection of material on a dynamical timescale, the so-called *dynamical ejecta* (e.g., Bauswein et al. 2013; Hotokezaka et al. 2013b; Radice et al. 2016b). Dynamical ejecta mass and average properties are reported in Table 2. In simulations that do not include viscosity the outflow rate drops to zero a few milliseconds after the merger. However, it is expected that more material will become unbound from the remnant on longer timescales, due to magnetic effects and/or nuclear recombination (e.g., Fernández & Metzger 2013; Perego et al. 2014; Siegel & Metzger 2017; Fernández et al. 2019; Fujibayashi et al. 2018), which we cannot currently study with our simulations. We refer to this latter component as the *secular ejecta* to distinguish it from the dynamical ejecta defined above. The simulations performed with viscosity show the early development of viscously driven outflows. However, due to the high computational costs, we do not follow the postmerger remnant for sufficiently long times to study the secular ejecta.

Table 2
Dynamical Ejecta and Remnant Disks for All Simulations

Model	h (m)	M_a ($M_\odot$)	M_b ($M_\odot$)	$t_{\rm BH}$ (ms)	$M_{\rm disk}$ ($10^{-2}\,M_\odot$)	$M_{\rm ej}$ ($10^{-2}\,M_\odot$)	$M_{\rm ej}^{v\geqslant 0.6c}$ ($10^{-5}\,M_\odot$)	$\langle Y_e \rangle$	$\langle s \rangle$ ($k_{\rm B}$)	$v_{\rm ej}$ (c)	$\theta_{\rm ej}$	$T_{\rm ej}$ (10^{50} erg)
BHBlp_M125125_LK	185	1.25	1.25	>21.9	NA	0.13	0.000	0.13	15	0.18	22	0.46
BHBlp_M1365125_LK	185	1.365	1.25	>24.0	18.73	0.06	1.367	0.14	17	0.21	25	0.35
BHBlp_M130130_LK	185	1.3	1.3	>26.9	NA	0.07	0.000	0.16	22	0.12	33	0.11
BHBlp_M135135_LK	185	1.35	1.35	>21.3	14.45	0.07	0.746	0.15	20	0.17	28	0.26
BHBlp_M135135_LK_HR	123	1.35	1.35	>23.3	14.26	0.05	0.015	0.16	20	0.18	24	0.19
BHBlp_M135135_M0	185	1.35	1.35	>37.0	12.75	0.14	0.283	0.26	24	0.14	38	0.40
BHBlp_M140120_LK	185	1.4	1.2	>23.7	20.74	0.11	0.229	0.11	13	0.16	22	0.36
BHBlp_M140120_M0	185	1.4	1.2	>28.2	22.56	0.16	0.994	0.19	17	0.17	30	0.60
BHBlp_M140140_LK	185	1.4	1.4	12.0	7.05	0.09	0.232	0.15	18	0.17	28	0.34
BHBlp_M140140_LK_HR	123	1.4	1.4	10.3	5.38	0.10	0.793	0.14	17	0.20	26	0.50
BHBlp_M144139_LK	185	1.44	1.39	10.4	8.28	0.06	0.511	0.18	22	0.20	30	0.30
BHBlp_M150150_LK	185	1.5	1.5	2.3	1.93	0.05	0.727	0.17	20	0.23	28	0.33
BHBlp_M160160_LK	185	1.6	1.6	1.0	0.09	0.00	0.000	…	…	…	…	…
DD2_M120120_LK	185	1.2	1.2	>24.7	NA	0.08	0.000	0.15	21	0.14	31	0.16
DD2_M125125_LK	185	1.25	1.25	>32.4	NA	0.04	0.000	0.18	27	0.15	33	0.10
DD2_M1365125_LK	185	1.365	1.25	>24.2	20.83	0.04	0.443	0.15	21	0.20	25	0.20
DD2_M130130_LK	185	1.3	1.3	>22.9	NA	0.12	0.005	0.13	15	0.18	21	0.45
DD2_M135135_LK	185	1.35	1.35	>24.4	15.69	0.03	0.024	0.18	27	0.18	31	0.12
DD2_M135135_LK_HR	123	1.35	1.35	>23.4	15.05	0.02	0.001	0.18	28	0.19	30	0.09
DD2_M135135_M0	185	1.35	1.35	>20.4	16.16	0.14	0.168	0.23	21	0.17	31	0.49
DD2_M140120_LK	185	1.4	1.2	>23.6	19.26	0.09	0.307	0.12	15	0.18	23	0.36
DD2_M140120_M0	185	1.4	1.2	>26.9	19.48	0.16	0.570	0.21	18	0.16	34	0.54
DD2_M140140_LK	185	1.4	1.4	>24.5	12.36	0.04	0.529	0.17	22	0.22	28	0.26
DD2_M140140_LK_HR	123	1.4	1.4	>24.6	16.85	0.09	0.431	0.14	17	0.18	28	0.39
DD2_M144139_LK	185	1.44	1.39	>23.5	14.40	0.05	0.158	0.17	22	0.20	28	0.26
DD2_M150150_LK	185	1.5	1.5	>23.1	16.70	0.07	0.462	0.20	23	0.17	32	0.26
DD2_M160160_LK	185	1.6	1.6	2.3	1.96	0.12	2.759	0.14	13	0.24	20	0.83
LS220_M120120_LK	185	1.2	1.2	>23.2	17.43	0.14	0.000	0.12	15	0.15	25	0.33
LS220_M1365125_LK	185	1.365	1.25	>26.7	16.86	0.11	0.013	0.10	13	0.16	23	0.32
LS220_M135135_LK	185	1.35	1.35	20.3	7.25	0.06	0.000	0.11	16	0.16	23	0.17
LS220_M135135_LK_LR	246	1.35	1.35	>27.6	NA	0.11	0.000	0.13	16	0.16	26	0.32
LS220_M135135_M0	185	1.35	1.35	>22.6	9.06	0.19	0.009	0.25	19	0.15	35	0.50
LS220_M135135_M0_L05	185	1.35	1.35	>24.5	14.07	0.27	0.061	0.27	20	0.13	38	0.58
LS220_M135135_M0_L25	185	1.35	1.35	18.1	4.65	0.20	0.395	0.26	21	0.14	42	0.51
LS220_M135135_M0_L50	185	1.35	1.35	>32.0	8.59	0.20	0.419	0.26	24	0.16	44	0.66
LS220_M135135_M0_LTE	185	1.35	1.35	>21.1	14.24	0.11	0.000	0.20	17	0.13	30	0.24
LS220_M140120_LK	185	1.4	1.2	>23.5	22.82	0.19	0.000	0.09	11	0.15	20	0.47
LS220_M140120_M0	185	1.4	1.2	>24.8	23.38	0.24	0.001	0.18	14	0.15	29	0.63
LS220_M140120_M0_L05	185	1.4	1.2	>28.2	20.33	0.28	0.017	0.18	14	0.15	29	0.76
LS220_M140120_M0_L25	185	1.4	1.2	>28.5	12.07	0.41	0.625	0.16	13	0.20	29	1.97
LS220_M140120_M0_L50	185	1.4	1.2	>31.2	13.97	0.70	8.289	0.18	13	0.22	28	3.97
LS220_M140140_LK	185	1.4	1.4	9.9	4.58	0.14	0.087	0.14	16	0.17	29	0.48
LS220_M140140_LK_HR	123	1.4	1.4	9.4	2.68	0.07	0.168	0.15	17	0.17	33	0.26
LS220_M140140_LK_LR	246	1.4	1.4	8.6	3.12	0.17	0.019	0.16	15	0.19	28	0.68
LS220_M144139_LK	185	1.44	1.39	7.2	3.91	0.19	0.014	0.14	15	0.16	30	0.54
LS220_M145145_LK	185	1.45	1.45	2.3	2.05	0.16	1.230	0.14	14	0.21	22	0.82
LS220_M150150_LK	185	1.5	1.5	0.9	0.16	0.03	0.001	0.08	11	0.19	13	0.13
LS220_M160160_LK	185	1.6	1.6	0.6	0.07	0.03	0.000	0.07	8	0.21	8	0.14
LS220_M171171_LK	185	1.71	1.71	0.5	0.06	0.03	0.000	0.08	9	0.22	8	0.14
SFHo_M1365125_LK	185	1.365	1.25	>26.4	8.81	0.15	1.888	0.14	14	0.23	24	0.92
SFHo_M135135_LK	185	1.35	1.35	12.0	6.23	0.35	1.924	0.17	14	0.24	28	2.24
SFHo_M135135_LK_HR	123	1.35	1.35	6.9	1.78	0.23	0.982	0.17	14	0.21	29	1.23
SFHo_M135135_LK_LR	246	1.35	1.35	3.4	2.79	0.36	1.877	0.18	14	0.24	27	2.35
SFHo_M135135_M0	185	1.35	1.35	7.7	1.23	0.42	3.255	0.22	17	0.22	33	2.40
SFHo_M140120_LK	185	1.4	1.2	>24.3	11.73	0.12	1.302	0.14	14	0.20	27	0.59
SFHo_M140120_M0	185	1.4	1.2	>32.7	15.65	0.30	2.368	0.22	17	0.16	34	1.05
SFHo_M140140_LK	185	1.4	1.4	1.1	0.01	0.04	3.853	0.19	37	0.35	24	0.60
SFHo_M144139_LK	185	1.44	1.39	0.9	0.09	0.04	3.056	0.18	16	0.33	20	0.53
SFHo_M146146_LK	185	1.46	1.46	0.7	0.02	0.00	0.000	…	…	…	…	…

Note. We report the model name, the grid resolution h, the NS masses at infinite separation M_a and M_b, the time of BH formation $t_{\rm BH}$, the remnant disk masses $M_{\rm disk}$, the total ejected mass $M_{\rm ej}$, and the amount of fast moving ejecta $M_{\rm ej}^{v\geqslant 0.6c}$. For the dynamical ejecta we report the mass-averaged electron fraction $\langle Y_e \rangle$, specific entropy per baryon $\langle s \rangle$, and asymptotic velocity $v_{\rm ej}$. We also give the rms opening angle of the outflow streams from the orbital plane $\theta_{\rm ej} = \sqrt{\langle \theta^2 \rangle}$, and the total kinetic energy of the ejecta $T_{\rm ej}$. All ejecta properties are measured on a sphere with coordinate radius of $300\ G/c^2\ M_\odot \simeq 443$ km.

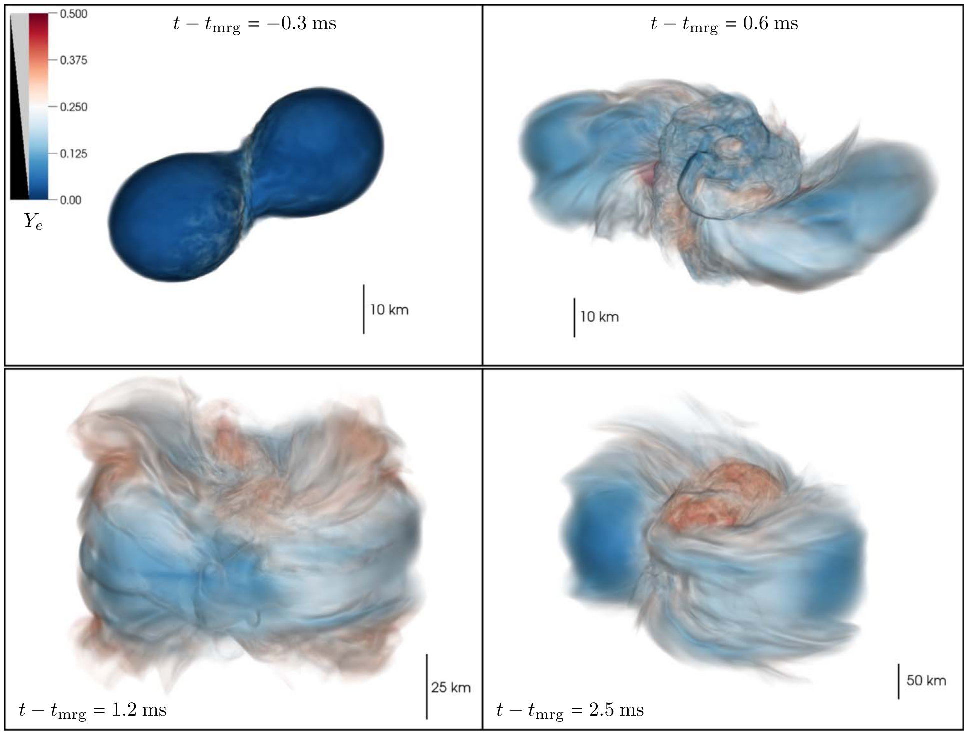

Figure 2. Volume rendering of the electron fraction of the ejecta for the simulation `SFHo_M135135_M0`. The ray-casting opacity is linear in the logarithm of the rest-mass density. From the top left in the clockwise direction, the transparency minimum–maximum in the opacity scale is (10^{11}–10^{14}) g cm^{-3}, (10^{8}–10^{11}) g cm^{-3}, (10^{8}–10^{11}) g cm^{-3}, and (10^{7}–10^{11}) g cm^{-3}. The last panel of this figure should be compared with Figure 14 where we plot a cut of the data in the xz-plane.

3.1. Dynamical Ejecta

We discuss the qualitative properties of the dynamical ejecta in the case of the `SFHo_M135135_M0` binary, which we take as fiducial. Figure 2 summarizes its most salient features. The bulk of the dynamical outflow is contained within a wide ~60° angle from the orbital plane. In the simulations that do not account for neutrino absorption the outflow is neutron rich, with average electron fraction $\langle Y_e \rangle < 0.2$. When neutrino absorption is included in the simulations, as is the case for the `SFHo_M135135_M0` binary, the ejecta is reprocessed to higher values of Y_e, but remains neutron rich $\langle Y_e \rangle < 0.25$.

As shown in Figure 2, the tidal component of the dynamical ejecta is emitted first close to the orbital plane, followed by a more isotropic shock-heated ejecta component. However, the shock-heated component generally has higher velocity, so it rapidly overtakes the tidal component. The two components interact and, as a consequence, the tidal tail is partially reprocessed by weak reactions to slightly higher values of $Y_e \simeq 0.1$. Later, we observe the emergence of a neutrino-driven wind component of the outflow, concentrated at high latitudes. Finally, for this binary, mass ejection shuts off shortly after the formation of a BH.

As the two NSs merge, their inner cores are violently compressed against each other. For some of our models this compression is sufficient to trigger a runaway collapse of the remnant and a BH forms within a single dynamical timescale. However, for most of our binaries the angular momentum of the remnant is sufficiently large to prevent the collapse and the remnant's core undergoes a centrifugal bounce. The bounce starts a cycle of large-scale oscillations of the remnant. As also discussed in detail by Bauswein et al. (2013), for most binaries the most abundant component of the outflow is triggered during the first expansion of the remnant. This is demonstrated in Figure 3,

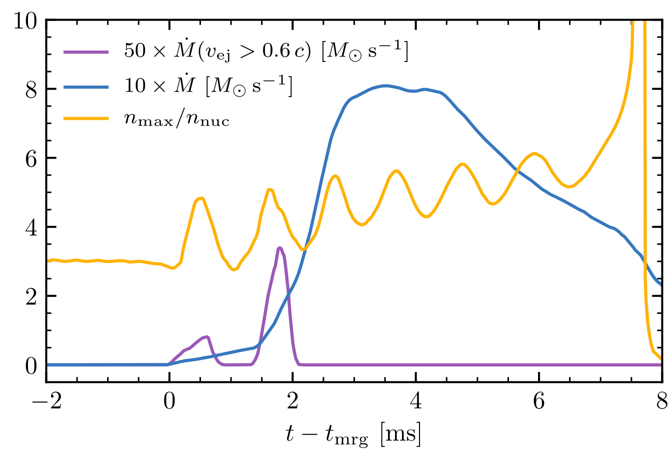

Figure 3. Maximum rest-mass density and outflow rate for the `SFHo_M135135_M0` binary. The outflow rate is computed at a radius of $R = 443$ km and shifted in time by $R\,(0.5c)^{-1}$, $0.5c$ being roughly the 99 percentile of the velocity of the ejecta at radius R. We show both the total outflow rate and the outflow rate of only the material with asymptotic velocity larger than $0.6c$. We find that the bulk of the ejecta is launched when the hypermassive neutron star first bounces back after the merger.

where we show the maximum density and the outflow rates measured for our fiducial `SFHo_M135135_M0` binary. The former is extracted from the flux of unbound material leaving a coordinate sphere with radius $R = 300\ G/c^2\ M_\odot \simeq 443$ km and is retarded according to the velocity of the tip of the ejecta at the detection sphere. As evidenced in the figure, and confirmed by a careful inspection of the multi-dimensional data, the bulk of the outflow is triggered at the time when the merger remnant rebounds. However, after the first bounce, the subsequent oscillations do not produce significant mass ejection. The outflow

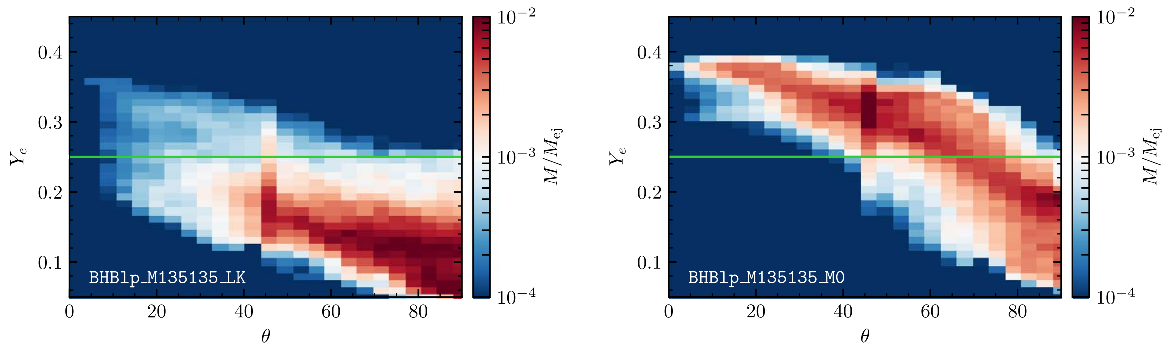

Figure 4. Angular distribution and composition of the ejecta for the 1.35 $M_\odot$ vs. 1.35 $M_\odot$ binary with the BHB$\Lambda\phi$ EOS. Right panel: neutrino cooling only. Left panel: simulation with neutrino absorption. Neutrino irradiation is necessary to generate high-Y_e, polar outflows.

rate remains positive for a few milliseconds as slower material, which has also started expanding during the first ejection episode, reaches the detector.

The inclusion of neutrino re-absorption results in the formation of a new outflow component. This additional outflow stream is composed of material that is ablated from the surface of the HMNS and its accretion disk. This material is reprocessed to $Y_e > 0.25$ and channeled along the polar direction $\theta < 45°$. We remark that this outflow component is absent if neutrino heating is not included (Radice et al. 2016b; Perego et al. 2017a; see also Figure 4 for another representative case). Furthermore, because in our simulation the tidal streams interact with the shocked component of the ejecta, the former also see their Y_e slightly increased with the inclusion of neutrino absorption, as can be seen from the shift in Y_e of the material close to the orbital plane (see region $\theta \simeq 90°$ in Figure 4).

3.1.1. Outflow Properties

Table 2 reports ejecta masses, average electron fraction $\langle Y_e \rangle$, entropy $\langle s \rangle$, asymptotic velocity v_{ej}, and kinetic energy T_{ej} of the ejecta for all models. We also report the rms opening angle of the outflows about the equatorial plane θ_{rms}. Note that the definition of θ_{rms} implies that at least 75% of the ejecta is confined within $2\theta_{rms}$ of the orbital plane.

The dynamical ejecta masses are not fully converged in our simulations. From the comparison of results obtained at different resolutions we estimate the relative errors to be of the order of ~50%. In the following, we will assume the uncertainty in the ejecta masses to be

$$\Delta M_{ej} = 0.5\, M_{ej} + (5 \times 10^{-5}) M_\odot. \tag{17}$$

On the other hand, other ejecta properties, such as the average asymptotic velocities, the entropy, and the composition, appear to be converged (see Appendix A for a more detailed discussion).

Despite the large inferred numerical uncertainty, we find overall good qualitative agreement between the ejecta masses estimated from our simulations and others presented in the literature. However, quantitative differences are present. In particular, we compare dynamical ejecta masses estimated for the $(1.35 + 1.35)\, M_\odot$ binaries with the DD2 and the SFHo EOSs, which have been considered in several previous works and by us. The results are reported in Table 3. Sekiguchi et al. (2015, 2016) considered these binaries with and without neutrino absorption. In the former case they reported ejecta masses about three times larger than what we find. The disagreement is somewhat less severe for the simulations with neutrino absorption included. Lehner et al. (2016) and Bovard et al. (2017) performed simulations only with neutrino cooling and reported ejecta masses in good agreement with those of our `DD2_M135135_LK` and `SFHo_M135135_LK` binaries. Note, however, that the latter study also employed the `WhiskyTHC` code, albeit with a different grid setup and lower resolution, so it does not represent a completely independent confirmation of our results. Finally, Bauswein et al. (2013) performed simulations using a smoothed particle hydrodynamics (SPH) code with an approximate treatment of GR and neglected the effect of neutrinos. They reported ejecta mass of $0.48 \times 10^{-2} M_\odot$ for the SFHo binary. This is in good agreement with our value of $0.35 \times 10^{-2} M_\odot$, especially when taking into account that neglecting neutrino cooling results in an overestimate of the ejecta mass (Radice et al. 2016b). On the other hand, the ejecta mass they reported for the DD2 EOS is a factor ~10 larger than what we infer from our simulations.

Dietrich & Ujevic (2017) derived empirical formulas predicting the ejecta mass and velocity from binary NS mergers extending previous work on the ejecta from BHNS mergers (Foucart 2012; Kawaguchi et al. 2016).[7] They calibrated their fitting formulas using data from Hotokezaka et al. (2013b), Bauswein et al. (2013), Dietrich et al. (2015, 2017b), Sekiguchi et al. (2016), and Lehner et al. (2016). Note that most of these data completely neglected neutrino effects (both emission and absorption). Moreover, as we discuss above, some of these works predict rather different ejecta masses for the same binaries. The resulting fits have been used in Abbott et al. (2017b) to estimate the contribution of the dynamical ejecta to the kilonova that followed GW170817 and, more recently, by Coughlin et al. (2018) to constrain the tidal deformability of the binary progenitor to GW170817. Note, however that Coughlin et al. (2018) used a modified fit for $\log(M_{ej}/M_\odot)$.

We recalibrate the model of Dietrich & Ujevic (2017) using our data. We only consider the simulations performed without neutrino heating and at our reference resolution $h = 185$ m, so as to have a homogeneous data set. We refer to this subset of the runs as being our fiducial subset of simulations. The omission of neutrino re-absorption could result in a systematic underestimate of the ejecta mass by up to factors of a few (see Table 2). However, we expect the qualitative trends to be robust.

[7] See Foucart et al. (2018b) for updated fits to BHNS merger data.

Table 3
Dynamical Ejecta Masses Reported in the Literature for the $(1.35 + 1.35)\,M_\odot$ Binary Simulated with Either the DD2 or the SFHo EOS

EOS	ν cool.	ν abs.	$M_{\rm ejecta}$ $[10^{-3}\,M_\odot]$	References
DD2	✓	⋯	0.3	This work
DD2	✓	✓	1.4	This work
DD2	⋯	⋯	3.1	Bauswein et al. (2013)
DD2	✓	⋯	0.6	Bovard et al. (2017)
DD2	✓	⋯	0.4	Lehner et al. (2016)
DD2	✓	⋯	0.9	Sekiguchi et al. (2015)
DD2	✓	✓	2.1	Sekiguchi et al. (2015)
SFHo	✓	⋯	3.5	This work
SFHo	✓	✓	4.2	This work
SFHo	⋯	⋯	4.8	Bauswein et al. (2013)
SFHo	✓	⋯	3.5	Bovard et al. (2017)
SFHo	✓	⋯	3.4	Lehner et al. (2016)
SFHo	✓	⋯	10.0	Sekiguchi et al. (2015)
SFHo	✓	✓	11.0	Sekiguchi et al. (2015)

Note. For each reported value we indicate the reference and whether the simulation included heating and compositional changes due to neutrino emission (ν cool) and/or absorption (ν abs). There are differences of factors of a few among published results.

Following Dietrich & Ujevic (2017) we fit the ejecta mass as

$$\frac{M_{\rm ej;fit}}{10^{-3}M_\odot} = \left[\alpha\left(\frac{M_b}{M_a}\right)^{1/3}\left(\frac{1-2C_a}{C_a}\right) + \beta\left(\frac{M_b}{M_a}\right)^n + \gamma\left(1-\frac{M_a}{M_a^*}\right)\right]M_a^* + (a \leftrightarrow b) + \delta, \tag{18}$$

where M_a, M_b and M_a^*, M_b^* are the NS gravitational and baryonic masses, respectively, and

$$C_{a,b} = \frac{GM_{a,b}}{c^2 R_{a,b}} \tag{19}$$

are the stars' compactnesses. We use Equation (17) to estimate the numerical uncertainty in the ejecta mass and we use a standard least-squares fit to determine the coefficients α, β, γ, δ, and n in Equation (18). We find

$$\alpha = -0.657, \qquad \beta = 4.254, \qquad \gamma = -32.61, \tag{20}$$

$$\delta = 5.205, \qquad n = -0.773. \tag{21}$$

We find differences of ~50%–100% compared to the values reported by Dietrich & Ujevic (2017). In particular, our fit systematically predicts lower dynamical ejecta masses compared to Dietrich & Ujevic (2017).

The right panel of Figure 5 shows the ejecta masses from our fiducial subset of simulations plotted against the predicted ejecta masses from Equation (18). Overall, we find that $M_{\rm ej}$ correlates with $M_{\rm ej;fit}$, suggesting that the model of Dietrich & Ujevic (2017) captures some of the physics behind the mass ejection. However, there are differences between the values measured in simulations and those predicted by the fit as large as ~200%. This is a factor of a few in excess of the finite-resolution uncertainties we estimate for our simulations. We note that Dietrich & Ujevic (2017) also reported similarly large fit residuals. More worrisome is the fact that the model seems to be systematically missing trends in the data. For example, it over-predicts the ejecta for most of the massive DD2 binaries. This suggests that Equation (18) does not capture all of the physical effects relevant for the mass ejection.

We fit the mass-weighted average asymptotic velocity $v_{\rm ej}$ of the ejecta using an expression similar to that used by Dietrich & Ujevic (2017):

$$v_{\rm ej;fit} = \left[\alpha\left(\frac{M_a}{M_b}\right)(1+\gamma C_a)\right] + (a \leftrightarrow b) + \beta. \tag{22}$$

On the basis of the comparison between results obtained at different resolution, we use a constant value $\Delta v_{\rm ej} = 0.02c$ as fiducial uncertainty for the ejecta velocity and perform a least-squares fit of our fiducial subset of simulations using Equation (22). When doing so, we exclude simulations with ejecta masses smaller than $10^{-5}\,M_\odot$, since the ejecta properties cannot be reliably measured in those cases. Note that changing the value of $\Delta v_{\rm ej}$ has no effect on the results of the fitting procedure. Using a standard least-squares method we find

$$\alpha = -0.287, \qquad \beta = 0.494, \qquad \gamma = -3.000. \tag{23}$$

These coefficients are in good agreement with those reported by Dietrich & Ujevic (2017) for the ejecta velocity in the orbital plane. This suggests that the ejecta velocity predicted by the simulations are robust. We also find good qualitative agreement between the ejecta velocities from simulations and those predicted by the model, as shown in the right panel of Figure 5. However, there is a significant spread with residuals as large as $0.1c$.

Bauswein et al. (2013) compared dynamical ejecta mass obtained for the $(1.35 + 1.35)\,M_\odot$ binary using different EOSs and found that it was inversely proportional to the NS radii, suggesting that large ejecta masses could be produced in the case of compact NSs. This was used in Nicholl et al. (2017) to suggest that the large inferred ejecta mass for GW170817 implies a small NS radius $R_{1.35} \lesssim 12$ km. The strongest support for the correlation found by Bauswein et al. (2013) comes from binaries that were simulated with an approximate treatment of thermal effects. Our results (Table 2) also indicate that softer EOSs might produce more ejecta. However, we do not find evidence for a clear correlation that would support the conclusions of Nicholl et al. (2017).

Figure 6 shows ejecta masses and velocities as a function of the tidal deformability of the binary $\tilde\Lambda$ (e.g., Flanagan & Hinderer 2008; Favata 2014). By comparing results from simulations with different EOSs we confirm that there is some dependence of the ejecta mass on the stiffness of the EOS, with softer EOSs such as SFHo and LS220 producing more ejecta than BHB$\Lambda\phi$ and DD2. We also find indications that prompt BH formation results in smaller than average dynamical ejecta masses. However, we are not able to identify a relation between the ejecta masses and properties of the EOS such as the radius of a reference NS or the tidal deformability. This is not too surprising given that most of the dynamical ejecta in our simulations is the result of the centrifugal bounce of the merger remnant. Its characteristics are likely to depend on thermal effects and details of the EOS at high densities that are not captured by $\tilde\Lambda$. Our data exclude the possibility of constraining $\tilde\Lambda$ from the measurement of the properties of the dynamical ejecta alone. On the other hand, it might be possible to use kilonova observations to constrain other properties of

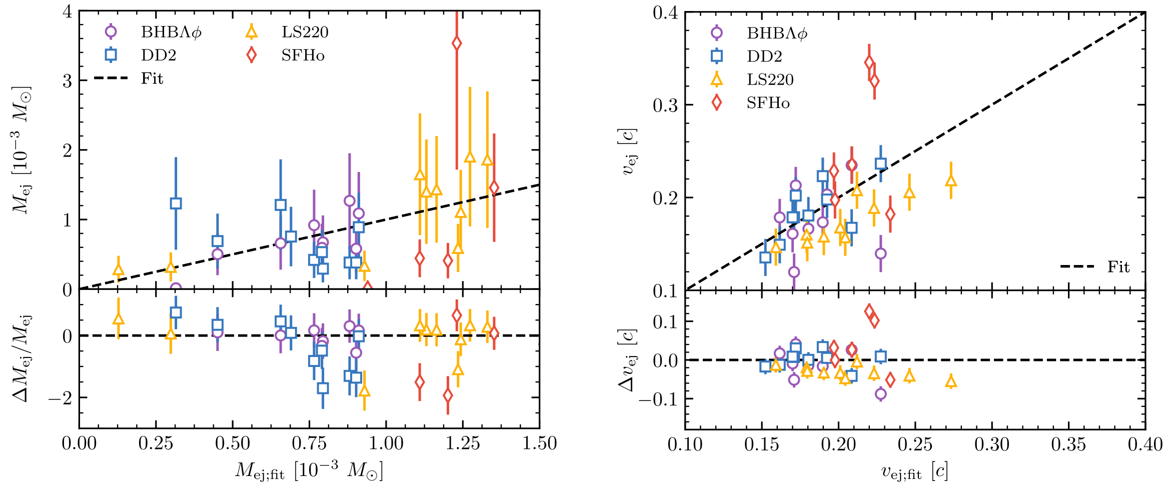

Figure 5. Dynamical ejecta masses (left panel) and velocities (right panel) vs. their fit according to Equations (18) and (22). The data points show the results from our fiducial subset of simulations, which have also been used to re-calibrate the fitting coefficients. For the velocity fit, we only include/plot models with total ejecta mass larger than $5 \times 10^{-5}\,M_\odot$. There is a correlation between $M_{\rm ej}$ and $v_{\rm ej}$ as extracted from our simulations and their predictors $M_{\rm ej;fit}$ and $v_{\rm ej;fit}$.

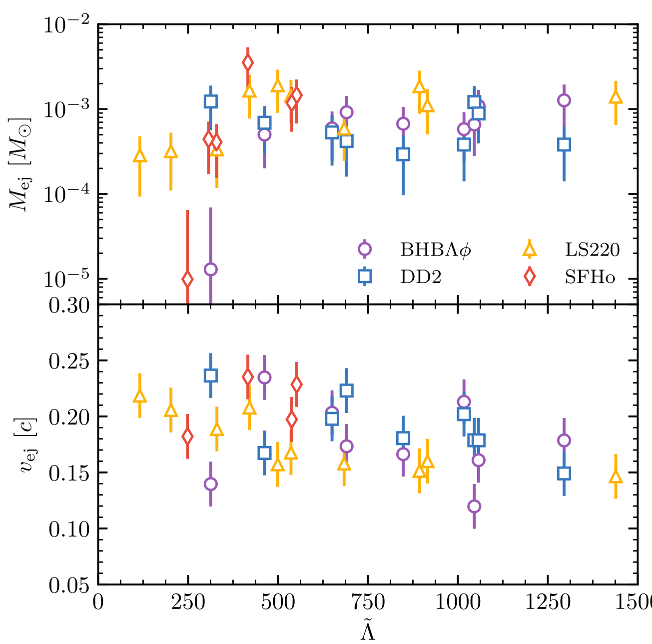

Figure 6. Dynamical ejecta masses $M_{\rm ej}$ and asymptotic velocities $v_{\rm ej}$ as a function of the tidal parameter $\tilde\Lambda$. The data points show the results from our fiducial subset of simulations. No correlation is found between the ejecta mass and $\tilde\Lambda$. There is, however, a weak tentative inverse correlation between the asymptotic velocity of the ejecta and $\tilde\Lambda$.

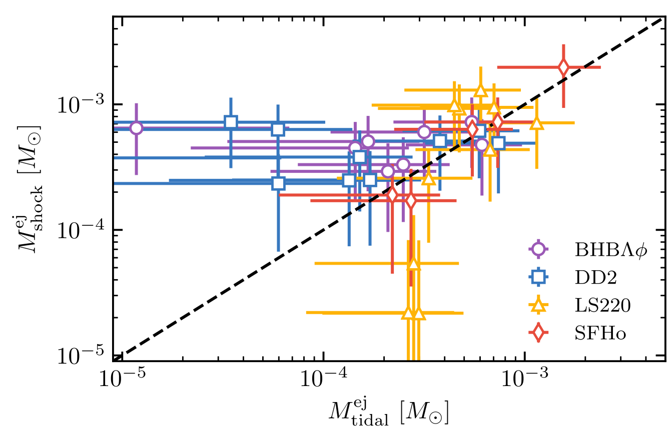

Figure 7. Mass of shock-heated ejecta with $s > 10\,k_{\rm B}$ plotted against the mass of the cold ejecta. The center left part of the figure is tentatively populated by stiff EOSs. Tidally dominated ejecta dominates over shock-heated ejecta only for binaries with prompt BH formation (lower middle part of the figure).

the binary, for instance using an improved version of Equation (18), and thus indirectly improve the bounds on $\tilde\Lambda$ by restricting the priors used in the GW data analysis. However, these applications would necessarily require more precise theoretical predictions than those currently available.

Other properties of the outflow, such as proton fraction and entropy, also show some dependence on the EOS. The reason is that different EOSs result in different relative amounts of shocked and tidal ejecta. This is quantified in Figure 7, where we show the mass of the tidal and shocked ejecta for our fiducial subset of simulations, i.e., those with only neutrino cooling and $h = 185$ m. For this analysis we tentatively identify as shocked ejecta all of the unbound material crossing a coordinate sphere with radius $\simeq$443 km and having specific entropy per baryon larger than $10\,k_{\rm B}$. Material ejected with smaller entropies is assumed to be originating from tidal interactions. We find that stiff EOSs, such as BHBΛϕ and DD2, typically have smaller $M^{\rm ej}_{\rm tidal}$ than softer EOSs, such as LS220 and SFHo. Softer EOSs also eject more mass overall. The shocked component of the dynamical ejecta dominates the overall mass ejection for most of the binaries we have considered. The only exceptions are cases where BH formation occurs shortly after merger ($\lesssim$1 ms) so that there is no centrifugal bounce of the remnant.

The balance between shocked and tidal ejecta is also dependent on the binary mass ratio (see Section 4.1). On the one hand, binaries with larger mass asymmetry produce more massive tidal outflow streams. On the other hand, asymmetric binaries result in the partial disruption of the secondary star during merger, less violent mergers, and smaller amount of shocked ejecta (Table 2; Bauswein et al. 2013; Hotokezaka et al. 2013b; Lehner et al. 2016; Sekiguchi et al. 2016; Bovard et al. 2017; Dietrich et al. 2017b).

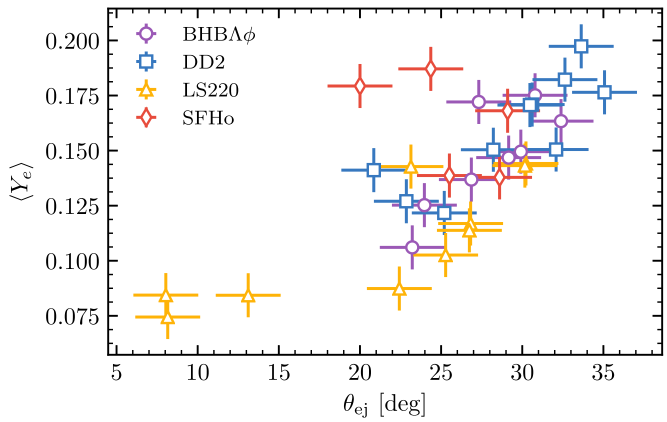

Figure 8. Average electron fraction $\langle Y_e \rangle$ vs. rms angular spread $\theta_{\rm ej}$ of the ejecta. The data points show the results from our fiducial subset of simulations. We only include models with total ejecta mass larger than $5 \times 10^{-5}\,M_\odot$. The shock-heated component of the ejecta is absent in the cases with prompt BH formation.

We conclude that the balance between tidal ejecta and shocked ejecta is set by a complex interplay between microphysical effects and binary properties.

Tidally driven outflows have low average Y_e and are preferentially concentrated close to the orbital plane. Conversely, the shocked ejecta are spread over a larger angle of the orbital plane and have larger $\langle Y_e \rangle$, so a correlation between $\theta_{\rm ej}$ and $\langle Y_e \rangle$ is expected. This is shown in Figure 8. For clarity, the figure only shows our fiducial subset of simulations, for which numerical and microphysical parameters have been set in a consistent way. The binaries in the lower left corner of the figure are LS220 binaries resulting in prompt BH formation. These are the same binaries appearing in the lower part of Figure 7. The outflows from these binaries are dominated by the tidal ejection of material. The two outliers with $\theta_{\rm ej} = 20°$–$25°$ are `SFHo_M140140_LK` and `SFHo_M144139_LK`, which also undergo prompt collapse, but have outflows mostly driven by shocks. With the possible exception of the binaries resulting in prompt BH formation, all others show a clear correlation between $\langle Y_e \rangle$ and $\theta_{\rm ej}$. This suggests that a constraint on the opening angle of the dynamical ejecta, perhaps obtained by combining the observation of multiple systems with different orientations, could constrain the strength of the bounce of the massive NS after merger and the composition of the dynamical ejecta.

Overall, we find good qualitative agreement between our results for the dynamical ejecta and those reported in previous studies that adopted a more idealized treatment for the EOSs of NSs and/or approximate GR (Bauswein et al. 2013; Hotokezaka et al. 2013a; Dietrich et al. 2017a, 2017b). At the same time, there are substantial quantitative differences in the dynamical ejecta mass and properties from those studies, as well as with other works that considered a limited number of binary configurations, but included full-GR and neutrino effects (Sekiguchi et al. 2015, 2016). The total ejecta mass is also not fully converged in our simulations (Table 2). While there appear to be robust trends and correlations between ejecta properties, binary parameters, and the EOSs of NSs, more comprehensive and better resolved studies would be needed to create reliable quantitative models of the dynamical ejecta.

3.1.2. Fast Moving Ejecta

Metzger et al. (2015) re-analyzed data from Bauswein et al. (2013) and identified 106 SPH particles, corresponding to $\sim 10^{-4}\,M_\odot$ of material, that were dynamically ejected with velocities in excess of 0.6c. If indeed present, these fast-moving ejecta would expand sufficiently rapidly to still contain a significant fraction of free neutrons at freeze-out. The decay of the neutrons in the outermost part of the ejecta would then produce a bright UV/optical counterpart to the merger on a timescale of several minutes to an hour (Kulkarni 2005; Metzger et al. 2015). On the other hand, because of the small number of SPH particles, it cannot be excluded that this fast component of the ejecta is due to numerical noise, as also recognized by Metzger et al.

More recently, a fast-moving component of the dynamical ejecta was proposed as a possible origin for the synchrotron radiation detected from GW170817 in the first $\sim$100 days (Mooley et al. 2018a; Hotokezaka et al. 2018b). This interpretation is currently disfavored on the light of more recent observations showing an abrupt decline in the source luminosity in all bands (Alexander et al. 2018) and very long baseline interferometry observations showing apparent superluminal motion of the radio source indicative of collimation of the outflow (Ghirlanda et al. 2018; Mooley et al. 2018b). Nevertheless, this fast-moving component of the outflows was identified by Hotokezaka et al. (2018b) using data from the simulations of Kiuchi et al. (2017). The latter simulations, however, employed piecewise polytropic fits to the cold NS EOS augmented with an ideal-gas component to describe thermal effects. These approximations affect the thermodynamical properties of the shocks responsible for the ejection of this material (Bauswein et al. 2013), so they need to be independently verified.

Our previous simulations (Radice et al. 2016b) did not show evidence for the presence of a fast-moving component of the ejecta. However, we only considered one equal mass configuration with $M_a = M_b = 1.39\,M_\odot$ simulated using the LS220 EOS, while Metzger et al. (2015) considered a large sample of EOSs and binary masses. In our new simulations we find evidence for a fast-moving component of the outflow with asymptotic velocities in excess of 0.6c (Table 2). The amount of fast-moving ejecta strongly depends on the EOS and other binary parameters. For instance, for total binary masses up to $2.8\,M_\odot$, with the exception of simulations performed with viscosity, discussed in a companion paper (Radice et al. 2018b), the LS220 EOS does not seem to predict an appreciable number of fast outflows, in agreement with Radice et al. (2016b). On the other hand, binaries simulated with the BHBΛϕ, DD2, or SFHo EOSs, as well as higher-mass LS220 binaries, typically eject $\sim 10^{-6}$–$10^{-5}\,M_\odot$ of fast-moving material. This is still one or two orders of magnitude less than reported in Metzger et al. (2015), but suggests that the ejection of at least a small amount of fast material does indeed take place during NS mergers. That said, given the small overall mass involved, we cannot completely exclude its origin as being numerical. Indeed, we find large variations in the amount of the fast-moving ejecta with resolution, and much better-resolved simulations would be needed to fully quantify the mass of these fast outflows. On the other hand, the smooth distribution of the ejecta in velocity space, shown in Figure 9, seems to suggest that the properties of the outflows are reasonably well captured even down to these masses.

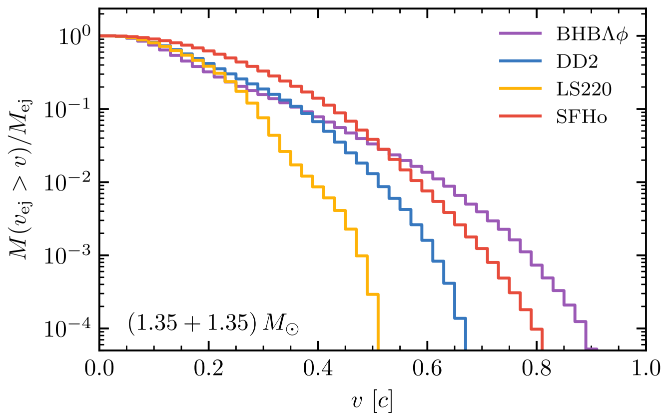

Figure 9. Cumulative distribution of ejecta velocities for the $(1.35 + 1.35)\,M_\odot$ binary with four EOSs and at the reference resolution. Neutrino re-absorption has not been included in these simulations.

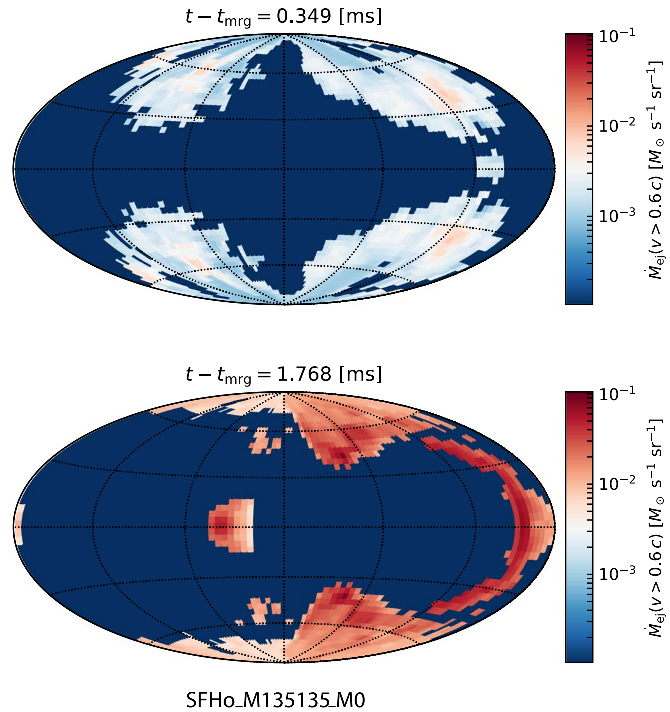

Figure 10. Angular distribution of the flux of ejecta with asymptotic velocities larger than $0.6c$ for the `SFHo_M135135_M0` binary. The data are extracted on a coordinate sphere with radius 443 km. For clarity, time is retarded in the same way as in Figure 3. We find two distinct episodes resulting in the production of fast ejecta: one associated with the merger and one associated with the first bounce of the remnant.

We discuss the possible observational consequences of the fast-moving component of the ejecta in Section 5. Here, we focus on their origin. Metzger et al. (2015) suggested that shocks generated at the time of the collision between the NSs could be accelerated by the steep density gradient at the surface of the remnant and drive outflows with trans-relativistic velocities. This is a scenario first considered by Kyutoku et al. (2014) who studied its possible high-energy signatures. The same scenario has also been recently revisited in detail by Ishii et al. (2018). They used high-resolution 1D Lagrangian simulations to resolve the shock acceleration and predict the amount of ejected material. They found that this mechanism can indeed produce free neutrons. However, they found the amount of free neutrons that can be produced in this way to be $\sim 10^{-7}$–$10^{-6}\,M_\odot$. This might be insufficient to explain the results of Metzger et al. (2015). On the other hand, the values found by Ishii et al. (2018) are not inconsistent with our data.

Comparable mass binaries simulated with the SFHo EOS, the softest in our set, result in the most violent mergers. As the NSs collide, material is squeezed out from the collisional interface at large velocities, as in the simulation discussed by Metzger et al. (2015). This is evident from Figure 3, where we show the outflow rate of the fast-moving component of the ejecta with asymptotic velocities $v_{\rm ej} > 0.6c$. Because of its peculiar origin, this outflow component is preferentially channeled to high latitudes and in directions not obstructed by the NSs. This is shown, in the case of the `SFHo_M135135_M0` binary, in the upper panel of Figure 10. However, this first clump of material amounts only to about a quarter of all of the fast ejecta. Most of the fast-moving ejecta instead appears to originate when the shock launched from the first bounce of the remnant breaks out of the forming ejecta cloud, as indicated in Figure 3. This second component of the fast ejecta is also highly anisotropic, but preferentially concentrated close to the orbital plane, as shown in the lower panel of Figure 10 for the `SFHo_M135135_M0` binary. This is possibly because of the oblate shape of the merger debris cloud which favors the acceleration of the material close to the orbital plane.

Smaller mass ratio binaries, or binaries simulated with other EOSs, do not, however, show evidence for an early fast-ejecta component from the collisional interface between the NSs. For these binaries the fast-moving component of the ejecta is entirely constituted of material accelerated after the bounce of the merger remnant. This material is preferentially confined to the region close to the orbital plane, as shown in Figure 11. We stress that this angular distribution is inconsistent with the ejecta originating at the collisional interface between the NSs. The reason for the different behavior of more unequal mass binaries and/or binaries with stiffer EOSs is that the former result in less violent collisions than those predicted for comparable mass NSs with the SFHo EOS, either because of the larger NS radii, or because of the partial disruption of the secondary star shortly before merger. We note that the inclusion of neutrino heating only results in a modest quantitative correction to the distribution of the fast-moving component of the ejecta, but the overall qualitative picture is unchanged.

We find the distribution of the fast-component of the ejecta to be not only anisotropic in latitude, but also in the azimuthal direction, as shown in Figure 12. The fast-moving material forms narrow streams that cover only a small fraction of area of a sphere centered at the location of the binary merger. In contrast, the overall ejecta distribution is almost uniformly spread in the azimuthal direction (e.g., Bovard et al. 2017). We remark that non-spinning, equal-mass binaries have a discrete rotational symmetry of 180° around the orbital angular momentum axis. However, this symmetry is typically broken at the time of the merger, when turbulence operating in the shear layer between the two NSs can exponentially amplify small initial asymmetries, such as those due to floating-point truncation in the simulations (Paschalidis et al. 2015; Radice et al. 2016a). This is reflected in the asymmetry of the fast-moving tail of the dynamical ejecta and is another indication of the fact that the bulk of the fast-moving ejecta is launched with

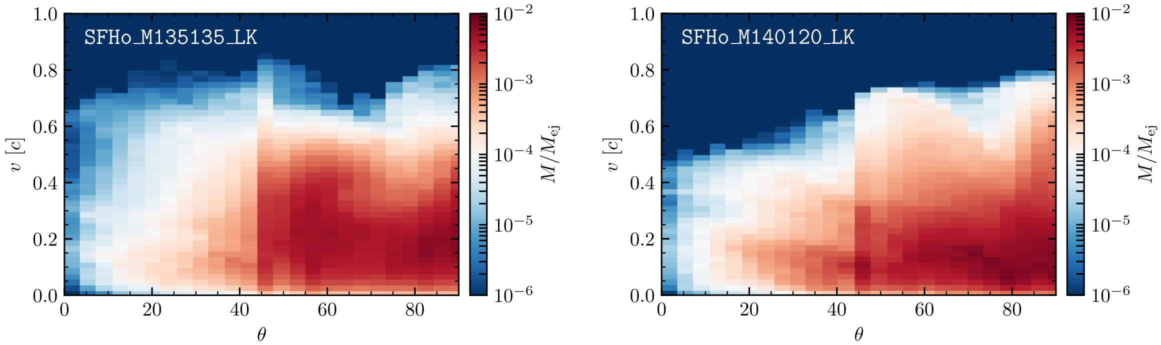

Figure 11. Angular distribution and asymptotic velocity of the ejecta for the $(1.35 + 1.35)\,M_\odot$ and $(1.4 + 1.2)\,M_\odot$ binaries with the SFHo EOS simulated without neutrino re-absorption. $\theta = 0$ corresponds to the polar axis, while $\theta = 90°$ is the orbital plane. The data are extracted on a coordinate sphere with radius 443 km. The fast-moving tail of the ejecta is confined to a region close to the orbital plane for the unequal mass `SFHo_M140120_LK` binary (right panel), but it is somewhat more isotropically distributed for the equal mass `SFHo_M135135_LK` binary (left panel).

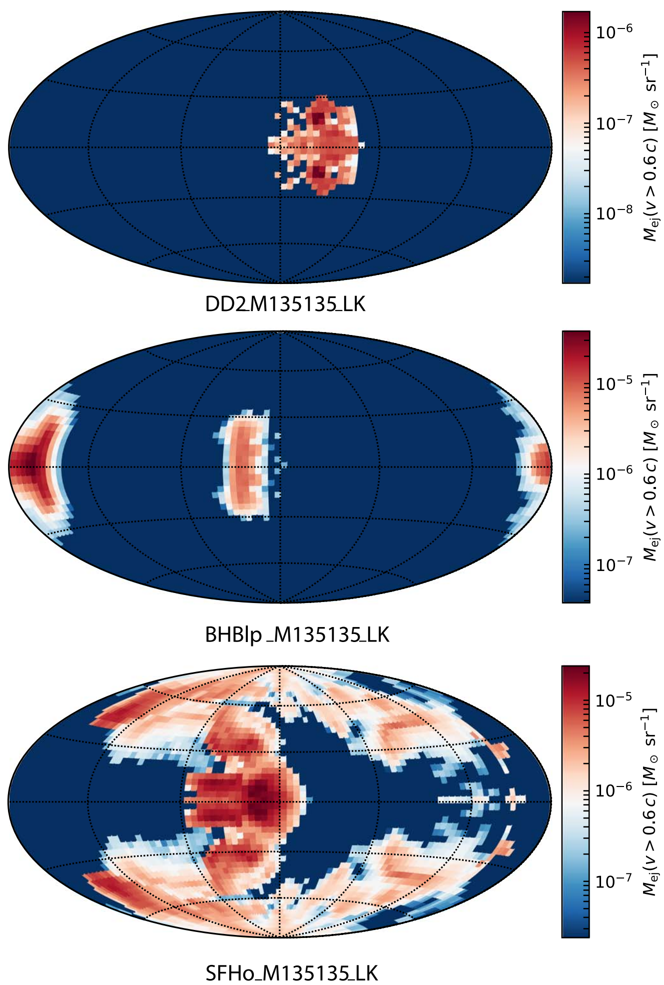

Figure 12. Angular distribution of the ejecta with asymptotic velocities larger than $0.6c$ for $(1.35 + 1.35)\,M_\odot$ binaries simulated without neutrino re-absorption, and at the fiducial resolution. The data are extracted on a coordinate sphere with radius 443 km. The `LS220_M135135_LK` binary is not shown, since it does not produce an appreciable amount of fast-moving ejecta. The fast-moving component of the outflow is anisotropic and covers a relatively small portion of the sky around the binary, especially in the case of the BHB$\Lambda\phi$ and DD2 binaries.

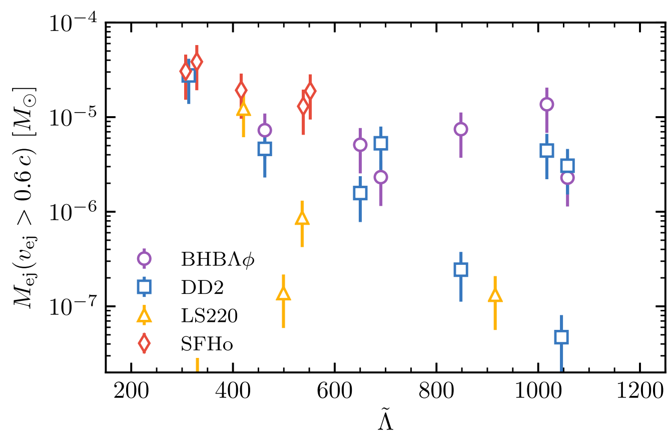

Figure 13. Fast-moving component of the ejecta plotted against the binary tidal deformability $\tilde\Lambda$. The data points show the results from our fiducial subset of simulations. Note that several binaries produce no appreciable amount of fast-moving ejecta and are not seen in the figure. There is only a tentative correlation between the mass of the fast-moving ejecta and the tidal deformability of the binary.

some delay from the merger. Note that the early fast ejecta for the equal-mass binaries with the SFHo EOS, which instead originates at the time of the merger, is symmetric (see Figure 10).

We report the total mass of the ejecta with $v_{\rm ej} > 0.6c$ in Figure 13. The error bars are estimated following Equation (17). The motivation for this choice is that, while we find relatively large numerical uncertainties in the total ejecta mass, the relative distribution of the ejecta as a function of velocity appears to be robust (see Appendix A). Consequently, the numerical uncertainty in the total ejecta mass should be well correlated with that of the fast component. Each simulation is labeled by the tidal deformability of the binary $\tilde\Lambda$. The tidal parameter $\tilde\Lambda$ is related to the compactness of the binary and should correlate with the strength with which different NSs binaries collide at the time of merger. We might expect that $\tilde\Lambda$ should also correlate with the amount of fast ejecta produced during the collision between the two stars. Indeed, we find that there is a weak correlation between the two in Figure 13. However, there are systematic effects that are not captured by $\tilde\Lambda$. For instance, the BHB$\Lambda\phi$ and the DD2 binaries have very close compactnesses, since the two EOSs are identical for NSs with gravitational mass $M \lesssim 1.5\,M_\odot$. However, the BHB$\Lambda\phi$ binaries typically produce a significantly larger amount of fast-moving ejecta compared to the DD2 binaries. The reason is likely the more violent bounce of the merger remnant due to the formation of Λ hyperons in the aftermath of the BHB$\Lambda\phi$ binary mergers (Radice et al. 2017). Perhaps more importantly, there are several binaries, spanning

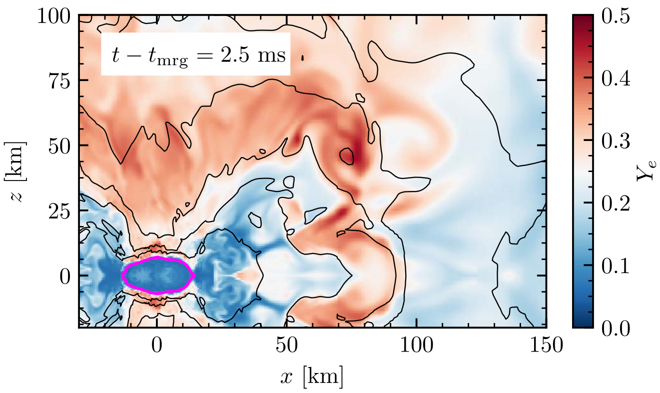

Figure 14. Electron fraction and density in the *xz*-plane for the `SFHo_M135135_M0` simulation. The thin black contours enclose regions with density larger than 10^6, 10^7, 10^8, 10^9, 10^{10}, and 10^{11} g cm^{-3}. The thick magenta line encloses the region with density larger than 10^{13} g cm^{-3}. This figure should be compared with the last panel of Figure 2 where a volume rendering of the same data is shown.

a wide range of $\tilde{\Lambda}$, that do not produce any appreciable amount of fast-moving ejecta.

3.2. Secular Ejecta

Part of the tidal tails from the NSs remains bound to form a rotationally supported disk around a central remnant more precisely defined below. In the cases in which the remnant survives for more than about one millisecond, we observe the formation of hot, $\sim$10–20 MeV, streams of material expelled from what is originally the interface region between the NSs. This material assembles into an excretion disk. Consequently, there is a correlation between the lifetime of the remnant and the remnant disk mass (Radice et al. 2018c); see also Table 2.

The disks are geometrically thick and moderately neutron rich (see Figure 14; Siegel & Metzger 2018). We observe the propagation of $m = 2$ spiral density waves originating as the streams from the massive NS remnant impact the disk. After the first 10–20 ms from the merger, these streams subside, and $m = 1$ spiral density waves, induced by the one-armed spiral instability of the remnant NS (Paschalidis et al. 2015; East et al. 2016; Radice et al. 2016a), become dominant.

If the merger does not result in the formation of a BH within a few dynamical timescales, the remnant is composed of a relatively slowly rotating inner core surrounded by a rotationally supported envelope (Shibata et al. 2005; Kastaun et al. 2016; Ciolfi et al. 2017; Hanauske et al. 2017). In particular, regions with rest-mass densities below $\simeq 10^{13}$ g cm^{-3} are mostly rotationally supported (Hanauske et al. 2017). Note that the rotational structure of the remnant might be strongly affected by the effective shear viscosity arising due to the turbulent fluid motion in the remnant (Radice 2017; Shibata et al. 2017b; Fujibayashi et al. 2018; Kiuchi et al. 2018; Radice et al. 2018a). In our analysis we define as the central part of the remnant the region with $\rho_0 \geqslant 10^{13}$ g cm^{-3}, and we estimate the remnant disk mass $M_{\rm disk}$ from the integral of the rest-mass density of the region with $\rho_0 < 10^{13}$ g cm^{-3}. We remark that the same criterion has also been adopted by Shibata et al. (2017a). Furthermore, as shown in Figure 14, the density threshold 10^{13} g cm^{-3} does indeed approximately correspond to the boundary of the centrally condensed remnant. Our results are given in Table 2. Unfortunately, the 3D output necessary to estimate the disk mass in post-processing was accidentally deleted for six of our simulations. For those cases the disk masses are not given.

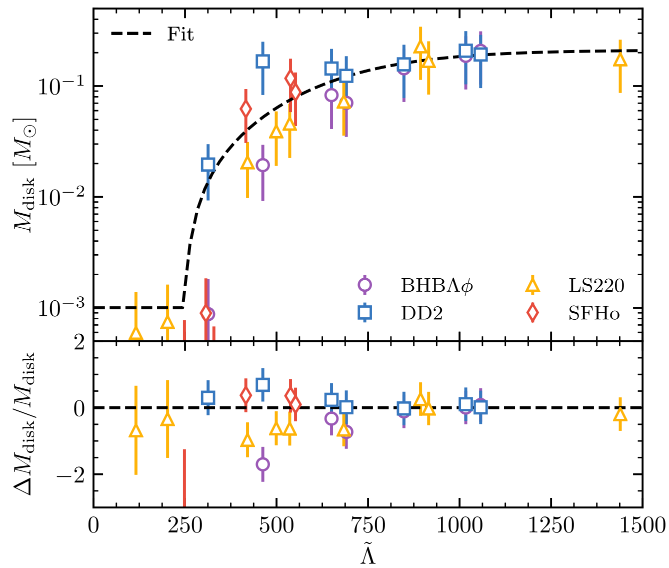

Figure 15. Remnant disk masses as a function of the tidal parameter $\tilde{\Lambda}$. The data points show the results from our fiducial subset of simulations. Disk formation is suppressed in the case of prompt BH formation, corresponding to small $\tilde{\Lambda}$. The final disk masses saturate for large values of $\tilde{\Lambda}$.

Figure 14 shows the electron fraction and the density contours shortly after merger, during the formation of the accretion disk. At this time the disk has not yet reached its maximum extent and is expanding behind the cloud of the dynamical ejecta. The latter can be recognized for their higher electron fraction and are located at radii $\gtrsim$75 km. The neutron-rich outflow visible at radii $\gtrsim$100 km is part of the tidal tail, while the higher Y_e material between the forming accretion disk and the tidal tail is part of the outflow generated during the first bounce of the merger remnant.

We find that the remnant disk masses tightly correlated with the tidal deformability of the binary $\tilde{\Lambda}$. This is shown in Figure 15 where we plot the disk masses for our fiducial models. The error bars are estimated from the comparison of simulations performed at different resolutions (see Table 2). In particular, we estimate the uncertainty on the disk mass due to numerical errors to be $\sim$30%. To be conservative, we estimate the uncertainties on the disk masses as

$$\Delta M_{\rm disk} = 0.5\, M_{\rm disk} + (5 \times 10^{-4}) M_\odot. \tag{24}$$

We remark that the error bars only account for finite-resolution uncertainties and we cannot exclude that missing physics, or more extreme binaries with larger mass asymmetries and/or extreme spins, could deviate from the trend shown in Figure 15. Moreover, because a significant fraction ($\sim$30%–90%) of the disk is accreted promptly after BH formation, the transition between low- and high-mass disks visible in Figure 15 would likely become sharper if we could evolve all of the hypermassive remnants to collapse.

Notwithstanding these caveats, we find that our data are reasonably well fitted with the simple expression

$$\frac{M_{\rm disk}}{M_\odot} = \max\left\{10^{-3},\, \alpha + \beta \tanh\left(\frac{\tilde{\Lambda} - \gamma}{\delta}\right)\right\} \tag{25}$$

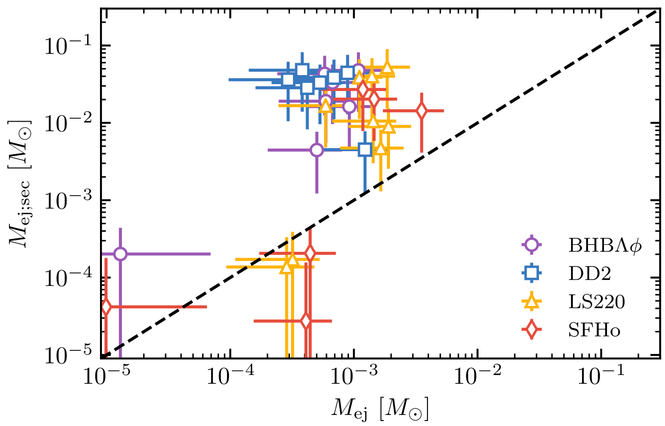

Figure 16. Dynamical ejecta $M_{\rm ej;dyn}$ vs. secular ejecta masses $M_{\rm ej;sec}$. With the exception of the prompt BH formation cases that are able to expel at least a few $10^{-4}\,M_\odot$ in dynamical ejecta, the secular ejecta dominate over the dynamical ejecta.

with fitting coefficients $\alpha = 0.084$, $\beta = 0.127$, $\gamma = 567.1$, and $\delta = 405.14$. In the case of GW170817, the amount of ejecta estimated from the modeling of the kilonova signal $\sim 0.05\ M_\odot$ is about an order of magnitude too large to be explained by the dynamical ejecta. This suggests that most of the material powering the kilonova should have been produced during the viscous evolution of the accretion disk.

This finding is in agreement with the results from long-term GRMHD simulations of postmerger disks that show that up to $\sim$40% of the accretion disk can be ejected over the viscous timescale (Siegel & Metzger 2017; Fernández et al. 2019). According to this scenario, $M_{\rm disk}$ should have been larger than at least $\sim 0.1\ M_\odot$. This, in turn, implies that $\tilde{\Lambda}$ for GW170817 should have been larger than about 400. Another possibility, which however we cannot currently test with our data, is that the progenitor binary to GW170817 had a large mass asymmetry. Under these conditions it has been suggested that the merger could still produce a massive disk even for compact configurations (Shibata et al. 2003; Shibata & Taniguchi 2006; Rezzolla et al. 2010). On the other hand, large mass asymmetries are disfavored on the basis of mass measurements for galactic double pulsars (Ozel & Freire 2016). Moreover, Shibata & Taniguchi (2006) found that the accretion disk mass only increases by about an order of magnitude for extremely asymmetric binaries.

We speculate on the total amount of mass expelled in a binary NS merger. We consider three different ejection channels. In addition to the dynamical ejecta, directly extracted from the simulations, we include the possible presence of neutrino- and magnetically driven winds from the disk, which develop on a timescale of a few tens of ms. We parameterize their contribution to the ejecta as a fraction of the disk mass. The neutrino-driven wind is estimated as $M_{\rm ej;wind} = \xi_{\rm wind} M_{\rm disk}$, with $\xi_{\rm wind} = 0.03 \pm 0.015$. The uncertainty includes variations due to the possible presence of a longer-lived remnant (e.g., Just et al. 2015; Martin et al. 2015). The viscous ejecta is taken to be $M_{\rm ej;\,vis} = \xi_{\rm vis} M_{\rm disk}$ with $\xi_{\rm vis} = 0.2 \pm 0.1$, a range including the results from most postmerger simulations (e.g., Metzger & Fernández 2014; Just et al. 2015; Fernández et al. 2019; Fujibayashi et al. 2018; Siegel & Metzger 2018).

In Figure 16 we compare dynamical and secular ejecta masses, the latter estimated as $M_{\rm ej;sec} = M_{\rm ej;wind} + M_{\rm ej;vis}$. With the exception of the prompt BH formation cases that produce at least $10^{-4}\,M_\odot$ of dynamical ejecta, the total ejecta is largely dominated by the disk ejecta. As a consequence of the tight correlation between the disk mass and $\tilde{\Lambda}$, we expect a correlation between the total ejecta and $\tilde{\Lambda}$. Indeed, our estimates for $M_{\rm ej} + M_{\rm ej;wind} + M_{\rm ej;vis}$ are reasonably well fitted by the same simple formula used for $M_{\rm disk}$, Equation (25), but assuming a floor value of $5 \times 10^{-4}\,M_\odot$ and with fitting coefficients $\alpha = 0.0202$, $\beta = 0.0341$, $\gamma = 538.8$, and $\delta = 439.4$. In most cases, the relative error between the total ejecta mass and the fit is below 50%. When prompt BH formation occurs, we do not expect the total ejecta to be larger than $\sim 10^{-3}\,M_\odot$. On the other hand, for long-lived remnants the mass of the unbound material can span a broad range of masses: from a few times $10^{-3}\,M_\odot$ to $0.1 M_\odot$, increasing with $\tilde{\Lambda}$.

In comparison to previous studies (Oechslin et al. 2007; Hotokezaka et al. 2013b, as reported in Wu et al. 2016) we find that disk winds and viscous outflows should contribute a significantly larger fraction of the overall ejecta. The difference can be explained in part by the fact that previous simulations did not include the effects of neutrino cooling, or used approximate treatments for the gravity, and in part by the fact that we assume that a larger fraction of the accretion disk can be unbound secularly, unlike Wu et al. (2016). The latter assumption is motivated by recent GRMHD simulations that showed that up to $\sim$40% of the disk can be unbound secularly (Siegel & Metzger 2017; Fernández et al. 2019). Our study differs from some of the previous studies also in the numerical setup and analysis methodology.

4. Nucleosynthesis

The discovery of a kilonova counterpart to GW170817 (Abbott et al. 2017e; Arcavi et al. 2017; Chornock et al. 2017; Coulter et al. 2017; Cowperthwaite et al. 2017; Drout et al. 2017; Evans et al. 2017; Kasliwal et al. 2017; Nicholl et al. 2017; Smartt et al. 2017; Soares-Santos et al. 2017; Tanaka et al. 2017; Tanvir et al. 2017) provided compelling evidence that NS mergers are one of the main sources of *r*-process elements in the universe (Kasen et al. 2017; Hotokezaka et al. 2018a; Rosswog et al. 2018). However, the question of whether NS mergers are the only source of *r*-process elements or whether there is a contribution from other sources is still not completely settled. Part of the uncertainty is due to the lack of a full theoretical understanding of the nucleosynthetic yields from mergers. Here, we study in detail the dependence of *r*-process nucleosynthesis on the properties of the binary, mostly focusing on the dynamical ejecta.

4.1. Dynamical Ejecta

For simplicity, we perform most of our nucleosynthesis calculations using the approach we developed in Radice et al. (2016b) and which we briefly recall. We extract electron fraction $Y_{e,R}$, specific entropy s_R, velocity v_R, and rest-mass density $\rho_{0,R}$ of the unbound material crossing a coordinate sphere surface with radius $R = 300\,G/c^2\,M_\odot \simeq 443$ km. A fluid element is considered to be unbound if its kinetic energy is sufficient to overcome the gravitational potential well, that is, $u_t \leqslant -1$, where we have assumed a nearly stationary metric. See Kastaun & Galeazzi (2015) and Bovard et al. (2017) for alternative criteria. For the nucleosynthesis calculations we further assume that the outflow is undergoing a homologous expansion

$$\rho_0(t) = \rho_{0,R}\left(\frac{v_R}{cR}t\right)^{-3}. \tag{26}$$

This density history is matched with the expansion histories used in the parameterized r-process calculations of Lippuner & Roberts (2015):

$$\rho_0(t) = \rho_0(s, Y_e, T = 6\ \mathrm{GK})\left(\frac{3\tau}{et}\right)^3, \tag{27}$$

where $e \simeq 2.718$ is Euler's number. From the matching we extract the expansion timescale τ. To compute the nucleosynthesis yields we bin the ejecta according to their density, entropy, and expansion timescale. The nucleosynthesis yields in each bin can be pre-computed because, under the assumption of homologous expansion, the r-process outcome depends only on $\rho_{0,R}$, s_R $Y_{e,R}$, and τ_R. Then we compute the full nucleosynthetic yields by summing up the contributions from all bins. The uncertainty due to this procedure and the comparison with nucleosynthetic calculations performed using Lagrangian tracer particles are discussed in Section 4.3.

We discuss first the systematics of the nucleosynthetic yields for our fiducial subset of runs, for which neutrino re-absorption has been neglected. The effect of neutrino re-absorption is discussed below. Figure 17 shows histograms of the electron fraction Y_e of the ejecta and the relative abundances of different isotopes synthesized by the r-process 32 years after the merger. We show the electron fraction since it is the most important variable determining the outcome of the r-process in the conditions relevant for NS mergers (e.g., Lippuner & Roberts 2015; Radice et al. 2016b). In the figure we compare isotopic abundances of r-process elements estimated from our simulation with the solar abundances from Arlandini et al. (1999). Both abundances are normalized by fixing the overall fraction of elements with $180 \leqslant A \leqslant 200$.

In the absence of neutrino heating, the distribution of the ejecta as a function of Y_e drops rapidly for $Y_e > 0.15$–0.2. We find systematic changes in the composition of the outflows as the total mass of the binary increases. However, these variations are inconsistent between the different EOSs. The BHB$\Lambda\phi$ and SFHo binaries produce higher Y_e ejecta as the binary mass is increased, presumably because the larger compactness of the more massive binaries inhibits the production of tidally driven ejecta. As a consequence, these binaries produce more of the light r-process elements, i.e., the isotopes with $90 \lesssim A \lesssim 125$, when approaching the prompt BH formation threshold. Conversely, the relative amount of shocked ejecta from the LS220 binaries progressively decreases as the binary mass increases and the ejecta for the most massive binaries appears to be dominated by the tidal tail. Consequently, the relative abundance of light r-process elements decreases with the total binary mass for the LS220 binaries. Finally, the behavior of the DD2 binaries is non-monotonic with mass: for chirp masses up to $\sim 1.25\,M_\odot$ the average electron fraction $\langle Y_e \rangle$ increases with mass. However, the highest-mass binary `DD2_M160160_LK`, has the lowest $\langle Y_e \rangle$ and the lowest relative abundance of light r-process elements.

Overall we find that, irrespective of binary parameters and EOS, the dynamical ejecta robustly produce second- and third-peak elements, i.e., elements with $125 \lesssim A \lesssim 145$ and $185 \lesssim A \lesssim 210$, respectively. The reason for this is that the bulk of the outflows are always very neutron rich, with $\langle Y_e \rangle < 0.2$. On the other hand, we observe a variance in the production of the light r-process elements.

The normalization condition we impose effectively scales the second and third peaks of the solar abundances to the second and third peaks of the calculated abundances (see Figure 17). With this normalization, it is clear that our calculations underproduce the material in the mass $\sim$140 region beyond the second r-process peak. We note that, although different models produce a wide range of Y_e distributions, this underproduction is robust. Therefore, it is more likely due to the choice of nuclear input data used in our network calculations. In particular, the choice of fission fragment distributions and neutron-induced fission rates can have a significant impact on abundances in this region (Eichler et al. 2015), and the symmetric fission fragment distributions used in our calculations likely underproduce material in this region.

Neutrino–matter interaction rates roughly scale with the square of the incoming neutrino energy. Consequently, the composition, nucleosynthetic yield, and EM opacity of the ejecta depend on the details of the neutrino radiation spectra (Foucart et al. 2016b). The determination of the last quantity is not possible using an energy-integrated scheme such as adopted for this work. To quantify the relative uncertainty, we simulate the $(1.35 + 1.35)\,M_\odot$ binary using the LS220 EOS and two different schemes for the calculation of the absorption opacities. In addition to the standard treatment in which we approximatively account for the incoming neutrino energy using Equation (8), we also perform a simulation in which the absorption cross-section is calculated assuming local thermal equilibration (LTE) between matter and neutrinos. This simulation is labeled `LS220_M135135_M0_LTE`.

The results of this comparison are shown in Figure 18. As anticipated, the inclusion of compositional changes and heating due to the absorption of neutrinos results in a significant shift in the ejecta Y_e distribution. The tidal tail is reprocessed to slightly higher values of Y_e and a new ejecta component, with Y_e up to 0.4, is found. The approximate inclusion of non-LTE effects results in a slight increase in the absorption rates. This is expected because the incoming neutrinos originally decoupled from the central regions of the remnant and the accretion disk at higher temperatures than those found in the ejecta. Overall, we find that the dynamical ejecta, especially in the regions close to the orbital plane, robustly produces heavy r-process elements with relative abundances close to solar. On the other hand, the neutrino re-absorption significantly affects the production of elements in the region close to the first peak of the r-process relative abundance pattern, i.e., around $A = 80$. The treatment of the absorption opacities can result in changes in the relative abundance of elements in this region of up to factors of a few. This points to the need for more sophisticated simulations with spectral neutrino transport.

We do not consider the effect of neutrino oscillations in this work. However, we point out that recent studies have shown that NS merger remnants might host ideal conditions for resonant oscillations and fast flavor conversion (Zhu et al. 2016; Frensel et al. 2017; Deaton et al. 2018). This might have an impact on the nucleosynthesis of light r-process elements (Wu et al. 2017). Investigation of these effects in the context of dynamical simulations is urgent.

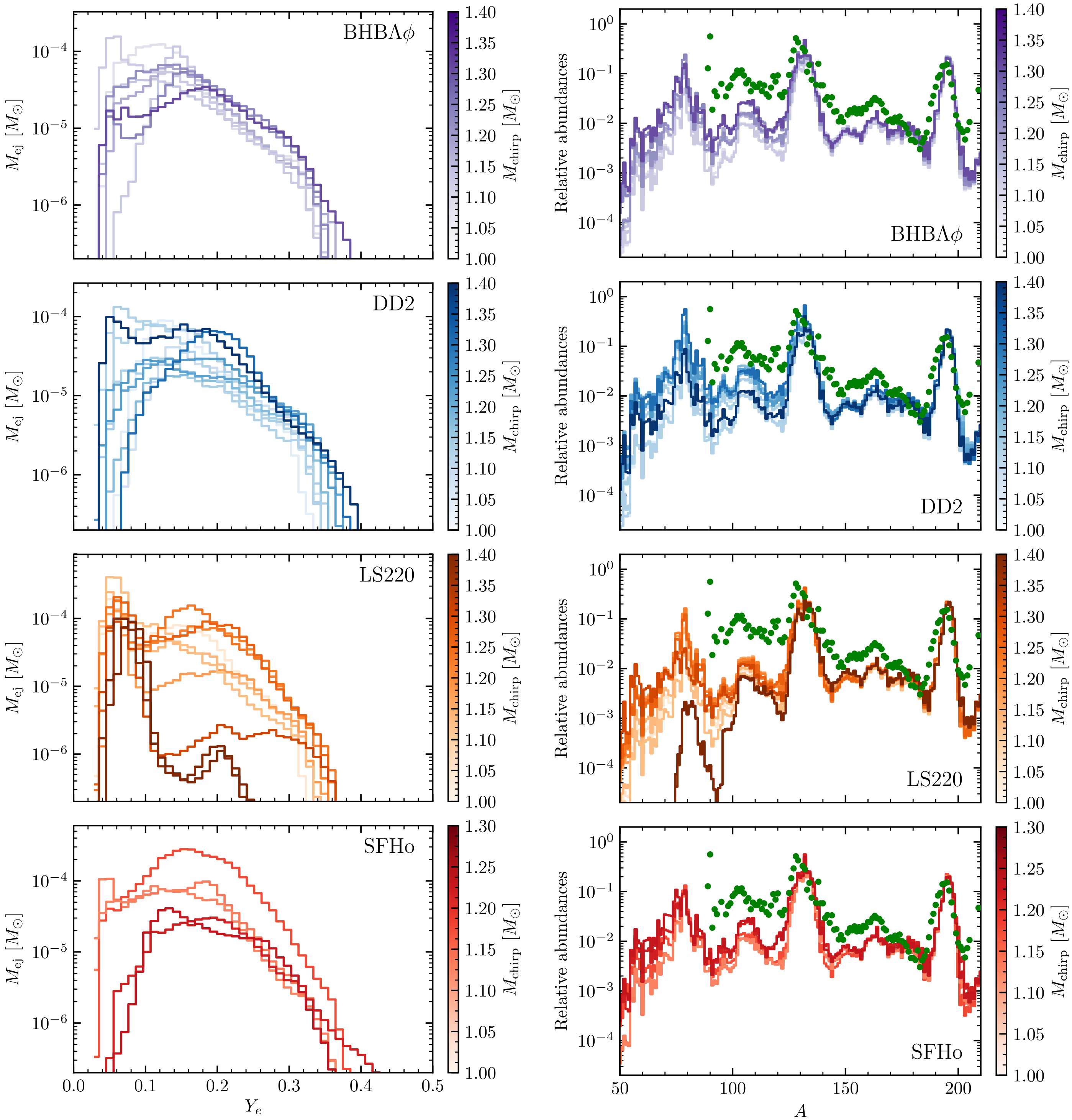

Figure 17. Electron fraction of the ejecta before the activation of the r-process (left panel) and final nucleosynthetic abundances (right panel). The histograms show the results from our fiducial subset of simulations. We only include models with total ejecta mass larger than $5 \times 10^{-5}\,M_\odot$. The green dots in the right panel show the solar abundances from Arlandini et al. (1999). All abundance curves are normalized by fixing the overall fraction of elements with $180 \leqslant A \leqslant 200$.

The nucleosynthetic yield of the dynamical ejecta is also sensitive to the mass ratio of the binary, especially in the region of light r-process elements. This is shown in Figure 19 where we compare composition and nucleosynthesis yields between the `LS220_M135135_M0` and `LS220_M140120_M0` binaries which are representative of the general trend with mass ratio. The relative abundances are normalized as in Figure 17 over the mass range $180 \leqslant A \leqslant 200$. Because of the more abundant tidal tail the relative composition of the ejecta is shifted to lower Y_e. This affects the relative abundances of first-peak r-process elements which are reduced by factors of several. A similar trend is also present in the simulations that do not include neutrino re-absorption; see Table 2.

Even though there are differences in the quality and quantity of the dynamical ejecta, r-process nucleosynthesis appears to be only weakly sensitive to the EOS. In Figure 20 we show

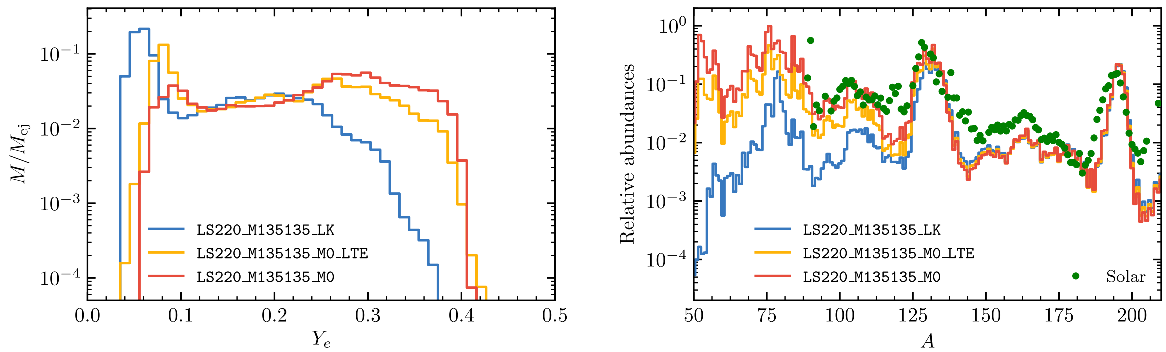

Figure 18. Dynamical ejecta sensitivity to neutrino treatment. Left panel: electron fraction; right panel: nucleosynthetic yields. All abundance curves are normalized by fixing the overall fraction of elements with $180 \leqslant A \leqslant 200$. Neutrino absorption can have a strong impact on the ejecta composition and on the nucleosynthetic yields around the light *r*-process elements.

electron fraction distributions and final isotopic abundances for the dynamical ejecta from the $(1.35 + 1.35)\,M_\odot$ binary simulated with different EOSs. Neutrino re-absorption has been included in these simulations using the M0 scheme. Irrespective of the EOS, the dynamical ejecta is neutron rich $\langle Y_e \rangle \lesssim 0.25$, but has a broad distribution in Y_e, with a significant amount of ejecta with Y_e as large as 0.4. Consequently, both heavy and light *r*-process elements are produced. For comparable mass binaries, such as those shown in Figure 20, we find that the dynamical ejecta robustly synthesizes *r*-process elements with isotopic abundances close to solar. Conversely, the dynamical ejecta from binaries with large mass asymmetry underproduces light *r*-process elements. These conclusions are not altered with the inclusion of viscosity. Indeed, while viscosity impacts the overall ejecta mass (Table 2 and Radice et al. 2018b), it does not affect the electron fraction and the isotopic abundances of the *r*-process in the dynamical ejecta. Overall, our simulations suggest that the EOS of dense matter controls the amount of the dynamical ejecta, but that the relative isotopic abundances are most sensitive to weak reaction rates, mass ratio, and total binary mass.

4.2. Secular Ejecta

The nucleosynthetic yields of the secular ejecta have been the subject of several recent studies. In the case of neutrino-driven winds, neutrino irradiation of the expanding ejecta drives the electron fraction toward higher values than those of the original cold, weak equilibrium configuration. The electron fraction of the material in the wind depends on the relative timescales for weak re-equilibration and expansion. If the expansion is not too rapid, then the material achieves electron fractions given by the weak equilibrium in optically thin conditions with neutrinos (Qian & Woosley 1996):

$$(Y_e)_{\rm eq} = \left[1 + \frac{L_{\bar{\nu}_e}(\epsilon_{\bar{\nu}_e} - 2\Delta + 1.2\Delta^2/\epsilon_{\bar{\nu}_e})}{L_{\nu_e}(\epsilon_{\nu_e} + 2\Delta + 1.2\Delta^2/\epsilon_{\nu_e})}\right]^{-1}, \qquad (28)$$

where L_{ν_e} and $L_{\bar{\nu}_e}$ are the luminosities for electron neutrinos and antineutrinos, $\epsilon_\nu \equiv \langle E_\nu^2 \rangle / \langle E_\nu \rangle$, E_ν is the neutrino energy, $\langle x \rangle$ is the average of x over the neutrino distribution function, and Δ is the mass difference between neutrons and protons in vacuum. During the early postmerger phase, $L_{\bar{\nu}_e} \gtrsim L_{\nu_e}$, while electron antineutrinos are significantly hotter than neutrinos ($\langle E_{\bar{\nu}_e} \rangle \approx 15$ MeV $> \langle E_{\nu_e} \rangle \approx 10$ MeV; e.g., Dessart et al. 2009; Perego et al. 2014; Foucart et al. 2016b). Thus, $(Y_e)_{\rm eq} \lesssim 0.45$ and *r*-process nucleosynthesis can occur. However, due to the small neutron-to-seed ratio, only nuclei with $A \lesssim 130$ can be synthetized and this ejecta is expected to contribute to the first *r*-process peak. If the dynamical ejecta is dominated by the tidal component and has few first peak *r*-process elements, the neutrino-driven wind can complement the nucleosynthesis and lead to the production of all *r*-process elements (Martin et al. 2015).

If a massive disk forms after the merger, viscously driven ejection, occurring over the disk lifetime, can become the dominant source of ejecta from a binary NS merger (see Section 3.2). Viscous hydrodynamic simulations of the long-term disk evolution, mainly performed in axisymmetry assuming a BH–torus system, showed that, if the disk becomes transparent to neutrinos, the rapid decrease in temperature makes neutrino cooling inefficient and the disk becomes connectively unstable (e.g., Fernández & Metzger 2013; Just et al. 2015). The resulting large-scale mixing, combined with the long timescale over which neutrino–matter interactions can occur, produces a rather uniform, broad distribution of Y_e in the ejecta. In particular, it was found that the resulting distribution has $0.1 \lesssim Y_e \lesssim 0.45$ and all *r*-process elements from the first to the third peak, as well as uranium and thorium, can be synthesized in proportions close to solar (e.g., Wu et al. 2016).

Recent 3D GRMHD simulations of a BH disk torus (Siegel & Metzger 2017; Fernández et al. 2019) confirmed the presence of a self-regulating mechanism based on electron degeneracy in the disk mid-plane that ensures the presence of a reservoir of neutron-rich material ($Y_e \sim 0.1$). This results in the production of neutron-rich outflows ($\langle Y_e \rangle \sim 0.2$). The resulting nucleosynthesis yields all *r*-process elements between the second and the third peak. If the kinetic energy dissipation in the innermost part of the disk results in a significant neutrino luminosity, neutrino absorption increases the electron fraction of the ejecta, producing also elements down to the first peak. Neutrino influence on the properties of the viscous ejecta can be even more relevant in the presence of a long-lived massive NS. This is expected to emit a large amount of neutrinos over the diffusion timescale (a few seconds; e.g., Dessart et al. 2009; Perego et al. 2017b). The high neutrino flux is expected to unbind matter in a neutrino-driven wind during the first tens of ms after the merger (Dessart et al. 2009; Perego et al. 2014; Fujibayashi et al. 2017) and can further increase the electron fraction of the viscous ejecta. For a very long-lived massive NS, the properties of the neutrino- and viscously driven ejecta

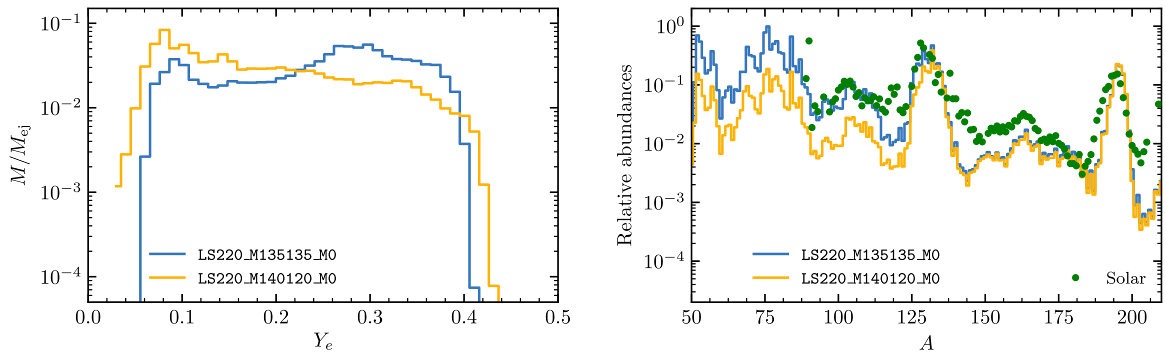

Figure 19. Dynamical ejecta sensitivity to the binary mass ratio. Left panel: electron fraction; right panel: nucleosynthetic yields. All abundance curves are normalized by fixing the overall fraction of elements with $180 \leqslant A \leqslant 200$. The nucleosynthetic yield from the dynamical ejecta is sensitive to the mass ratio in the region of the light *r*-process elements $A \lesssim 120$.

could become similar and the resulting *r*-process nucleosynthesis in the viscous ejecta could be limited to the first and second *r*-process peaks (Lippuner et al. 2017).

4.3. Effect of the Thermodynamic History of the Ejecta

In principle, nucleosynthesis in the ejecta should be calculated by following the non-equilibrium evolution of the material composition as it is advected along with the fluid flow and potentially undergoes mixing. Such an approach would require tracking the large number of isotopic abundances needed to follow the *r*-process flow along with adding stiff, coupled source terms to the composition equations. Such an approach is too computationally expensive, but it would include possible feedback on the ejecta dynamics of nuclear heating and composition-based changes to the EOS (Metzger et al. 2010). The next level of approximation to the nucleosynthesis in the outflows would be following nucleosynthesis in Lagrangian tracers of the flow, while ignoring the back-reaction of nucleosynthesis on the flow dynamics. This is likely to be a very reasonable approximation, since the nuclear energy release is only likely to be important to the dynamics of a small amount of marginally bound material. Nevertheless, nuclear burning will produce entropy in these fluid elements which may change the nuclear flow. Therefore, most calculations of nucleosynthesis in binary NS merger ejecta involve taking density histories, $\rho(t)$, of Lagrangian tracers and evolving the composition and entropy of the material in time starting at t_0, with entropy s_0 and electron fraction $Y_{e,0}$ extracted from the simulation output using a self-heating nuclear reaction network (Freiburghaus et al. 1999).

For the nucleosynthesis results discussed above in this section, an even more approximate method has been used in which we assume $\rho(t) \approx \rho_0(t;\, \tau_d,\, s_R,\, Y_{e,R})$, where $Y_{e,R}$ and s_R are the electron fraction and entropy at of an ejected fluid element when it crosses a radius R and $\tau_d = eR/(3v_R)(\rho_R/\rho_0)^{1/3}$ as described above. This approximation allows us to rapidly calculate nucleosynthesis without including Lagrangian tracer particles in the simulations, but it needs to be tested. Therefore, we have run one simulation with a large number of tracer particles and calculated nucleosynthesis in these tracers using their actual density histories. The results of this calculation compared to our approximate method of calculating nucleosynthesis are shown in Figure 21. At all mass numbers, the calculations agree to within a factor of two and in most regions to better than 20%. This agreement is good enough to give us confidence in our approximation. Nevertheless, we would like to understand where the variations come from.

The first possible source of error in our approximation is that going from $\rho(t) \to \rho_0(t;\, \tau_d,\, s_R,\, Y_{e,R})$ introduces errors into the calculation. We test this for individual tracer particles by running nucleosynthesis calculations using both the actual density history $\rho(t)$ and $\rho_0(t)$. The nucleosynthesis results for these particles are shown in Figure 22. Our approximate functional form for the density captures most of the behavior of the actual particles and we recover very similar nucleosynthesis in both cases. All abundances above 10^{-5} agree within a factor of two between the two calculations for all Y_e.

The second possible source of error comes from sampling error in the Lagrangian tracer particles. To test how well they represent the underlying Eulerian flow, we compare the distribution of $Y_{e,R}$ and s_R inferred from integrating the flux using the Eulerian outflow and sampling the conditions in the Lagrangian particles at R. These are shown in Figure 23. The Y_e and entropy of the particle may change between $R = 300\, G/c^2\, M_\odot$ and the time nucleosynthesis begins at $\sim$6 GK. The average electron fraction for the Eulerian outflow is $\langle Y_e \rangle = 0.22$, while it is $\langle Y_e \rangle = 0.20$ at both measurement points in the tracer particles. By comparing the tracer Y_e distributions at these two points, we can see that this approximation introduces at most a 25% error in the Y_e distribution (at $Y_e = 0.04$) and substantially less error at most Y_e. The difference between either tracer Y_e distribution and the integrated Eulerian outflow Y_e distribution is substantially larger, almost 40% at $Y_e = 0.25$. We have checked that this error is not due to undersampling by the Lagrangian tracer particles.

5. Electromagnetic Signatures

The radioactive decay of freshly synthesized *r*-process nuclei in the expanding ejecta powers a quasi-thermal emission known as a kilonova (Li & Paczynski 1998; Kulkarni 2005; Metzger et al. 2010). The properties of the emission crucially depend on the amount of mass, on the expansion velocity, and on the detailed composition of the ejecta. The last, in particular, determines the photon opacity, which can substantially differ from the opacity of iron group elements in the presence of a significant fraction of lanthanides (e.g., Kasen et al. 2013; Tanaka & Hotokezaka 2013).

Eleven hours after the detection of GW170817, a kilonova transient consistent with a binary NS merger was detected and intensively followed up for a few weeks (AT2017gfo;

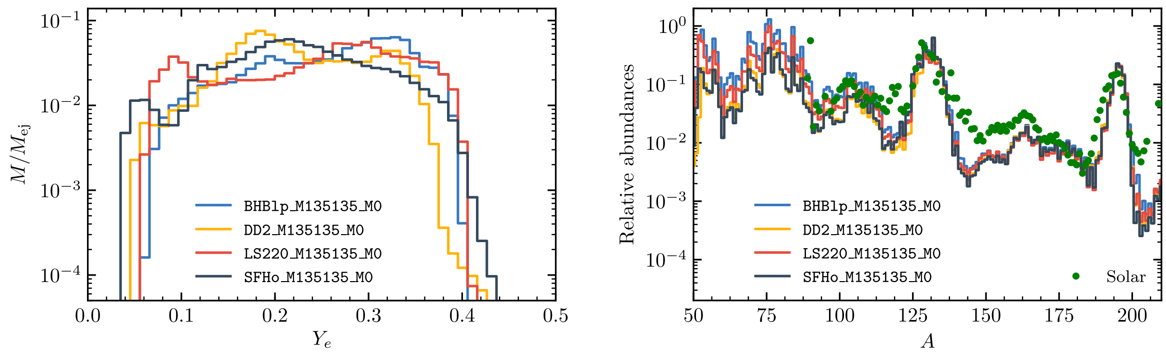

Figure 20. Dynamical ejecta sensitivity to the EOS. Left panel: electron fraction; right panel: nucleosynthetic yields. All abundance curves are normalized by fixing the overall fraction of elements with $180 \leqslant A \leqslant 200$. The total ejecta mass depends sensitively on the EOS; however, electron fraction and nucleosynthetic yields appear to be insensitive to the EOS.

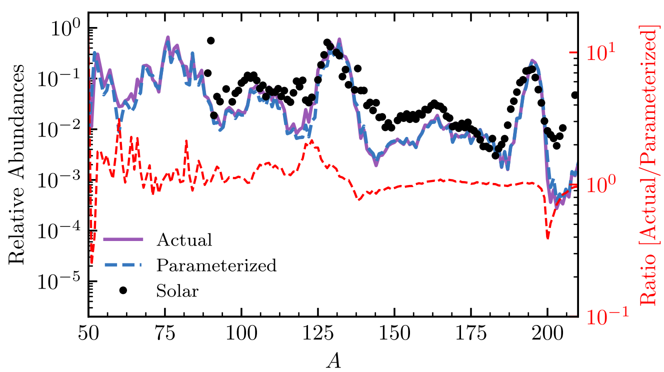

Figure 21. Integrated nucleosynthesis from a simulation using the actual density history from the simulation extracted from tracer particles (dashed line) and using the integrated mass flux approximation described in the text (solid line). The thin dashed line shows the ratio of the two calculations.

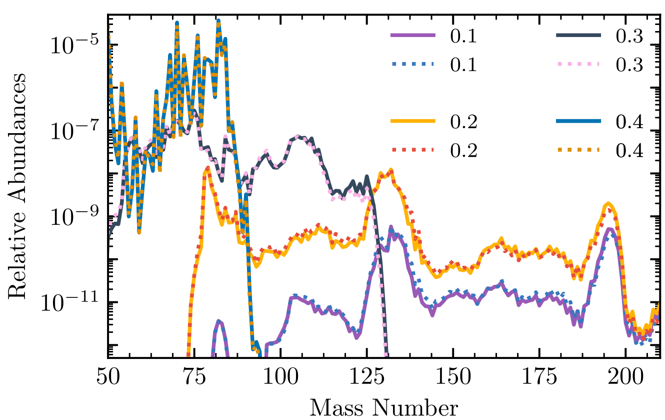

Figure 22. Nucleosynthesis for four selected tracer particles calculated using the actual density history from the simulation (solid lines) and using a parameterized density history extracted as described in the text (dashed lines). The legend labels the Y_e of each separate trajectory. We see that there is generally good agreement between the nucleosynthesis predictions with the different density histories across a broad range of Y_e. The abundance curves are scaled by arbitrary factors for clarity.

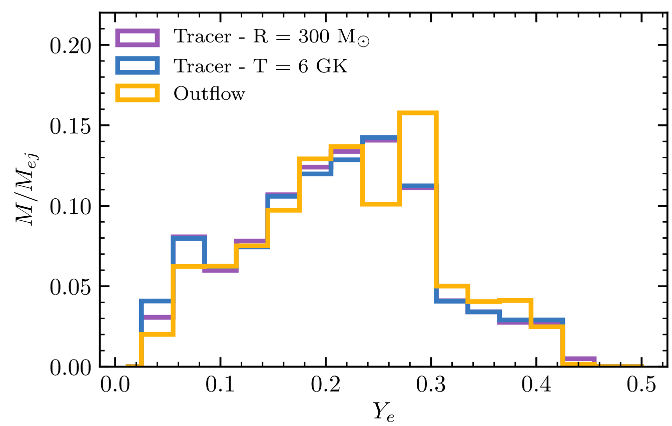

Figure 23. Distribution of the electron fraction in the ejecta as inferred from the tracer particles when they reach a radius of $300\,G/c^2\,M_\odot$, when they reach a temperature of 6 GK, and from the integrated mass outflow at $300\,G/c^2\,M_\odot$ calculated on the Eulerian grid as described above.

Abbott et al. 2017e; Arcavi et al. 2017; Coulter et al. 2017; Drout et al. 2017; Evans et al. 2017; Kasliwal et al. 2017; Nicholl et al. 2017; Smartt et al. 2017; Soares-Santos et al. 2017; Tanvir et al. 2017). The emission peaked in the UV and visible bands within the first day. Subsequently, the kilonova reddened and peaked in the near-IR (NIR) on a timescale of a few days.

A long-lasting synchrotron remnant is suggested as another promising electromagnetic counterpart to NS mergers (Nakar & Piran 2011; Hotokezaka et al. 2016). Previous studies showed that such signals can be produced by several different ejecta components, e.g., an SGRB jet, cocoon, and dynamical ejecta (van Eerten & MacFadyen 2011; Piran et al. 2013; Hotokezaka & Piran 2015). A synchrotron remnant has been detected in X-ray, optical, and radio bands for GW170817 (Haggard et al. 2017; Hallinan et al. 2017; Margutti et al. 2017, 2018; Mooley et al. 2018a; Troja et al. 2017; Alexander et al. 2018; Dobie et al. 2018; Lyman et al. 2018; Ruan et al. 2018). Recently, Mooley et al. (2018b) and Ghirlanda et al. (2018) observed the superluminal motion of a compact radio emission region in GW170817 and provided us with direct evidence of the existence of a narrowly collimated off-axis jet.

5.1. Kilonovae

We compute synthetic kilonova light curves for the non-viscous, standard resolution models presented in Table 2 for which disk masses are available. We use the semi-analytical kilonova model presented in Perego et al. (2017a). The model accounts for different ejecta components and their possible anisotropies. It assumes azimuthal symmetry around the rotational axis of the binary and reflection symmetry with respect to the orbital plane. The polar angle θ is discretized in 30 angular bins equally spaced in $\cos\theta$. Within each polar ray, the luminosity, radius, and temperature at the outer photosphere

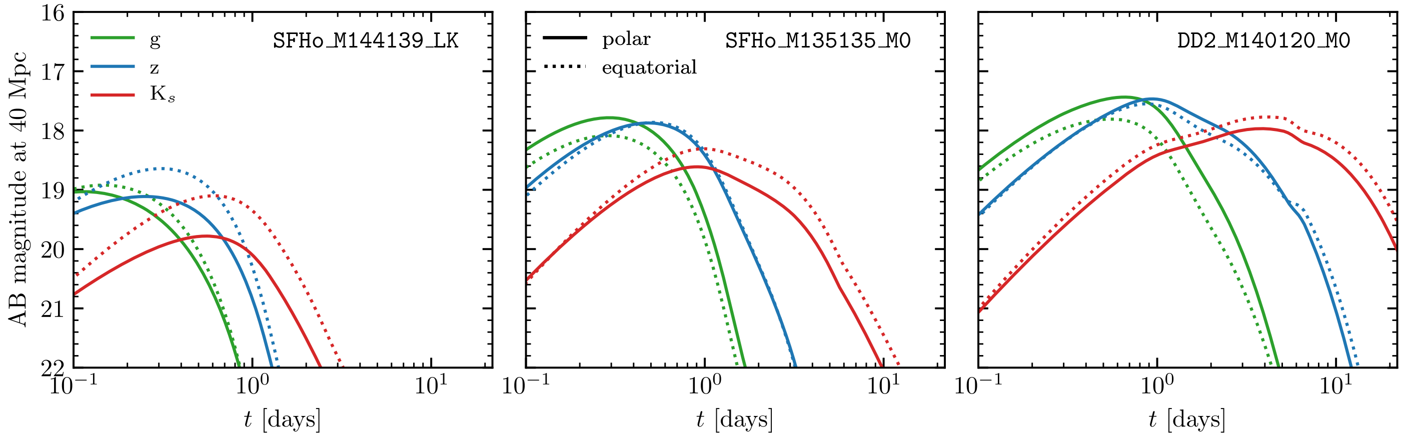

Figure 24. Kilonova synthetic light curves in three different bands (g, z, and K_s) for three representative models. The left panel shows a binary with prompt BH formation. The middle panel shows a binary forming a hypermassive NS ($t_{\rm BH} = 7.7$ ms). The right panel shows a binary forming a long-lived supramassive NS ($t_{\rm BH} > 34.2$ ms). Solid and dashed lines correspond to polar and equatorial viewing angles, respectively. Prompt BH formation binaries do not form massive accretion disks and result in faint and fast transients. Longer-lived NS remnants are associated with the formation of more massive disks that are a source of more abundant secular outflows. They result in brighter kilonovae that evolve on longer timescales.

are related through the Stefan–Boltzmann law. Finally, we compute *AB* magnitudes in different UV/visible/IR bands assuming the distance of the source to be 40 Mpc.

Following Villar et al. (2017), we include a floor temperature $T_{\rm c}$ for the photosphere. We assume all material with temperature less than $T_{\rm c}$ to be transparent so that the effective photosphere temperature is always larger than or equal to $T_{\rm c}$ (see, e.g., Barnes & Kasen 2013). Guided by the values of $T_{\rm c}$ obtained by Villar et al. (2017) for AT2017gfo for different ejecta components, we assume a composition-dependent $T_{\rm c}$. For material having $Y_e > 0.25$ we set $T_{\rm c} = T_{\rm c,blue} = 3000$ K, otherwise we set $T_{\rm c} = T_{\rm c,red} = 1000$ K.

Angular profile, expansion velocity, and electron fraction of the dynamical ejecta are directly extracted from the simulations. Where Y_e is larger than 0.25, the kilonova model assumes a lanthanide-free gray photon opacity $\kappa = \kappa_{\rm blue} = 1.0\ {\rm cm^2\ g^{-1}}$. Otherwise we set $\kappa = \kappa_{\rm red} = 30\ {\rm cm^2\ g^{-1}}$.

For the secular ejecta we include both neutrino-driven and viscously driven winds. The masses of these two components are assumed to be fixed fractions of the remnant accretion disk, as outlined in Section 3.2.

The neutrino-driven wind part of the secular ejecta is assumed to be uniformly distributed from the pole ($\theta = 0$) to $\theta = 60°$. This ejecta component is assumed to expand radially with $v_{\rm rms} = 0.08c$. We assume low opacity $\kappa = \kappa_{\rm blue}$ for the part of the neutrino-driven wind at $\theta \leqslant 45°$, which is found to be less neutron rich in postmerger simulations (e.g., Perego et al. 2014; Martin et al. 2015), while we set the opacity of the rest of the neutrino-driven wind to be $\kappa = \kappa_{\rm purple} = 5.0\ {\rm cm^2\ g^{-1}}$, since this part of the wind is expected to have a broader distribution of Y_e.

The viscously driven wind is assumed to have a $\sin^2\theta$ distribution in mass as a function of the polar angle and to expand homologously with $v_{\rm rms} = 0.06c$. Due to the expected broad and homogeneous Y_e distribution of this outflow component (e.g., Metzger & Fernández 2014; Fujibayashi et al. 2018), we assume $\kappa = \kappa_{\rm purple}$ at all angles.

The model parameters discussed above, as well as other parameters not explicitly mentioned, have been calibrated using AT2017gfo in Perego et al. (2017a). We refer to that study for a more detailed account of the procedure used to generate synthetic kilonova light curves.

In Figure 24 we present synthetic light curves for three representative binaries in three different bands. The left panel shows a prompt BH formation case, `SFHo_M144139_LK`, the middle panel shows a short-lived HMNS case, `SFHo_M135135_M0`, and the right panel shows a case where a BH has not formed by the end of the simulation, `DD2_M140120_M0`. In the last case we assume that the massive NS will not collapse within the accretion disk lifetime. In a previous work, we have already speculated on the possible implications of a long-lived or even stable massive NS on the kilonova light curves (Radice et al. 2018a). We compute light curves in a band in the visible part of the EM spectrum (g) and in two NIR bands (z and K_s). These are chosen because their effective wavelength midpoints satisfy the proportion 1:2:4, and because they span a significant fraction of the expected detection range.

The `SFHo_M144139_LK` binary undergoes prompt collapse and forms a BH surrounded by a light accretion disk with $M_{\rm disk} = 9 \times 10^{-4}\ M_\odot$. In this case the ejecta is predominantly of dynamical origin ($M_{\rm ej} = 4 \times 10^{-4}\ M_\odot$). The outflow is neutron rich ($\langle Y_e \rangle = 0.18$) and expands rapidly ($v_{\rm ej} = 0.33c$). Despite the large effective photon opacity of the ejecta, because of the small mass and fast expansion of the outflows, this binary produces a rapid but faint transient peaking within the first day of the merger in all bands. Polar observers preferentially receive radiation from lower-opacity but also lower-density material. For these observers the kilonova fades even more rapidly and is bluer.

The `SFHo_M135135_M0` binary produces a short-lived HMNS. After its collapse a BH–torus system with a disk of $0.0123\ M_\odot$ is formed. We estimate that this binary will eject $\lesssim 3 \times 10^{-3}\ M_\odot$ of material in the form of secular ejecta, an amount comparable to that of the dynamical ejecta, $\sim 4.2 \times 10^{-3} M_\odot$. The resulting kilonova transient peaks within a day in both g and z bands and subsequently reddens. Because of the higher Y_e of the dynamical ejecta in the polar region, and because of the presence of the neutrino-driven wind from the disk, polar observers will see a marginally brighter kilonova in the UV/visible bands compared to equatorial observers. Conversely, due to the larger amount of dynamical and viscous ejecta close to the orbital plane, equatorial observers will receive a larger NIR flux.

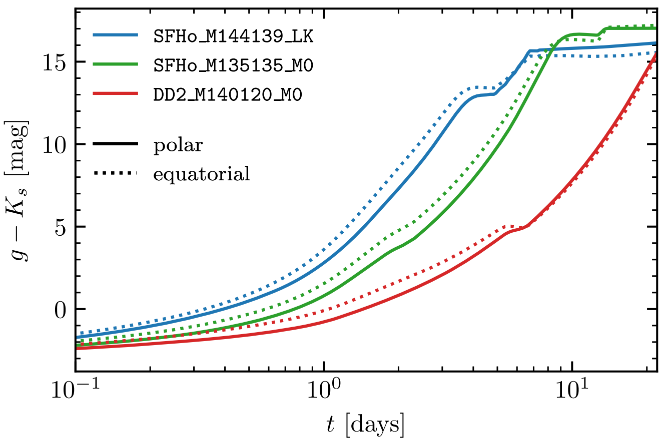

Figure 25. Color evolution of the kilonova light curves computed as the difference in the *AB* magnitude between g and K_s bands for three representative models. Binaries forming hypermassive NSs or dynamically stable remnants power significantly bluer transients.

The results are qualitatively different for the third binary, DD2_M140120_M0, which forms a long-lived remnant. While the mass and the characteristics of the dynamical ejecta from this binary are in line with that of the SFHo_M135135_M0 binary, the former produces a much more massive disk ($M_{\rm disk} \approx 0.19\, M_\odot$). Consequently, the secular ejecta dominates over the dynamical ejecta in this case and the outflow is overall more massive and has a lower expansion velocity. The ejecta are optically thick for days and this results in more slowly evolving light curves in all bands. The light curves in both the z and the K_s bands present a double-peak structure with a first peak around 1 day and a second one at around 5–7 days depending on the inclination. The z band shows a kink instead of a second peak, and both peak and kink are shifted to earlier times compared to the redder filters of the two peaks. These features are the result of the presence of different ejecta components: the dynamical and neutrino-driven wind ejecta, which mostly determine the early light curve, and the viscously driven wind, which dominates at late times.

The color evolutions for these models, exemplified by the difference in magnitude between the g and K_s bands, are shown in Figure 25. All of the synthetic kilonova signals show a fast evolution toward the IR after about a day from the merger. However, there are are significant differences between them. This suggests that the color of the kilonova signal could be used to infer the outcome of the merger. We remark that a similar point was also made by Metzger & Fernández (2014) and Lippuner et al. (2017). However, in our case the difference in the color is purely due to the differences in dynamical ejecta and disk masses, since we do not assume that long-lived remnants produce disk winds with different compositions, as argued by those authors.

We study the relative impact that each of the ejecta components has on the kilonova light curve in the case of the DD2_M140120_M0 binary. In addition to the "full" light curve, which includes all ejecta components, we generate light curves in which, in turn, one of the ejecta components has been removed. In doing so we assume the viewing angle to be 45°. The results are shown in Figure 26. We recall that our model does not simply add contributions from the different components, but also accounts for irradiation and reprocessing effects. Starting from a few days from the merger the light curves are dominated by the viscous ejecta, especially in the NIR bands. This is not surprising, since this component dominates the overall mass ejection. However, we find that both the neutrino-driven wind and the dynamical ejecta play an important role in determining the visible and NIR light curves in the first days. The dynamical ejecta is most important in the very first day, when the viscous ejecta is still too opaque to contribute significantly. All ejecta components are necessary to reproduce the light curve properties in the UV and visible bands.

The presence of a polar component of the dynamical ejecta irradiated by neutrinos could, in principle, impact the properties of the kilonova emission. We study this in Figure 27 where we compare light curves obtained from two binaries having the same NS masses and EOSs, but different neutrino treatments: BHBlp_M135135_LK and BHBlp_M135135_M0. The angular distribution and composition of dynamical ejecta of these binaries are shown in Figure 4. The inclusion of neutrino re-absorption results in an increase of the magnitude in the UV and visible bands within the first few hours of the merger. However, these differences amount only to less than 0.5 mag, even for an observer located along the polar direction. The reason is that the overall UV/optical signal is actually dominated by the secular neutrino-driven wind, while the dynamical ejecta is less important.

In general, we find that the high-latitude, neutrino-irradiated part of the dynamical ejecta has a very modest impact on the kilonova light curve. Instead the UV/optical signal is typically dominated by the secular neutrino-driven winds. There are two reasons for this. First, the secular neutrino-driven wind dominates the overall outflow of high-Y_e material at high latitudes. Indeed, only a small fraction of the dynamical ejecta is directed far from the orbital plane and experiences significant neutrino irradiation. Second, because of its fast expansion, the lanthanide-free part of the dynamical ejecta becomes transparent already a few hours after merger and does not subsequently contribute significantly to the kilonova light curve. The situation is slightly different for prompt collapse binaries for which the accretion disk masses are modest. However, in these cases the effect of neutrino irradiation of the dynamical ejecta is expected to be negligible.

A summary of the most important features of the kilonova light curves in different bands is presented in Figure 28. For each binary in our fiducial subset of simulations we present the time, the magnitude, and the width of the kilonova peak as a function of $\tilde{\Lambda}$ in three different bands: g, z, and K_s. The peak width is defined as the time interval around the peak over which $\Delta M = +1$. We further distinguish between polar and equatorial observers. Different symbols denote different merger outcomes. There is a clear dependence of the kilonova properties on the nature of the merger remnant and on $\tilde{\Lambda}$. These trends, already anticipated by the three representative cases of Figure 24, are a consequence of the dependence of the disk mass on $\tilde{\Lambda}$ (see Figure 15) and of the dominant role of the secular ejecta in determining the properties of the kilonova. Faint and rapidly decreasing kilonovae indicate the formation of BHs via prompt collapse, while bright and long-lasting light curves in the NIR bands are signatures of longer-lived remnants.

Figure 28 also reports the values or upper limits inferred for AT2017gfo. The properties of the kilonova are compatible with the formation of a massive NS that survived for at least several milliseconds after merger, as also argued by Shibata et al. (2017a). However, it is important to emphasize that our

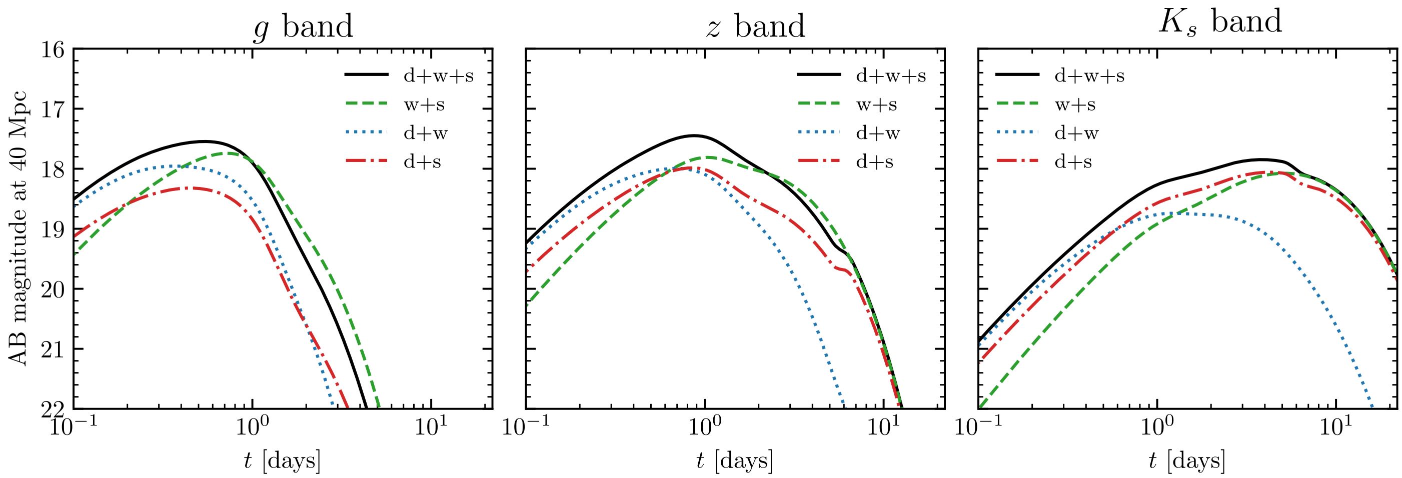

Figure 26. Synthetic kilonova light curves for an observer located at 45° in the g (left), z (middle), and K_s (right) bands for the `DD2_M140120_M0` binary computed using different combinations of ejecta components: dynamical, "d," neutrino-driven wind, "w," and viscously driven wind, "s." The comparison between the light curve obtained including all ejecta components (d+w+s) and light curves obtained by neglecting in turn one of the components reveals the different roles of the components in shaping the light curves, at different times and in different bands.

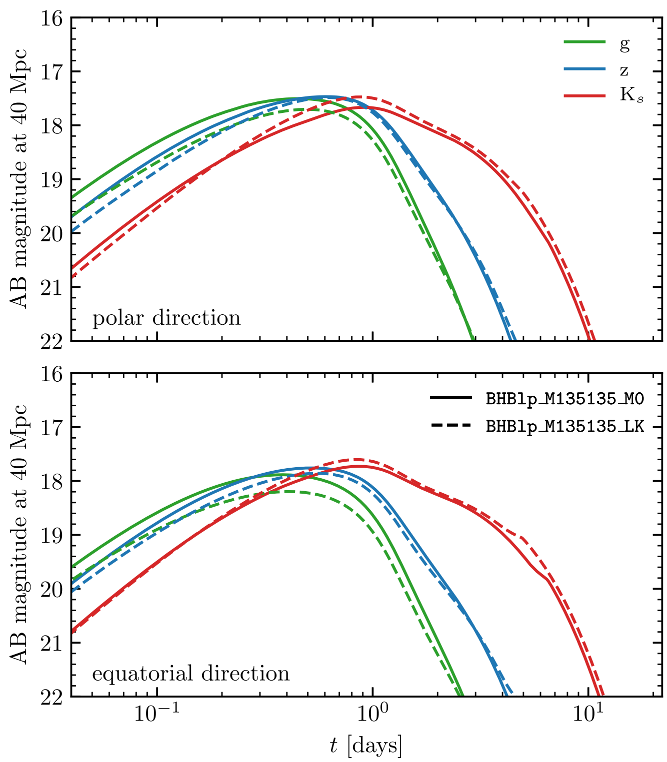

Figure 27. Synthetic kilonova light curves in the g, z, and K_s bands for the `BHBlp_M135135_M0` and `BHBlp_M135135_LK` binaries, both in the polar (top panel) and in the equatorial (bottom panel) directions. Because neutrino-driven winds from the disk dominate the early light curve, the presence of a neutrino-irradiated component of the dynamical ejecta only yields a modest $\lesssim$0.5 mag change of the color light curve in the first few hours after the merger.

theoretical models are based on a number of assumptions that still need to be verified with first-principles simulations, most notably the assumption that a fixed fraction of the accretion disk is unbound by winds.

The differences in the kilonova brightnesses have important consequences for their detectability. We consider the limiting magnitudes reported in Rosswog et al. (2017) for the Large Synoptic Survey Telescope in the g and z bands, and for the Visual and Infrared Survey Telescope for Astronomy in the K_s band and assume exposure times of 60 s. Considering the detection horizon for Advanced LIGO to be 120–170 Mpc (Abbott et al. 2018c), we estimate that kilonovae counterparts would be detectable for a large fraction of the NS merger GW events. If a long-lived massive NS is formed, then the kilonova would be dectable for all GW events in both the g and z bands up to the horizon distance of Advanced LIGO, and up to a luminosity distance of ~90 Mpc in the K_s band. If, on the other hand, a BH is rapidly formed after merger, then the kilonova would only be detectable in the K_s band to distances of 30–50 Mpc, depending on the orientation of the binary. Kilonovae associated with prompt BH formation are detectable in the z and g bands in the entire Advanced LIGO and Virgo volume; however, their observation will be challenging given their fast decline.

In Figure 29 we show the difference in magnitude between the g and K_s bands for kilonovae at three different epochs and as a function of $\tilde{\Lambda}$. Our results show that the color evolution and properties previously described for the three representative models are generic. Moreover, there is a clear correlation between $g - K_s$ and $\tilde{\Lambda}$ which suggests that it might be possible to constrain the EOS of NS matter with EM observations in different bands.

We want to stress that, while the correlations between kilonova light curve properties and $\tilde{\Lambda}$ in Figures 28 and 29 appear robust, their quantitative determination must wait until simulations self-consistently including dynamical and secular ejecta from NS mergers become available. The impact of viscosity on the kilonova light curves is discussed in a companion paper (Radice et al. 2018b).

5.2. Synchrotron Remnants

We calculate the light curve of the synchrotron radiation arising from the dynamical ejecta using the semi-analytic method of Hotokezaka & Piran (2015). According to this model electrons accelerated in the shock between the ejecta and the ISM emit synchrotron radiation in the amplified magnetic field. The total flux density is calculated by integrating the radiation flux from each solid angle over the equal-arrival time surface. The ISM number density n is a parameter of the model. The conversion efficiencies of the internal energy of the shock

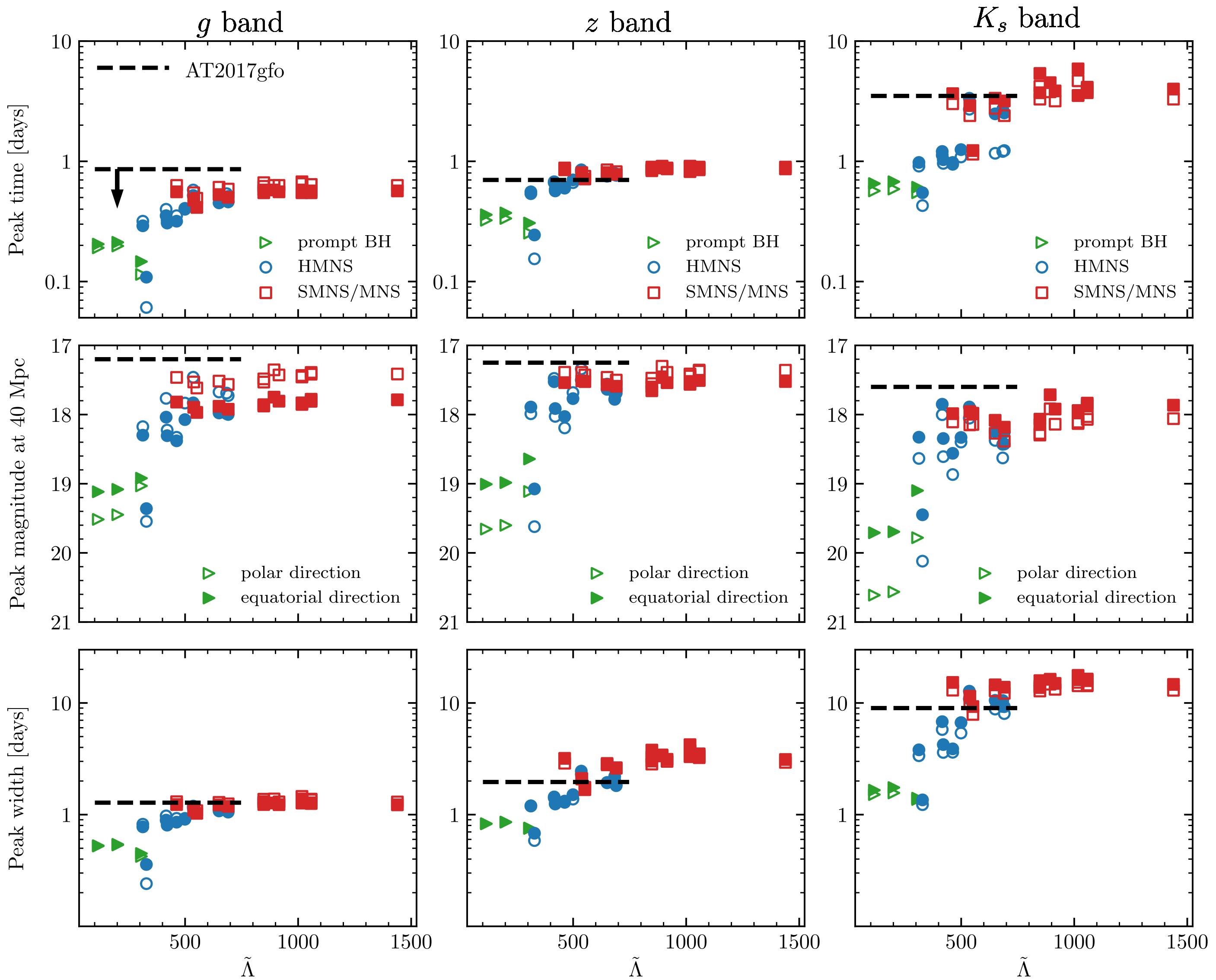

Figure 28. Peak times (top), *AB* magnitudes (middle), and widths (bottom) in three phomometric bands (g, z, and K_s, moving from left to right) of the kilonova synthetic light curves for our fiducial subset of simulations assuming a distance of 40 Mpc for the sources. The peak width is defined as the time interval over which the *AB* magnitude increases by one across the peak. The dashed black lines correspond to the values (or limits) obtained for AT2017gfo, the EM counterpart to GW170817. The horizontal extension of the lines corresponds to the 90% highest posterior density interval 300^{+420}_{-230} for $\tilde{\Lambda}$ obtained assuming low-spin priors by Abbott et al. (2018b). The peak times, magnitudes, and widths of AT2017gfo are obtained from Villar et al. (2017), Coulter et al. (2017), Smartt et al. (2017), and Tanvir et al. (2017). BH formation (small $\tilde{\Lambda}$) results in faint and rapid transients. Longer-lived remnants (large $\tilde{\Lambda}$) are associated with brighter luminosity in the UV/visible bands and longer-lasting, more slowly evolving NIR signals.

to the energy of the accelerated electrons and amplified magnetic field are assumed to be ϵ_e and ϵ_B, respectively. The initial velocity profile of the ejecta is given by mapping the 3D structure of the ejecta to a 1D structure; then the ejecta are evolved adiabatically.

Before discussing the numerical results, here we give briefly the scalings of the peak time and peak flux with the relevant physical quantities. The peak time of the light curve can be estimated from the deceleration time of the ejecta (Nakar & Piran 2011):

$$t_{\rm dec} \sim 3 \cdot 10^3 \ {\rm day}\left(\frac{T_{\rm ej}}{10^{50}\ {\rm erg}}\right)^{1/3} \times \left(\frac{n}{10^{-3}}\ {\rm cm}^{-3}\right)^{-1/3}\left(\frac{v_{\rm ej}}{0.3c}\right)^{-5/3}, \tag{29}$$

where E and v are the ejecta kinetic energy and initial velocity.[8] The peak flux can be estimated as

$$F_\nu \sim 10\ \mu{\rm Jy}\left(\frac{T_{\rm ej}}{10^{50}\ {\rm erg}}\right)\left(\frac{n}{10^{-3}\ {\rm cm}^{-3}}\right)^{\frac{p+2}{4}}\left(\frac{\epsilon_B}{10^{-2}}\right)^{\frac{p+2}{4}} \times \left(\frac{\epsilon_e}{10^{-1}}\right)^{p-1}\left(\frac{v_{\rm ej}}{0.3c}\right)^{\frac{5p-7}{2}}\left(\frac{D}{40\ {\rm Mpc}}\right)^{-2}\left(\frac{\nu}{3\ {\rm GHz}}\right)^{-\frac{p-1}{2}}, \tag{30}$$

where p is the spectral index of the nonthermal electrons.

As in the previous work by Hotokezaka et al. (2018b), who used the results of high-resolution merger simulations

[8] This deceleration time is measured in the merger rest frame. The difference between this time and observer time is about a factor of a few.

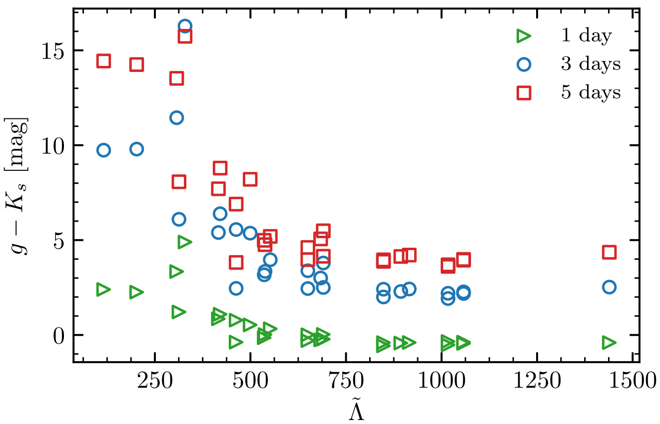

Figure 29. Color of the kilonova light curves for all the fiducial subset of simulations at three different times, as a function of the binary tidal parameter $\tilde{\Lambda}$. Light curves are computed for an observer located at a polar angle of 45°. The color of the transient at different times shows a significant correlation with $\tilde{\Lambda}$.

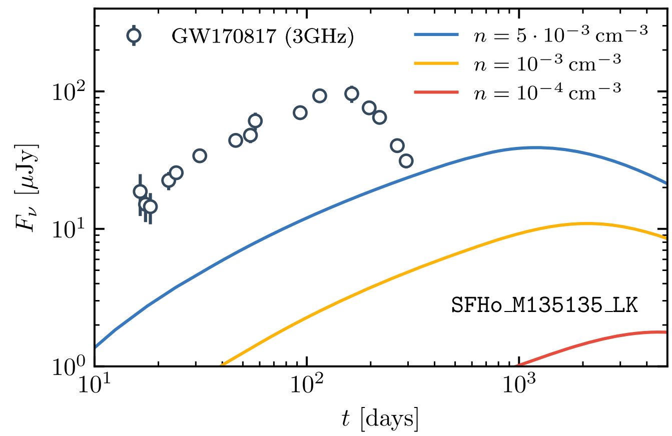

Figure 30. Radio light curves of the dynamical ejecta of SFHo_M135135_LK at 3 GHz. Here we assume the microphysics parameters to be $\epsilon_e = 0.1$, $\epsilon_B = 0.01$, and $p = 2.16$. Also shown as open circles are the observed flux densities at 3 GHz of the afterglow in GW170817 (Hallinan et al. 2017; Mooley et al. 2018a, 2018b).

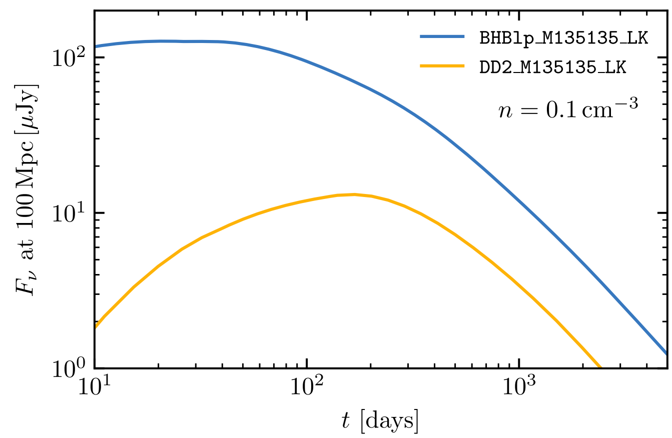

Figure 31. Radio light curves of DD2_M135135_LK and BHBlp_M135135_LK at 3 GHz. The distance to the source and ISM density are assumed to be 100 Mpc and 0.1 cm^{-3}, respectively. Here the microphysics parameters are set to be $\epsilon_e = \epsilon_B = 0.1$ and $p = 2.5$.

performed by Kiuchi et al. (2017), we also find the fast component of the dynamical ejecta with velocities of $\sim$0.3–0.8c to predominantly produce a synchrotron signal. Figure 30 shows the expected radio signals of the dynamical ejecta of SFHo_M135135_LK compared with GW170817. Here we calculate the light curve with a similar method to Hotokezaka et al. (2018b) and choose the number density of the ISM to be 10^{-4}–5×10^{-3} cm^{-3} as suggested by Mooley et al. (2018b). While the dynamical ejecta component is fainter than the observed flux densities until $\sim$ 300 days, this component can be detectable in radio and X-rays on timescales of a year to 10 years in the optimistic case. The peak flux density depends also on the EOS and it is fainter for the cases of DD2, BHB$\Lambda\phi$, and LS200 because the kinetic energy in the high-velocity component is lower than that of SFHo (see Equation (30) for the scaling).

The synchrotron remnant arising from the dynamical ejecta may be detectable in future GW events if the ISM density is large enough. For instance, radio counterparts with a flux of $\gtrsim$100 μJy can be detectable by blind survey with the VLA, ASKAP, and MeerKAT when the GW localization area is better than $\sim$30 deg^2 (Hotokezaka et al. 2016). Of course, if the host galaxy is identified by finding other EM counterparts, the detection limit is reduced to a few tens of μJy. Figure 31 shows the expected light curves for DD2_M135135_LK and BHBlp_M135135_LK at 3 GHz, assuming a distance of 100 Mpc and density of 0.1 cm^{-3}. Note that the radio flux of SFHo_M135135_LK is brighter than both models under the same condition (density, distance, and microphysics parameters). Therefore, the radio afterglow arising from the dynamical ejecta can be detectable for SFHo_M135135_LK and BHBlp_M135135_LK if a merger occurs within 100 Mpc and a surrounding ISM density of $\gtrsim$0.1 cm^{-3}.

It is worth noting that differences in the high-density part of the EOSs lead to large differences in the expected light curves. For example, as shown in Figure 31, BHBlp_M135135_LK results in a radio flux that is much brighter than that of DD2_M135135_LK, even though these EOSs share the same form up to around the nuclear saturation density. The reason is that BHBlp_M135135_LK produces a larger amount of fast-moving ejecta because of the more violent merger dynamics due to the appearance of Λ hyperons at high densities (see Figure 9). Therefore, we may be able to constrain the NS EOS using the observed light curves of the synchrotron remnants of future GW events.

The impact of viscosity on the synchrotron light curves is discussed in a companion paper (Radice et al. 2018b).

6. Conclusions

We have performed 59 full-GR NS merger simulations employing a microphysical treatment of the NS matter and including compositional and energy changes due to the emission of neutrinos. A subset of our simulations also included a treatment of neutrino re-absorption and/or of the effective viscosity due to MHD turbulence in the stars. This is the largest set of NS simulations with realistic microphysics to date. Our studies focused on the ejection of material during and after the mergers, and on the associated nucleosynthetic and EM signatures.

6.1. Mass Ejection

We find that material is ejected on a dynamical timescale during the mergers due to the combined effects of tidal torques, shocks, and neutrino heating. Tidally driven ejecta flow close to the orbital plane of the binary, have low entropies ($\sim 10\,k_B$ per baryon), and are very neutron rich, with electron fraction ~ 0.1. Shock-driven ejecta have broad distributions in entropy and electron fractions, and are distributed over a broad $\sim 60°$ angle from the orbital plane. Neutrino-driven winds are emitted preferentially close to the polar axis and have electron fractions in excess of 0.25. In accordance with previous studies using approximate GR and/or approximate microphysics (e.g., Bauswein et al. 2013; Hotokezaka et al. 2013b), we find that the most conspicuous episode of mass ejection is triggered by the centrifugal bounce of the merger remnant shortly after merger. Overall, we find dynamical ejecta masses of few times $10^{-3}\,M_\odot$ with average electron fractions $\lesssim 0.25$, and average entropies in the range 10–30 k_B per baryon.

The mass of the dynamical ejecta has a large numerical uncertainty. From a comparison of low- and high-resolution data, we estimate the relative error in its determination to be as large as 50%. Even larger discrepancies of a factor of a few are found when comparing with and among results published by different groups (Bauswein et al. 2013; Sekiguchi et al. 2015; Lehner et al. 2016; Bovard et al. 2017). On the other hand, the intensive properties of the ejecta, e.g., asymptotic velocity, composition, etc., appear to be robust with resolution.

We have studied the dependence of the outflow properties on the NS masses and EOSs. Following Dietrich & Ujevic (2017) we have constructed fits of the ejecta mass and velocity in terms of the NS masses and compactnesses. These capture some of the qualitative trend of our data reasonably well, especially for the ejecta velocity. However, the fitting coefficients we infer from our data are significantly different from those of Dietrich & Ujevic (2017). This is not too surprising given that most of the simulations used by Dietrich & Ujevic employed idealized microphysics and neglected weak reactions, which likely resulted in the overestimation of the ejecta mass (Radice et al. 2016b). We also find that there are systematic effects not captured by these fits. One of the main reasons is that the strength of the bounce of the merger remnant, an important parameter in determining the ejecta mass, depends on details of the EOS at higher densities and temperatures than those determining the fitting parameters. Accurate models of the dynamical ejecta mass could have important applications to multi-messenger astronomy and, indeed, the fits of Dietrich & Ujevic (2017) have already been applied, with small variations, to GW170817 (Abbott et al. 2017b; Coughlin et al. 2018). However, our results indicate that more work and better simulations will be required to build truly quantitative ejecta models.

Our results indicate that soft NS EOSs predict larger ejecta masses, at least in the range of mass ratios we have probed, in accordance with previous results (Bauswein et al. 2013; Hotokezaka et al. 2013b; Lehner et al. 2016; Sekiguchi et al. 2016; Bovard et al. 2017; Dietrich et al. 2017b). EOS effects are also imprinted in the ratio between the masses of the tidal and shock-heated components of the ejecta. However, we do not find any clear correlation between ejecta mass and velocity and the tidal deformability of the binary $\tilde{\Lambda}$. Consequently, it appears to be impossible to directly constrain the NS EOS from measurements of the dynamical ejecta. On the other hand, dynamical ejecta measurements might help to break degeneracies in the other binary parameters and, in this way, might improve the constraints on the tidal deformability of NSs indirectly.

We have analyzed the geometry of the outflows and found that it depends on the relative amount of tidal- and shock-driven ejecta, as does the average electron fraction. Consequently, we find that there is a correlation between the rms opening angle of the ejecta and the average electron fraction. This suggests that it might be possible to indirectly constrain the composition, and hence the nucleosynthetic yields, of the dynamical ejecta by combining observations of similar binary systems with different orientations.

We have computed the velocity distribution of the dynamical ejecta and found that shocks during and shortly after merger can accelerate a small fraction of the ejecta, $\sim 10^{-6}\,M_\odot$, to asymptotic velocities in excess of $0.6c$. This fast-moving material is preferentially located close to the orbital plane, presumably because of the oblate shape of the merger debris cloud into which the accelerating shocks propagate. It is also distributed in a very anisotropic fashion. The amount of material reaching these high velocities depends on the binary parameters and on the EOS. Binaries with compact NSs typically produce significantly more of this fast-moving component of the outflow. When comparing binaries simulated with the BHB$\Lambda\phi$ and DD2 EOSs, we find that the former systematically predicts a larger mass of the fast-moving ejecta by a factor of a few. This is because, even though BHB$\Lambda\phi$ and DD2 predict identical NS structures for most of the binaries we have considered, the former softens due to the appearance of Λ-hyperons after merger and predicts more violent bounces (Radice et al. 2017).

We find that binaries with remnants that are stable for at least several rotation periods after merger result in the formation of massive, ~ 0.1–$0.2\,M_\odot$, accretion disks. Conversely, BHs formed promptly after merger, i.e., within ~ 1 ms, are endowed with rather light accretion disks, $\sim 10^{-3}\,M_\odot$. More generally, the accretion disk masses are found to depend on the lifetime of the remnant and to correlate with the binary's tidal deformability (Radice et al. 2018c). It is expected that neutrino- and viscously driven outflows will carry away a significant fraction, $\sim$10%–50%, of these accretion disks on a timescale of a few seconds after the end of our calculations (Metzger & Fernández 2014; Just et al. 2015; Fernández et al. 2019; Fujibayashi et al. 2018; Siegel & Metzger 2018). Accordingly, these secular outflows are expected to be the dominant component of the ejecta. For this reason, kilonova observations can be used to constrain the accretion disk masses (Perego et al. 2017a) and binary tidal deformabilities (Radice et al. 2018c).

6.2. Nucleosynthesis

We have computed the nucleosynthetic yields of the dynamical ejecta. We find that second and third r-process peak isotopes, i.e., with $A \gtrsim 125$, are robustly produced with relative abundances close to solar. However, the relative abundance of light r-process elements, i.e., with $90 \lesssim A \lesssim 125$, and second and third peak isotopes are sensitive to the binary masses, weak reactions and, to a lesser extent, to the NS EOS.

We find that, for binaries close to the prompt BH formation threshold, different EOSs predict different ratios of tidal- and shock-driven dynamical ejecta and, consequently, different relative abundances of light r-process elements and second and third peak r-process elements. In particular, the LS220 and

DD2 EOSs predict that high-mass binaries should produce a smaller relative fraction of light elements compared to low-mass binaries, while the BHB$\Lambda\phi$ and SFHo EOSs have the opposite trend.

The absorption of neutrinos has a large impact on the composition and yields of the outflow. When neutrino absorption is included, the ejecta distribution in electron fraction becomes broad and Y_e of up to 0.4 are reached. The dynamical ejecta from comparable mass binaries in simulations that include neutrino re-absorption produce r-process isotopic abundances close to solar. If neutrino re-absorption is not included, light r-process elements are underproduced in our simulations. The isotopic abundances in the region of the first r-process peak are also sensitive to details of the neutrino treatment, such as the assumptions made for the incoming neutrino energy. This points to the need for simulations including energy-dependent neutrino-radiation treatments. This will be the object of future work.

The binary mass ratio also impacts the production of first-peak elements, with unequal mass systems underproducing elements with $90 \lesssim A \lesssim 125$. We find the relative yields to depend on the mass ratio almost as sensitively as on the neutrino treatment.

Secular ejecta is expected to be an important, if not dominant, component of the overall outflow, especially in the case of long-lived remnants or when massive disks are formed. Consequently, secular ejecta should be taken into account when estimating the nucleosynthetic yields from NS mergers. Presently, however, we can only speculate on the nucleosynthesis from this component. Long-term merger and postmerger simulations will be required to construct self-consistent models. We leave this to future work.

We have estimated the r-process nucleosynthesis yields using the simulation data extracted at a fixed radius of $300\,G/c^2\,M_\odot \simeq 450$ km and used pre-computed yields from parameterized trajectories. This is the same strategy we employed in Radice et al. (2016b). As part of our analysis, we have now validated this procedure by comparing with a more computationally expensive analysis using Lagrangian tracer particles. We find the nucleosynthesis to be rather insensitive to the detailed thermodynamical history of the tracer particles. The electron fraction of the material does not significantly evolve between the time we record it at $300\,G/c^2\,M_\odot$ and when the temperature drops below 6 GK and the r-process begins. On the other hand, we find that, due to advection errors in the position of the tracer particles, the Y_e distribution inferred from the tracers can differ quantitatively from that inferred from the grid data at the same radius. Overall, however, the differences between the results obtained with the two methods are well below those associated with other sources of uncertainty, most notably the treatment of neutrino radiation.

6.3. Electromagnetic Counterparts

We have computed synthetic kilonova light curves for all our models using the model of Perego et al. (2017a). Our light curve model is informed using the detailed angular structure of the outflows, density, velocity, and composition, as extracted from the simulations. These have been augmented with secular ejecta composed of neutrino-driven and viscously driven winds which we assume to entrain 3% and 20% of the disk, respectively. These values are motivated by recent long-term postmerger simulations (Metzger & Fernández 2014; Perego et al. 2014; Just et al. 2015; Martin et al. 2015; Fujibayashi et al. 2017, 2018; Fernández et al. 2019; Siegel & Metzger 2018).

Binaries resulting in prompt BH formation have kilonovae dominated by dynamical ejecta. These peak at about a day after merger and then rapidly decline. They are also very red, with $g - K_s \simeq 10$ mag three days after the merger. As the merger remnant lifetime increases, so does the disk mass, and hence the associated kilonovae become increasingly dominated by radiation coming from the secular ejecta. These kilonovae peak on longer timescales of few days to a week and are bluer, with $g - K_s \simeq 3$–7 mag three days after the merger. This suggests that kilonovae observations could be used to probe the lifetime of the merger remnant. A similar suggestion was also put forward by Metzger & Fernández (2014) and, more recently, by Lippuner et al. (2017). They argued that longer-lived remnants should result in bluer kilonovae because of the neutrino irradiation of the ejecta from the central remnant. This is expected to lower the electron fraction of the outflow below the threshold needed for the production of lanthanides, resulting in a drop of the photon opacity of the material. The phenomenon we find goes in the same direction, but is physically distinct since it arises from the correlation between disk masses and remnant lifetimes and not from changes in the ejecta photon opacity, which we have instead kept constant.

Since for most binaries the kilonova signal is dominated by the secular ejecta, the effect of the inclusion of neutrino re-absorption in the modeling of the dynamical ejecta has only a modest impact on the kilonova signal. Moreover, since remnant disk masses strongly correlate with binary tidal deformabilities, the peak properties of the kilonovae, i.e., peak time, magnitude, and width, are found to depend sensitively on $\tilde{\Lambda}$. This suggests that kilonovae observations could be used directly to probe the EOSs of NSs. However, it is important to stress than this correlation is in part due to our assumption that a fixed fraction of the accretion disk is ejected after merger. Long-term simulations of the evolution of postmerger remnants are necessary to verify if this assumption is valid, or whether light and massive postmerger disks evolve in quantitatively different ways.

We have computed the synchrotron radio signal expected from the interaction of the ejecta with the ISM using the model of Hotokezaka & Piran (2015). The radio fluence and the timescales over which the radio remnant evolves depend sensitively on the ISM density, and on the kinetic energy and the detailed velocity distribution of the ejecta.

We find that some of our models predict a rebrightening of the synchrotron signal from GW170817 on a timescale of months to years from the merger, when the emission from the ejecta will start to dominate over the emission coming from the SGRB jet.

Depending on the ISM density and the orientation of the binary, it may be possible to detect the radio signal due to the interaction of the ejecta with the ISM on timescales of weeks to months after merger at distances of up to ~100 Mpc. These observations would allow us to probe the velocity distribution of the ejecta and, hence, the violence with which the merged objects bounce back after the NS collision. This, in turn, depends on the EOS of matter at several times nuclear density. For instance, due to the appearance of Λ hyperons after the merger, the BHB$\Lambda\phi$ EOS predicts more violent mergers and

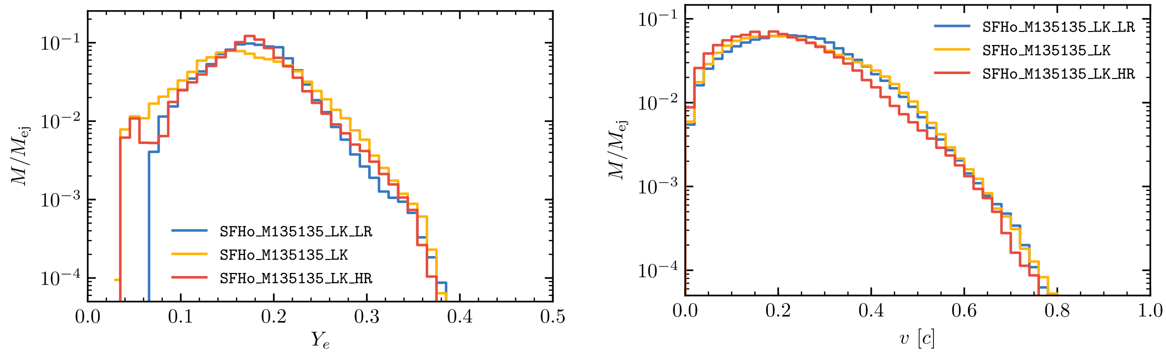

Figure 32. Dynamical ejecta sensitivity to resolution. Left panel: electron fraction; right panel: asymptotic velocity. The total ejecta mass shows large fractional variation with resolution; however, electron fraction, velocity distribution, and nucleosynthetic yields appear to be robust.

brighter radio flares by up to two orders of magnitude compared with the DD2 EOS, from which it only differs at high densities due to the inclusion of hyperons. This suggests that radio flares could be used to probe the EOS of NSs in a regime that is not accessible with GW observations of the inspiral alone.[9]

It is a pleasure to acknowledge A. Burrows for the many stimulating discussions. D.R. gratefully acknowledges support from a Frank and Peggy Taplin Membership at the Institute for Advanced Study and the Max-Planck/Princeton Center (MPPC) for Plasma Physics (NSF PHY-1523261). A.P. acknowledges support from the INFN initiative "High Performance data Network" funded by CIPE. D.R. and A.P. acknowledge support from the Institute for Nuclear Theory (17-2b program). A.P. thanks the Institute for Advanced Study for its hospitality and support. S.A.F. acknowledges support from the United States Department of Energy through the Computational Science Graduate Fellowship, grant No. DE-SC0019323. S.B. acknowledges support by the EU H2020 under ERC Starting grant, No. BinGraSp-714626. L.F.R. acknowledges support from US Department of Energy through the award number DE-SC0017955. The simulations were performed on BlueWaters, Bridges, Comet, and Stampede, and were enabled by the NSF PRAC program (ACI-1440083 and AWD-1811236) and the NSF XSEDE program (TG-PHY160025). The analysis employed computational resources provided by both the TIGRESS high performance computer center at Princeton University, which is jointly supported by the Princeton Institute for Computational Science and Engineering (PICSciE) and the Princeton University Office of Information Technology, and the Institute for Cyber-Enabled Research, which is supported by Michigan State University.

Software: `WhiskyTHC` (Radice et al. 2012), `Lorene` (Gourgoulhon et al. 1999), Matplotlib (Hunter 2007), NumPy (Oliphant 2015), SciPy (Jones et al. 2001), Pandas (McKinney 2010), iPython (Perez & Granger 2007), VisIt (Childs et al. 2012).

Appendix A
Finite-resolution Effects

Here we discuss uncertainties in the ejecta mass, velocity, and composition due to finite-resolution effects. The mass of the dynamical ejecta has not yet reached convergence at the resolution adopted in our simulations. As can be seen in Table 2, the dynamical ejecta mass shows moderate variations and changes in a non-monotonic way as we vary the grid resolution. Consequently, our estimate for the ejecta mass should only be considered as semi-quantitative. We estimate the relative uncertainty in the ejecta mass due to finite-resolution effects alone to be as large as 50%. We remark that, as discussed in Section 3.1, the differences between our and other published results, as well as between results published by different groups, are even larger (see also Table 3).

Despite the significant uncertainty in the total ejecta mass, we find the other properties of the outflow, i.e., velocity, composition, and entropy, to be robust with resolution. As an example, we show in Figure 32 histograms of the ejecta as a function of Y_e and of the asymptotic velocity for the `SFHo_M135135_LK` binary. The robustness of the ejecta properties suggests that, while the overall morphology of the outflow streams is well captured by the simulations, there are stochastic variations, for example resulting in the fallback of some of the material in these streams due to interaction with the merger debris, which affect the overall amount of matter entrained by these outflows (see also the discussion in Bauswein et al. 2013).

Appendix B
Treatment of the Viscous Fluxes

The GRLES approach requires the inclusion of the term $\partial_j(\sqrt{-g}\,\tau^{ij})$ in the fluid momentum equations. This numerical derivative needs to be carefully treated to avoid the odd–even decoupling instability. With this aim we introduce the left- and right-biased finite-differencing operators

$$\partial_i^{\pm} u = \pm \frac{u(x \pm h\boldsymbol{e}_i) - u(x)}{h}, \tag{31}$$

where ${e_i}^j = {\delta_i}^j$ are the coordinate basis vectors and h is the grid spacing. For the covariant derivatives we use the finite-differencing operators

$$D_i^{\pm} u^j = \partial_i^{\pm} u^j + \Gamma^j{}_{ik} u^k, \tag{32}$$

where $\Gamma^j{}_{ik}$ are the Christoffel symbols of the Levi–Cività connection associated with the spatial metric γ_{ij}. These are computed using a standard centered second-order finite-differencing operator.

[9] The high-density EOS could also be constrained with GW observations of the postmerger signal (Bernuzzi et al. 2015; Radice et al. 2017; Bauswein et al. 2018; Most et al. 2018a).

Using the biased finite-differencing operators we define

$$\tau^{\pm}_{ij} = -2\nu_{T}\,(\rho + p)W^2\left[\frac{1}{2}(D^{\pm}_i v_j + D^{\pm}_j v_i) - \frac{1}{3}D^{\pm}_k v^k \gamma_{ij}\right]. \tag{33}$$

Then we discretize the divergence of τ^{ij} as

$$\partial_j(\sqrt{-g}\,\tau^{ij}) \simeq \frac{1}{2}\{\partial^{-}_j[\sqrt{-g}\;(\tau^{+})^{ij}] + \partial^{+}_j[\sqrt{-g}\;(\tau^{-})^{ij}]\}. \tag{34}$$

It is easy to verify that this yields a flux-conservative scheme. Exact conservation is also ensured at refinement level boundaries using the flux correction algorithm of Berger & Colella (1989) as implemented in Reisswig et al. (2013a).

ORCID iDs

David Radice https://orcid.org/0000-0001-6982-1008
Albino Perego https://orcid.org/0000-0002-0936-8237
Kenta Hotokezaka https://orcid.org/0000-0002-2502-3730
Sebastiano Bernuzzi https://orcid.org/0000-0002-2334-0935

References

Abbott, B. P., Abbott, R., Abbott, T. D., et al. 2017a, Natur, 551, 7678
Abbott, B. P., Abbott, R., Abbott, T. D., et al. 2017b, ApJL, 850, L39
Abbott, B. P., Abbott, R., Abbott, T. D., et al. 2017c, ApJL, 848, L13
Abbott, B. P., Abbott, R., Abbott, T. D., et al. 2017d, PhRvL, 119, 161101
Abbott, B. P., Abbott, R., Abbott, T. D., et al. 2017e, ApJL, 848, L12
Abbott, B. P., Abbott, R., Abbott, T. D., et al. 2018a, PhRvL, 121, 161101
Abbott, B. P., Abbott, R., Abbott, T. D., et al. 2018b, arXiv:1805.11579
Abbott, B. P., Abbott, R., Abbott, T. D., et al. 2018c, LRR, 21, 3
Alexander, K. D., Margutti, R., Blanchard, P. K., et al. 2018, ApJL, 863, L18
Annala, E., Gorda, T., Kurkela, A., & Vuorinen, A. 2018, PhRvL, 120, 172703
Arcavi, I., McCully, C., Hosseinzadeh, G., et al. 2017, ApJL, 848, L33
Ardevol-Pulpillo, R., Janka, H. T., Just, O., & Bauswein, A. 2018, arXiv:1808.00006
Arlandini, C., Kaeppeler, F., Wisshak, K., et al. 1999, ApJ, 525, 886
Baiotti, L., Giacomazzo, B., & Rezzolla, L. 2008, PhRvD, 78, 084033
Baker, T., Bellini, E., Ferreira, P. G., et al. 2017, PhRvL, 119, 251301
Banik, S., Hempel, M., & Bandyopadhyay, D. 2014, ApJS, 214, 22
Barkov, M. V., Kathirgamaraju, A., Luo, Y., Lyutikov, M., & Giannios, D. 2018, arXiv:1805.08338
Barnes, J., & Kasen, D. 2013, ApJ, 775, 18
Baumgarte, T. W., Shapiro, S. L., & Shibata, M. 2000, ApJL, 528, L29
Bauswein, A., Bastian, N.-U. F., Blaschke, D. B., et al. 2018, arXiv:1809.01116
Bauswein, A., Goriely, S., & Janka, H. T. 2013, ApJ, 773, 78
Bauswein, A., Just, O., Janka, H.-T., & Stergioulas, N. 2017, ApJL, 850, L34
Beniamini, P., Petropoulou, M., Duran, R. B., & Giannios, D. 2019, MNRAS, 483, 840
Berger, M., & Colella, P. 1989, JCoPh, 82, 64
Berger, M. J., & Oliger, J. 1984, JCoPh, 53, 484
Bernuzzi, S., Dietrich, T., & Nagar, A. 2015, PhRvL, 115, 091101
Bernuzzi, S., & Hilditch, D. 2010, PhRvD, 81, 084003
Bernuzzi, S., Radice, D., Ott, C. D., et al. 2016, PhRvD, 94, 024023
Bovard, L., Martin, D., Guercilena, F., et al. 2017, PhRvD, 96, 124005
Bruenn, S. W. 1985, ApJS, 58, 771
Bucciantini, N., Metzger, B. D., Thompson, T. A., & Quataert, E. 2012, MNRAS, 419, 1537
Burrows, A., Reddy, S., & Thompson, T. A. 2006, NuPhA, 777, 356
Childs, H., Brugger, E., Whitlock, B., et al. 2012, in High Performance Visualization—Enabling Extreme-Scale Scientific Insight, ed. W. Bethel, H. Childs, & C. Hansen (Boca Raton, FL: CRC), 357
Chornock, R., Berger, E., Kasen, D., et al. 2017, ApJL, 848, L19
Ciolfi, R., Kastaun, W., Giacomazzo, B., et al. 2017, PhRvD, 95, 063016
Coughlin, M. W., Dietrich, T., Doctor, Z., et al. 2018, MNRAS, 480, 3871
Coulter, D. A., Foley, R. J., Kilpatrick, C. D., et al. 2017, Sci, 358, 1556
Cowperthwaite, P. S., Berger, E., Villar, V. A., et al. 2017, ApJL, 848, L17
De, S., Finstad, D., Lattimer, J. M., et al. 2018, PhRvL, 121, 091102
Deaton, M. B., O'Connor, E., Zhu, Y. L., et al. 2018, PhRvD, 98, 103014
Dessart, L., Ott, C., Burrows, A., Rosswog, S., & Livne, E. 2009, ApJ, 690, 1681
Dietrich, T., Bernuzzi, S., Ujevic, M., & Brügmann, B. 2015, PhRvD, 91, 124041
Dietrich, T., Bernuzzi, S., Ujevic, M., & Tichy, W. 2017a, PhRvD, 95, 044045
Dietrich, T., Radice, D., Bernuzzi, S., et al. 2018, arXiv:1806.01625
Dietrich, T., & Ujevic, M. 2017, CQGra, 34, 105014
Dietrich, T., Ujevic, M., Tichy, W., Bernuzzi, S., & Bruegmann, B. 2017b, PhRvD, 95, 024029
Dobie, D., Kaplan, D. L., Murphy, T., et al. 2018, ApJL, 858, L15
Drago, A., Pagliara, G., Popov, S. B., Traversi, S., & Wiktorowicz, G. 2018, Univ, 4, 50
Drout, M. R., Piro, A. L., Shappee, B. J., et al. 2017, Sci, 358, 1570
Duez, M. D., Liu, Y. T., Shapiro, S. L., & Shibata, M. 2006, PhRvD, 73, 104015
East, W. E., Paschalidis, V., Pretorius, F., & Shapiro, S. L. 2016, PhRvD, 93, 024011
Eichler, D., Livio, M., Piran, T., & Schramm, D. N. 1989, Natur, 340, 126
Eichler, M., Arcones, A., Kelic, A., et al. 2015, ApJ, 808, 30
Einfeldt, B. 1988, SIAM J. Numer. Anal., 25, 294
Evans, P. A., Cenko, S. B., Kennea, J. A., et al. 2017, Sci, 358, 1565
Fattoyev, F. J., Piekarewicz, J., & Horowitz, C. J. 2018, PhRvL, 120, 172702
Favata, M. 2014, PhRvL, 112, 101101
Fernández, R., & Metzger, B. D. 2013, MNRAS, 435, 502
Fernández, R., Tchekhovskoy, A., Quataert, E., Foucart, F., & Kasen, D. 2019, MNRAS, 482, 3373
Finstad, D., De, S., Brown, D. A., Berger, E., & Biwer, C. M. 2018, ApJL, 860, L2
Flanagan, E. E., & Hinderer, T. 2008, PhRvD, 77, 021502
Foucart, F. 2012, PhRvD, 86, 124007
Foucart, F., Duez, M. D., Kidder, L. E., et al. 2018a, PhRvD, 98, 063007
Foucart, F., Haas, R., Duez, M. D., et al. 2016a, PhRvD, 93, 044019
Foucart, F., Hinderer, T., & Nissanke, S. 2018b, PhRvD, 98, 081501
Foucart, F., O'Connor, E., Roberts, L., et al. 2015, PhRvD, 91, 124021
Foucart, F., O'Connor, E., Roberts, L., et al. 2016b, PhRvD, 94, 123016
Freiburghaus, C., Rosswog, S., & Thielemann, F.-K. 1999, ApJL, 525, L121
Frensel, M., Wu, M.-R., Volpe, C., & Perego, A. 2017, PhRvD, 95, 023011
Fujibayashi, S., Kiuchi, K., Nishimura, N., Sekiguchi, Y., & Shibata, M. 2018, ApJ, 860, 64
Fujibayashi, S., Sekiguchi, Y., Kiuchi, K., & Shibata, M. 2017, ApJ, 846, 114
Galeazzi, F., Kastaun, W., Rezzolla, L., & Font, J. A. 2013, PhRvD, 88, 064009
Ghirlanda, G., Salafia, O. S., Paragi, Z., et al. 2018, arXiv:1808.00469
Giacomazzo, B., & Perna, R. 2013, ApJL, 771, L26
Goriely, S., Bauswein, A., & Janka, H. T. 2011, ApJL, 738, L32
Gottlieb, S., Ketcheson, D. I., & Shu, C.-W. 2008, JSCom, 38, 251
Gourgoulhon, E., Grandclément, P., Marck, J.-A., Novak, J., & Taniguchi, K. 1999, LORENE, paris Observatory, Meudon section—LUTH laboratory, https://lorene.obspm.fr/
Guilet, J., Bauswein, A., Just, O., & Janka, H.-T. 2017, MNRAS, 471, 1879
Haggard, D., Nynka, M., Ruan, J. J., et al. 2017, ApJL, 848, L25
Hallinan, G., Corsi, A., Mooley, K. P., et al. 2017, Sci, 358, 1579
Hanauske, M., Takami, K., Bovard, L., et al. 2017, PhRvD, 96, 043004
Hempel, M., & Schaffner-Bielich, J. 2010, NuPhA, 837, 210
Hilditch, D., Bernuzzi, S., Thierfelder, M., et al. 2013, PhRvD, 88, 084057
Hinderer, T., Nissanke, S., Foucart, F., et al. 2018, arXiv:1808.03836
Hotokezaka, K., Beniamini, P., & Piran, T. 2018a, IJMPD, 27, 1842005
Hotokezaka, K., Kiuchi, K., Kyutoku, K., et al. 2013a, PhRvD, 88, 044026
Hotokezaka, K., Kiuchi, K., Kyutoku, K., et al. 2013b, PhRvD, 87, 024001
Hotokezaka, K., Kiuchi, K., Shibata, M., Nakar, E., & Piran, T. 2018b, ApJ, 867, 95
Hotokezaka, K., Kyutoku, K., Okawa, H., Shibata, M., & Kiuchi, K. 2011, PhRvD, 83, 124008
Hotokezaka, K., Nakar, E., Gottlieb, O., et al. 2018c, arXiv:1806.10596
Hotokezaka, K., Nissanke, S., Hallinan, G., et al. 2016, ApJ, 831, 190
Hotokezaka, K., & Piran, T. 2015, MNRAS, 450, 1430
Hunter, J. D. 2007, CSE, 9, 90
Ishii, A., Shigeyama, T., & Tanaka, M. 2018, ApJ, 861, 25
Jones, E., Oliphant, T., & Peterson, P. 2001, SciPy: Open source scientific tools for Python, http://www.scipy.org/
Just, O., Bauswein, A., Pulpillo, R. A., Goriely, S., & Janka, H. T. 2015, MNRAS, 448, 541
Kasen, D., Badnell, N. R., & Barnes, J. 2013, ApJ, 774, 25
Kasen, D., Metzger, B., Barnes, J., Quataert, E., & Ramirez-Ruiz, E. 2017, Natur, 551, 80

Kasliwal, M. M., et al. 2017, Sci, 358, 1559
Kastaun, W., Ciolfi, R., & Giacomazzo, B. 2016, PhRvD, 94, 044060
Kastaun, W., & Galeazzi, F. 2015, PhRvD, 91, 064027
Kawaguchi, K., Kyutoku, K., Shibata, M., & Tanaka, M. 2016, ApJ, 825, 52
Kawaguchi, K., Shibata, M., & Tanaka, M. 2018, ApJl, 865, L21
Kim, S., Schulze, S., Resmi, L., et al. 2017, ApJL, 850, L21
Kiuchi, K., Kawaguchi, K., Kyutoku, K., et al. 2017, PhRvD, 96, 084060
Kiuchi, K., Kyutoku, K., Sekiguchi, Y., & Shibata, M. 2018, PhRvD, 97, 124039
Kiuchi, K., Kyutoku, K., Sekiguchi, Y., Shibata, M., & Wada, T. 2014, PhRvD, 90, 041502
Kiuchi, K., Sekiguchi, Y., Shibata, M., & Taniguchi, K. 2010, PhRvL, 104, 141101
Korobkin, O., Rosswog, S., Arcones, A., & Winteler, C. 2012, MNRAS, 426, 1940
Kreiss, H. O., & Oliger, J. 1973, Methods for the Approximate Solution of Time Dependent Problems (Geneva: GARP)
Kulkarni, S. R. 2005, arXiv:astro-ph/0510256
Kurganov, A., & Tadmor, E. 2000, JCoPh, 160, 241
Kyutoku, K., Ioka, K., & Shibata, M. 2014, MNRAS, 437, L6
Lattimer, J. M. 2012, ARNPS, 62, 485
Lattimer, J. M., & Schramm, D. N. 1974, ApJL, 192, L145
Lattimer, J. M., & Swesty, F. D. 1991, NuPhA, 535, 331
Lazzati, D., Perna, R., Morsony, B. J., et al. 2018, PhRvL, 120, 241103
Lee, W. H., Ramirez-Ruiz, E., & López-Cámara, D. 2009, ApJL, 699, L93
Lehner, L., Liebling, S. L., Palenzuela, C., et al. 2016, CQGra, 33, 184002
Li, L.-X., & Paczynski, B. 1998, ApJL, 507, L59
Lippuner, J., Fernández, R., Roberts, L. F., et al. 2017, MNRAS, 472, 904
Lippuner, J., & Roberts, L. F. 2015, ApJ, 815, 82
Löffler, F., Faber, J., Bentivegna, E., et al. 2012, CQGra, 29, 115001
Lombriser, L., & Taylor, A. 2016, JCAP, 1603, 031
Lowrie, R., & Morel, J. 2001, JQSRT, 69, 475
Lyman, J. D., et al. 2018, NatAs, 2, 751
Malik, T., Alam, N., Fortin, M., et al. 2018, PhRvC, 98, 035804
Margalit, B., & Metzger, B. D. 2017, ApJL, 850, L19
Margutti, R., Alexander, K. D., Xie, X., et al. 2018, ApJL, 856, L18
Margutti, R., Berger, E., Fong, W., et al. 2017, ApJL, 848, L20
Martin, D., Perego, A., Arcones, A., et al. 2015, ApJ, 813, 2
McKinney, W. 2010, in Proc. 9th Python in Science Conf., ed. S. van der Walt & J. Millman (Austin, TX: SciPy), 51
McManus, R., Lombriser, L., & Peñarrubia, J. 2016, JCAP, 1611, 006
Metzger, B. D., Arcones, A., Quataert, E., & Martínez-Pinedo, G. 2010, MNRAS, 402, 2771
Metzger, B. D., Bauswein, A., Goriely, S., & Kasen, D. 2015, MNRAS, 446, 1115
Metzger, B. D., & Fernández, R. 2014, MNRAS, 441, 3444
Metzger, B. D., Martínez-Pinedo, G., Darbha, S., et al. 2010, MNRAS, 406, 2650
Metzger, B. D., Piro, A. L., & Quataert, E. 2008, MNRAS, 390, 781
Metzger, B. D., Piro, A. L., & Quataert, E. 2009, MNRAS, 396, 304
Metzger, B. D., Thompson, T. A., & Quataert, E. 2018, ApJ, 856, 101
Meyer, B. S. 1989, ApJ, 343, 254
Mooley, K. P., Deller, A. T., Gottlieb, O., et al. 2018b, Natur, 561, 355
Mooley, K. P., Nakar, E., Hotokezaka, K., et al. 2018a, Natur, 554, 207
Most, E. R., Weih, L. R., Rezzolla, L., & Schaffner-Bielich, J. 2018b, PhRvL, 120, 261103
Most, E. R., Papenfort, L. J., Dexheimer, V., et al. 2018a, arXiv:1807.03684
Nakar, E., & Piran, T. 2011, Natur, 478, 82
Nakar, E., & Piran, T. 2018, MNRAS, 478, 407
Nandi, R., Char, P., & Pal, S. 2018, arXiv:1809.07108
Neilsen, D., Liebling, S. L., Anderson, M., et al. 2014, PhRvD, 89, 104029
Nicholl, M., Berger, E., Kasen, D., et al. 2017, ApJL, 848, L18
O'Connor, E., & Ott, C. D. 2010, CQGra, 27, 114103
Oechslin, R., Janka, H. T., & Marek, A. 2007, A&A, 467, 395
Oliphant, T. E. 2015, A Guide to NumPy, Vol. 2 (Spanish Fork, UT: Trelgol)
Ozel, F., & Freire, P. 2016, ARA&A, 54, 401
Palenzuela, C., Lehner, L., Ponce, M., et al. 2013, PhRvL, 111, 061105
Palenzuela, C., Liebling, S. L., Neilsen, D., et al. 2015, PhRvD, 92, 044045
Pardo, K., Fishbach, M., Holz, D. E., & Spergel, D. N. 2018, JCAP, 1807, 048
Paschalidis, V., East, W. E., Pretorius, F., & Shapiro, S. L. 2015, PhRvD, 92, 121502
Paschalidis, V., Yagi, K., Alvarez-Castillo, D., Blaschke, D. B., & Sedrakian, A. 2018, PhRvD, 97, 084038
Perego, A., Cabezón, R., & Käppeli, R. 2016, ApJS, 223, 22
Perego, A., Radice, D., & Bernuzzi, S. 2017a, ApJL, 850, L37
Perego, A., Rosswog, S., Cabezón, R. M., et al. 2014, MNRAS, 443, 3134
Perego, A., Yasin, H., & Arcones, A. 2017b, JPhG, 44, 084007
Perez, F., & Granger, B. E. 2007, CSE, 9, 21
Piran, T., Nakar, E., & Rosswog, S. 2013, MNRAS, 430, 2121
Plewa, T., & Müller, E. 1999, A&A, 342, 179
Pollney, D., Reisswig, C., Schnetter, E., Dorband, N., & Diener, P. 2011, PhRvD, 83, 044045
Qian, Y. Z., & Woosley, S. E. 1996, ApJ, 471, 331
Radice, D. 2017, ApJL, 838, L2
Radice, D., Bernuzzi, S., Del Pozzo, W., Roberts, L. F., & Ott, C. D. 2017, ApJL, 842, L10
Radice, D., Bernuzzi, S., & Ott, C. D. 2016a, PhRvD, 94, 064011
Radice, D., Galeazzi, F., & Kastaun, W. 2012, WhiskyTHC: A General Relativistic Hydrodynamics Code, https://www.astro.princeton.edu/∼dradice/whiskythc.html
Radice, D., Galeazzi, F., Lippuner, J., et al. 2016b, MNRAS, 460, 3255
Radice, D., Perego, A., Bernuzzi, S., & Zhang, B. 2018a, MNRAS, 481, 3670
Radice, D., Perego, A., Hotokezaka, K., et al. 2018b, arXiv:1809.11163
Radice, D., Perego, A., Zappa, F., & Bernuzzi, S. 2018c, ApJL, 852, L29
Radice, D., & Rezzolla, L. 2012, A&A, 547, A26
Radice, D., Rezzolla, L., & Galeazzi, F. 2014a, MNRAS, 437, L46
Radice, D., Rezzolla, L., & Galeazzi, F. 2014b, CQGra, 31, 075012
Radice, D., Rezzolla, L., & Galeazzi, F. 2015, in ASP Conf. Ser. 498, Numerical Modeling of Space Plasma Flows ASTRONUM-2014, ed. N. V. Pogorelov et al. (San Francisco, CA: ASP), 121
Reisswig, C., Haas, R., Ott, C. D., et al. 2013a, PhRvD, 87, 064023
Reisswig, C., Ott, C. D., Abdikamalov, E., et al. 2013b, PhRvL, 111, 151101
Resmi, L., Schulze, S., Ishwara-Chandra, C. H., et al. 2018, ApJ, 867, 57
Rezzolla, L., Baiotti, L., Giacomazzo, B., Link, D., & Font, J. A. 2010, CQGra, 27, 114105
Rezzolla, L., Giacomazzo, B., Baiotti, L., et al. 2011, ApJL, 732, L6
Rezzolla, L., Most, E. R., & Weih, L. R. 2018, ApJL, 852, L25
Rosswog, S., & Davies, M. B. 2003, MNRAS, 345, 1077
Rosswog, S., Feindt, U., Korobkin, O., et al. 2017, CQGra, 34, 104001
Rosswog, S., & Liebendoerfer, M. 2003, MNRAS, 342, 673
Rosswog, S., Liebendoerfer, M., Thielemann, F. K., et al. 1999, A&A, 341, 499
Rosswog, S., Piran, T., & Nakar, E. 2013, MNRAS, 430, 2585
Rosswog, S., Ramirez-Ruiz, E., & Davies, M. B. 2003, MNRAS, 345, 1077
Rosswog, S., Sollerman, J., Feindt, U., et al. 2018, A&A, 615, A132
Ruan, J. J., Nynka, M., Haggard, D., Kalogera, V., & Evans, P. 2018, ApJL, 853, L4
Ruffert, M. H., Janka, H. T., & Schaefer, G. 1996, A&A, 311, 532
Ruiz, M., Lang, R. N., Paschalidis, V., & Shapiro, S. L. 2016, ApJL, 824, L6
Ruiz, M., Shapiro, S. L., & Tsokaros, A. 2018, PhRvD, 97, 021501
Schnetter, E., Hawley, S. H., & Hawke, I. 2004, CQGra, 21, 1465
Sekiguchi, Y. 2010, PThPh, 124, 331
Sekiguchi, Y., Kiuchi, K., Kyutoku, K., & Shibata, M. 2011, PhRvL, 107, 051102
Sekiguchi, Y., Kiuchi, K., Kyutoku, K., & Shibata, M. 2015, PhRvD, 91, 064059
Sekiguchi, Y., Kiuchi, K., Kyutoku, K., Shibata, M., & Taniguchi, K. 2016, PhRvD, 93, 124046
Shakura, N. I., & Sunyaev, R. A. 1973, A&A, 24, 337
Shapiro, S. L., & Teukolsky, S. A. 1983, Black Holes, White Dwarfs, and Neutron Stars: The Physics of Compact Objects (New York: Wiley)
Shibata, M. 2016, Numerical Relativity (Singapore: World Scientific)
Shibata, M., Fujibayashi, S., Hotokezaka, K., et al. 2017a, PhRvD, 96, 123012
Shibata, M., Kiuchi, K., & Sekiguchi, Y.-i. 2017b, PhRvD, 95, 083005
Shibata, M., & Taniguchi, K. 2006, PhRvD, 73, 064027
Shibata, M., Taniguchi, K., & Uryu, K. 2003, PhRvD, 68, 084020
Shibata, M., Taniguchi, K., & Uryu, K. 2005, PhRvD, 71, 084021
Shibata, M., & Uryu, K. 2000, PhRvD, 61, 064001
Siegel, D. M., Ciolfi, R., & Rezzolla, L. 2014, ApJL, 785, L6
Siegel, D. M., & Metzger, B. D. 2017, PhRvL, 119, 231102
Siegel, D. M., & Metzger, B. D. 2018, ApJ, 858, 52
Smartt, S. J., Chen, T.-W., Jerkstrand, A., et al. 2017, Natur, 551, 75
Soares-Santos, M., et al. 2017, ApJL, 848, L16
Steiner, A. W., Hempel, M., & Fischer, T. 2013, ApJ, 774, 17
Suresh, A. 1997, JCoPh, 136, 83
Symbalisty, E., & Schramm, D. N. 1982, ApJL, 22, 143
Tanaka, M., & Hotokezaka, K. 2013, ApJ, 775, 113
Tanaka, M., Utsumi, Y., Mazzali, P. A., et al. 2017, PASJ, 69, 102
Tanvir, N. R., Levan, A. J., González-Fernández, C., et al. 2017, ApJL, 848, L27
Tews, I., Margueron, J., & Reddy, S. 2018, PhRvC, 98, 045804

Thielemann, F. K., Eichler, M., Panov, I. V., & Wehmeyer, B. 2017, ARNPS, 67, 253
Troja, E., Piro, L., van Eerten, H., et al. 2017, Natur, 551, 7678
Tsang, C. Y., Tsang, M. B., Danielewicz, P., Lynch, W. G., & Fattoyev, F. J. 2018, arXiv:1807.06571
Typel, S., Ropke, G., Klahn, T., Blaschke, D., & Wolter, H. H. 2010, PhRvC, 81, 015803
Utsumi, Y., Tanaka, M., Tominaga, N., et al. 2017, PASJ, 69, 101
van Eerten, H. J., & MacFadyen, A. I. 2011, ApJL, 733, L37
van Riper, K. A., & Lattimer, J. M. 1981, ApJ, 249, 270
Villar, V. A., Guillochon, J., Berger, E., et al. 2017, ApJL, 851, L21
Visinelli, L., Bolis, N., & Vagnozzi, S. 2018, PhRvD, 97, 064039
Wanajo, S., Sekiguchi, Y., Nishimura, N., et al. 2014, ApJL, 789, L39
Waxman, E., Ofek, E., Kushnir, D., & Gal-Yam, A. 2018, MNRAS, 481, 3423
Wei, J. B., Figura, A., Burgio, G. F., Chen, H., & Schulze, H. J. 2018, arXiv:1809.04315
Wu, M.-R., Fernández, R., Martínez-Pinedo, G., & Metzger, B. D. 2016, MNRAS, 463, 2323
Wu, M.-R., Tamborra, I., Just, O., & Janka, H.-T. 2017, PhRvD, 96, 123015
Zhu, Y.-L., Perego, A., & McLaughlin, G. C. 2016, PhRvD, 94, 105006